POLITECNICO DI TORINO

MSc in Mechatronic Engineering

Master's Thesis

Robust Control Techniques for High-Power Electric Geostationary Satellites with Rotating Solar Arrays

Politecnico di Torino

Advisor:
Prof. Fabrizio Dabbene

Candidate:
Marco Giorgiutti

Co-advisor:
Dr. Martina Mammarella, PhD

Academic Year 2020/2021

Abstract

Optimal robust sun-pointing control for the Eutelsat 172B, a large geostationary electrical propelled satellite, is addressed in this thesis. For spacecraft which propulsion module is based exclusively on high-power electric engines, it is crucial to guarantee the optimal power production during the whole mission. Moreover, for telecommunication satellites is fundamental to maintain the desired pointing to fulfill mission and operational requirements, despite external perturbations that could affect their orientation. To optimize the power generation, guaranteeing proper solar-array sun-tracking, while tracking the desired Earth-pointing orientation of the satellite and its payloads, a first-order Sliding Mode Controller and a Tube-based Robust Model Predictive Control strategy have been implemented, combined with a controller for arrays sun tracking. The first part of this thesis work is devoted to the development of the Eutelsat 172B simulator, focusing on the environmental disturbances, the multibody dynamics model of the satellite and the electrical power production system. The second part is devoted to the design of the attitude and solar arrays drive controllers. Both attitude controllers proved to be able to reject the environmental disturbance torques and the modelling uncertainties due to the inertia modification caused by solar panels re-orientation. Moreover, we demonstrate how the proper control of solar array orientation can improve the solar power production. This aspect could allow, during the design phase, to reduce the solar array area and the satellite weight mass, thus further reducing launch and mission costs.

Contents

List of Figures

Acronyms

AEPR Average Electrical Power Requirement.

AOCS Attitude and Orbital Control Systems.

AU Astronomical Unit.

BoL Begin of Life.

CoM Center of Mass.

DCM Direct Cosine Matrix.

DoF Degrees of Freedom.

ECEF Earth Centered Earth Fixed.

ECI Earth Centered Intertial.

EoL End of Life.

EOR Electric Orbit Raising.

EPS Electrical Power Subsystem.

ESA European Space Agency.

GEO Geostationary Earth Orbit.

GMST Greenwich Mean Sideral Time.

HET Hall Effect Thruster.

IGRF Internationl Geomagnetic Reference Field.

JD Julian Date.

JPL Jet Propulsion Laboratory.

LEO Low Earth Orbit.

LHS Left Hand Side.

LP Linear Programming.

LQR Linear Quadratic Regulator.

LVLH Local Vertical Local Horizontal.

MIMO Multiple Input Multiple Output.

MPC Model Predictive Control.

MPI Maximal Positive Invariant set.

NASA National Aeronautics and Space Administration.

PCPPDR Power Charge Regulator and Power Dis-charge Regulator.

PDU Power Distribution Unit.

PEPR Peak Electrical Power Requirement.

PI Positive Invariant set.

PMSM Permanent Magnet Synchronous Motor.

PPM Power Production Mode.

PQW Perifocal Reference Frame.

QP Quadratic Programming.

RDM Residual Magnetic Dipole Moment.

RMPC Robust Model Predictive Control.

RPI Robust Positive Invariant.

SA Solar Arrays.

SADA Solar Array Drive Actuator.

SMC Sliding Mode Controller.

SRP Solar Radiation Pressure.

SS State Space.

TPM Thruster Pointing Mechanism.

TRMPC Tube Robust Model Predictive Control.

UTC Coordinated Universal Time.

UTJ Ultra Triple Junction.

Nomenclature

γ	Solar array rotation angle
ν	True anomaly
c_δ	cod of angle δ
s_δ	sin of angle δ
S_{ij}	element at row i and column j of matrix $\mathbf{S}$

Physical constants table

Quantity	Symbol	Value	Dimension
Solar Irradiance	$\mathcal{F}_\odot$	1361	$\mathrm{W\,m^{-2}}$
Speed of light	c	299792458	$\mathrm{m\,s^{-1}}$
Mean equatorial radius of Earth	$R_\oplus$	6378	km
Earth angular velocity	$\|\boldsymbol{\omega}_E\|$	7.2516×10^{-5}	$\mathrm{rad\,s^{-1}}$
Gravity acceleration	g_0	9.8067	$\mathrm{m\,s^{-2}}$

Chapter 1

Introduction

Geosynchronous GEO satellites are a class of satellites characterized by an orbit time equal to the Earth rotation time, allowing to maintain a constant position with respect to the Earth. These satellites are employed for several applications, most notably for communication, weather forecasting, navigation and military purposes [6]. The idea of the geosynchronous satellite dates to the early '30, but due to the unavailable technology of those years the idea did become feasible only during the '60, when Harold Rosen designed the first geosynchronous satellite, the Syncom. The Syncom satellite, launched by National Aeronautics and Space Administration (NASA), become operational in 1963 [7]. The geostationary orbit is located at an altitude of approximately 35.786 km from the equator of the Earth and it has a radius of 42.164 km. Although the orbit length is quite big, it does not allow for an unlimited number of satellites. The reason for this limitation is that, while occupying a slot in space, a satellite requires a specific radio frequency in the electromagnetic spectrum. These radio frequencies must be different and the satellites must be approximately eighteen kilometers apart so that there is no interference between the different transmissions. Theoretically, the total number of satellites capable of remaining in geostationary orbit is approximately two thousand [8]. Hence, the advancement in GEO satellite design are focused in increasing the platform size to accommodate larger payloads in each satellite. This of course introduces higher launch cost due to the satellite size and requires innovation in all satellite systems. The trend in GEO satellites design has consolidated into: a considerable increment of on board electrical power generation, an increase in platform size, bigger solar arrays and longer satellite operational time.

According to the NASA Technology Roadmap [9] the field of satellite propulsion and electrical power production systems are the enabler for new advancements in the GEO satellite design. Satellite propulsion systems are responsible for all the functions of primary propulsion, reaction control, station keeping, precision pointing and orbital maneuvering. The reaction control and orbital maneuvering systems provide the propulsive force for orbit maintenance, position control, station keeping, and spacecraft attitude control. One of the most promising advancement is represented by Hall Effect Thruster (HET) which is a high specific impulse - low thrust electrical thruster. The HET accelerate reaction mass (e.g., Xenon propellant) electromagnetically to generate thrust. The use of electrical power thrusters enhances the propulsive system performances compared with conventional chemical thrusters system. Unlike chemical sys-

tems, electric propulsion requires very little mass to accelerate a spacecraft. The propellant is ejected up to twenty times faster than a classical chemical thruster. Therefore the overall system turns out to be more mass efficient, thus enabling the extension of the mission lifetime duration [10].

Of course, all these benefits come at a price; the increase in electrical power demand. The EPS is responsible for the production of power and its distribution to the loads. The power generation in GEO satellite is a task demanded to the Solar Arrays (SA). The SA technology advancements lead to solar cell with 29 percent maximum conversion efficiency, anyway the design of high power systems generally results in increasing the SA size. One viable solution is to make the orientation of the SA independent from the payload orientation. This feature can be added by installing mechanism that allow the rotation of the SA. The addition of this feature for Earth-pointing GEO satellites increase the power production and its continuity since the produced power is almost constant along the orbit.

Another peculiar characteristic of GEO satellite are the pointing capabilities. For example Eutelsat 172B, which is the satellite analyzed in this thesis, can guarantee a pointing accuracy of ± 0.05 degrees [11]. Hence, the propulsion system has to guarantee proper pointing performances. Historically the type of actuators employed in GEO satellites were chemical thrusters. While the HET are currently used for station keeping purposes [12], the implementation of electric thrusters for attitude control is becoming feasible thanks to the advancements in the μN level thrusters [12]. A viable solution is then represented by coldgas, resistojet and mini-HET thrusters which, by exploiting the same Xenon bus of the orbit maneuvering system, allows to reduce complexity and cost of commercial platforms [13]

To satisfy the pointing requirements an attitude controller shall be implemented. Attitude control is a subsystem of the Attitude and Orbital Control Systems (AOCS). The attitude control objective is to drive the system towards the attitude trajectory minimizing the pointing error. Attitude control is not a new research topic, it has been deeply investigated during the years. Due to the recent introduction of electric thrusters in the satellite design some attitude control techniques using electric thrusters for GEO satellites have been proposed. Some of them are: [14] where a Model Predictive Control (MPC) scheme considering the on/off actuator and the number of firings has been applied; [15] where a MPC scheme that considers a complete AOCS employing reaction wheel and HET accounting for wheel saturation.

The aforementioned methods did not consider both the pointing constraints and the disturbance rejection together. In fact in GEO scenario several persistent, but bounded, disturbances act on the satellite and when external noise is included in the system dynamics, classical MPC schemes cannot ensure the robustness required to deal with the disturbances and to satisfy the mission and system constraints, whereas it can provide only a certain level of inherent robustness as a feedback control scheme [16]. Recently, a TRMPC approach has been developed and successfully applied to control attitude and trajectory of spacecraft during rendezvous and proximity operation. The TRMPC control strategy compared to the other Robust Model Predictive Control (RMPC) schemes benefits of a low computational load at the cost of constraint tightening [17]. In this thesis a TRMPC attitude control strategy is proposed for a geostationary satellite, the Eultelsat 172B, equipped with a full-electric propulsion system.

Large GEO satellite usually allow the rotation of the solar arrays around one or two axes [18, 19], thus a Solar Array Drive Actuator (SADA) system is mounted to perform the rotation of the solar arrays for sun tracking purposes. The main problem related with SADA control found in the literature is the suppression of the solar arrays induced vibrations as described in [20, 21]. In this thesis the panels are assumed to be rigid and the actuator dynamics is considered fast enough to produce the desired torque output directly, thus the vibration related problems are neglected. The proposed SADA controller is a saturated LQR controller.
The coupling of the attitude control and the SADA had required the development of a new model for the attitude dynamics of the satellite. In fact, models based on the single rigid body equations, e.g. Euler equations, do not include this feature. Thus, to solve this problem a multibody model of the satellite has been derived in this thesis.

The goal of this thesis is to provide a system level design, simulation and analysis of a GEO satellite focusing on the attitude propulsion subsystem and the electrical power subsystem. Another aims of this thesis is to preliminary assess the advantages and the drawbacks of a configuration implementing rotating SA in the Eutelsat 172B mission.

The design phase focuses on the development of an attitude dynamics model and its controllers. The controlled implemented in this thesis are TRMPC and a Sliding Mode Controller (SMC). The first one is a the controller proposed in this thesis, whereas the second one in standard attitude control technique that will be used as a benchmark for the TRMPC. The simulation phase is devoted to the simulation of the satellite systems focusing on the propulsion subsystem and electrical power subsystem in different scenarios. Finally, a comparison analysis of the simulation results of the different scenarios is presented. Due to the complexity of the topic, some simplifying assumptions throughout the modeling phase have been made. For instance, the strongest assumptions made are: the decoupling between the orbital control system and the attitude control system, the HET attitude actuator system is modeled as a adjustable thrust chemical thruster and the solar arrays mechanical model is considered rigid.

The thesis is organized as follows: Chapter 2 describes the satellite mission and the main satellite subsystem involved; Chapter 3 describes the the reference frames in space and the space environment; Chapter 4 describes the model used for the satellite simulator; Chapter 5 presents the controllers employed in this thesis; Chapter 6 shown the obtained results and their comparison; finally in Chapter 7 the conclusions and the further improvements are presented.

Chapter 2

EUTELSAT 172B

2.1 Satellite description

Figure 2.1: Rendering of Eutelsat 172B in orbit [Credit AIRBUS]

Eultelsat 172B is a GEO telecommunications with a high throughput payload and all electric orbital raising. This satellite was built by Airbus Defence and Space and is based on the Eurostar E3000 platform. The Eurostar E3000 satellite platform allow the rotation of the solar arrays enhancing the electrical power production [22]. This version uses only electric propulsion, based on a Fakel SPT140D propulsion unit, for initial orbit raising and all on-orbit manoeuvres. The initial orbit raising maneuvers , which brought the satellite to reach its final GEO orbit from the release one, lasted four months [23].
As the name of the satellite suggests, it stations at the 172^o meridian, in the east transpacific neighborhood. The coverage area of the satellite is depicted in figure 2.2 [1].

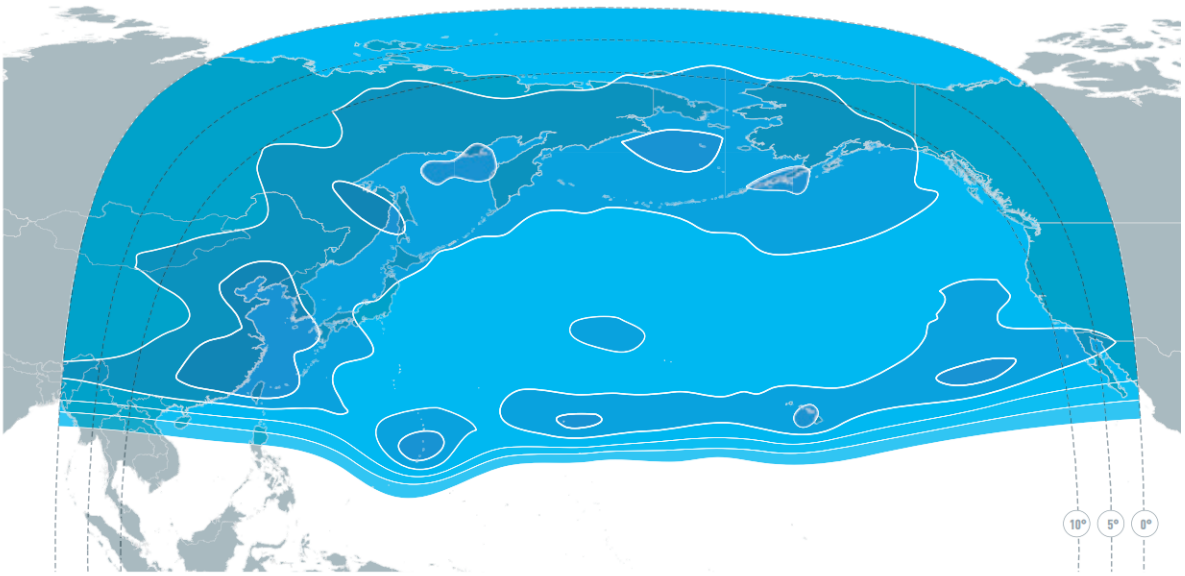

Figure 2.2: Eutelsat coverage [Credit Eutelsat [1]]

The GEO orbit has circular shape and it is contained in the plane generated by the equator. The nominal radius of the orbit is 42164 km which corresponds to an average distance above the Earth of 35786 km . The orbital trajectory of the Eutelsat 172 is shown in figure 2.3.
The Eutelsat 172B, rendered in figure 2.1, is composed by a main body and two fixed solar array, respectively the blue body the two purple parallelepipeds shown in 2.4. The payload is attached to the main body and the telecommunication devices are pointed towards the negative direction of x-axis. Hence, since the Eutelsat is a telecommunication satellite the negative direction of the x-axis shall be aligned to the nadir pointing vector.
The physical properties of the main body are described in table 2.1, while the physical properties of each solar array are described in table 2.2 [11].

dimension	measure	unit
l_x^{SC}	5.7	m
l_y^{SC}	3.0	m
l_z^{SC}	3.7	m
m_d	3400	kg
m_f	0-151	kg
m_w	3400-3551	kg

Table 2.1: Main body physical properties

The Center of Mass (CoM) of the main body coincides with the origin of the body reference frame and it is fixed, i.e. it does not vary during the mission horizon. The

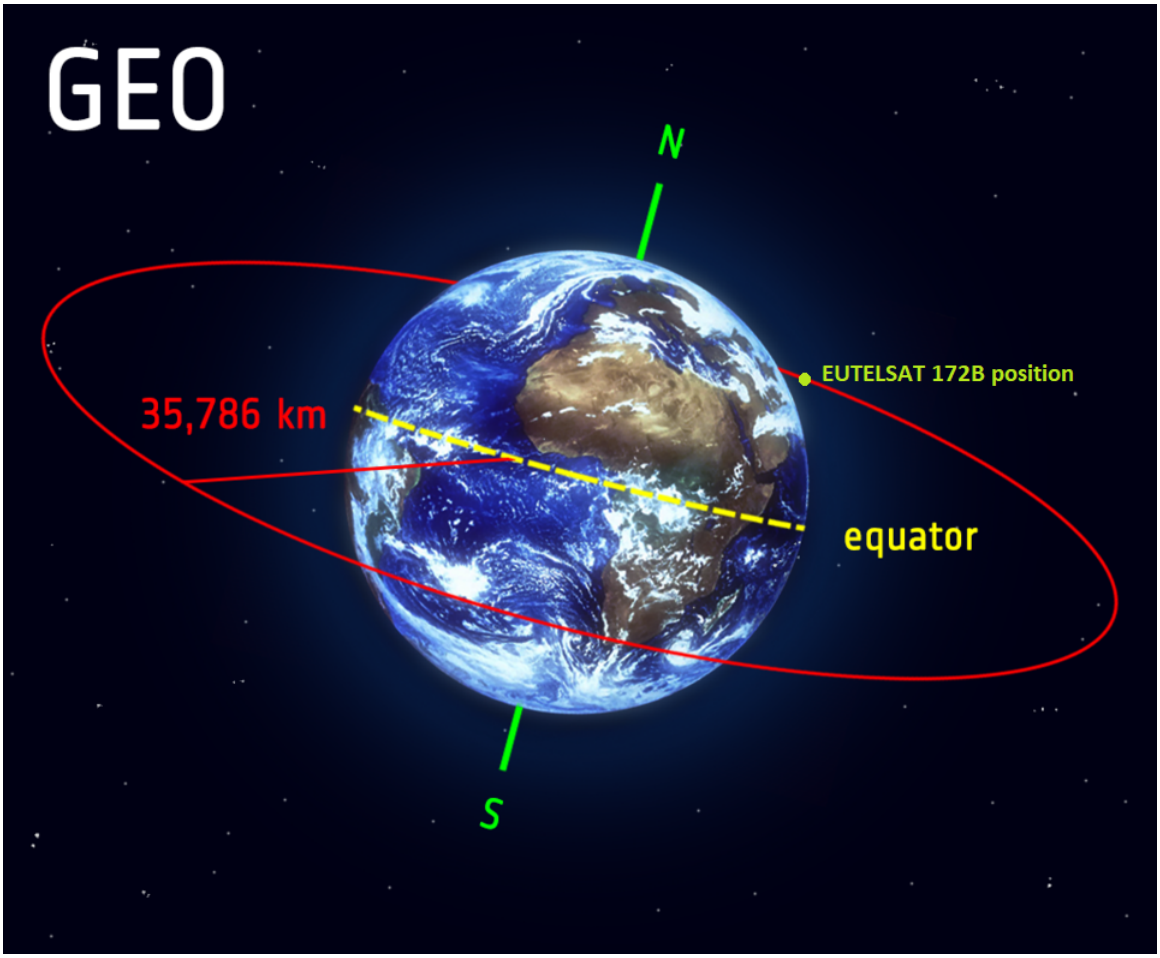

Figure 2.3: Eutelsat GEO orbit [Credit ESA [2]]

dimension	measure	unit
l_{xSA}	3.7	m
l_{ySA}	18	m
l_{zSA}	0.15	m
m_{SA}	67.13	kg
A	67.37	m^2

Table 2.2: Solar array physical properties

position of the left and right CoM solar array with respect to the body reference frame are described respectively in table 2.3 and 2.4[11]

2.2 Electrical Power Subsystem (EPS)

The Electrical Power Subsystem (EPS) provides, stores, distributes and controls satellite electrical power as described in Figure 2.5. The EPS is sized in order to provide the necessary power from the Begin of Life (BoL) to the End of Life (EoL). For sizing the

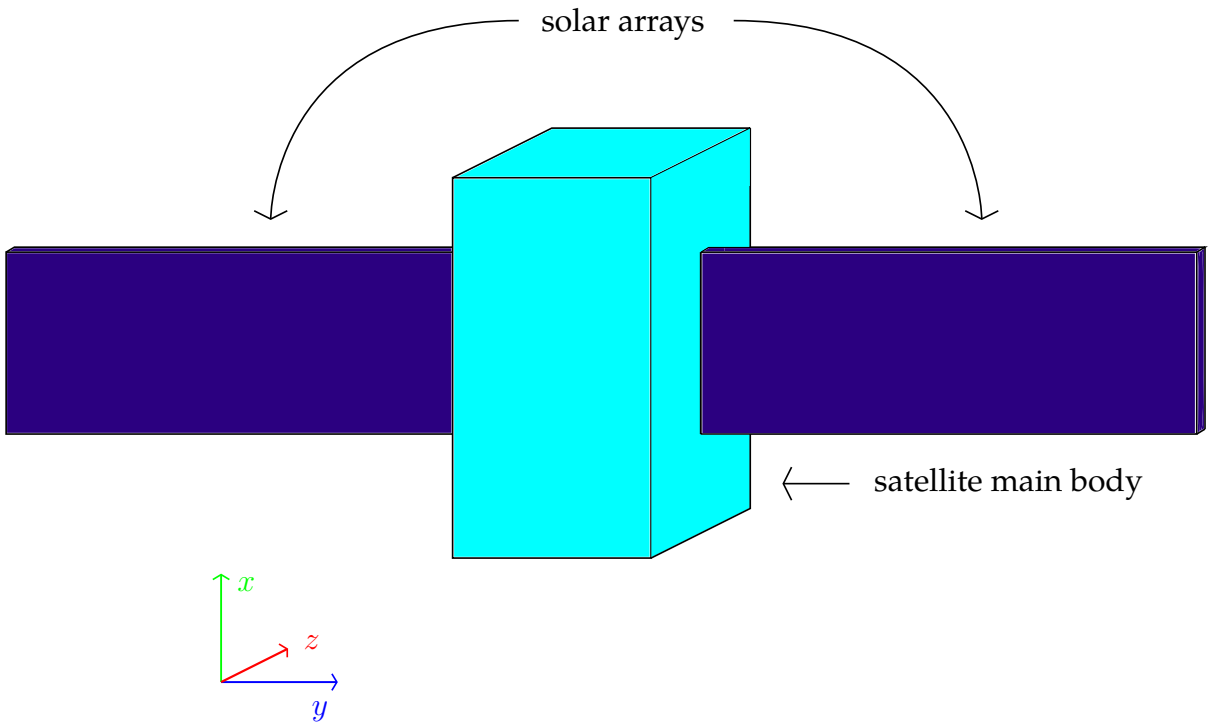

Figure 2.4: EUTELSAT scheme

dimension	measure	unit
x^L_{gSA}	0	m
y^L_{gSA}	$-l_y/2 - l_{ySA}/2$	m
z^L_{gSA}	0	m

Table 2.3: Left solar array CoM

dimension	measure	unit
x^R_{gSA}	0	m
y^R_{gSA}	$l_y/2 + l_{ySA}/2$	m
z^R_{gSA}	0	m

Table 2.4: Right solar array CoM

EPS, in addtion to BoL and EoL requirements other parameters shall be taken into account such as the mission type, mission lifetime, spacecraft configuration and payload definition [24].

2.2.1 EPS architecture

The typical EPS architecture is shown in Figure 2.6. The components function are reported in [24] and listed hereafter:

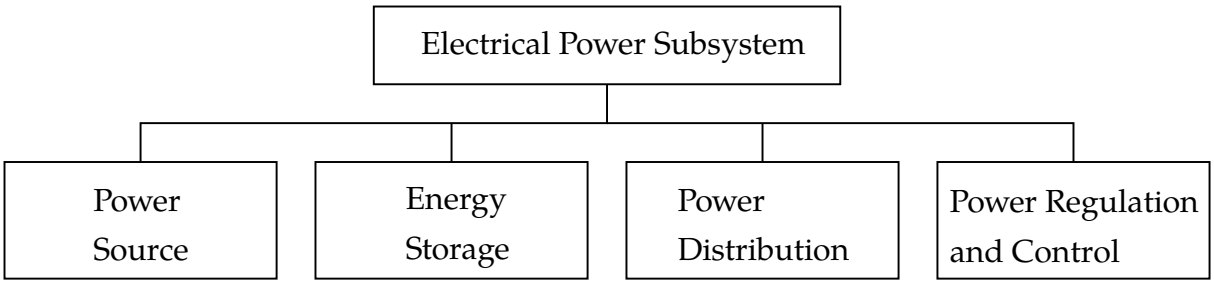

Figure 2.5: EPS functional diagram

- Solar arrays: producing of electrical power by converting solar energy
- Batteries: storing energy to be distributed when eclipse occurs or when the solar array power production is not sufficient to power the required loads
- Shunts: regulating the bus voltage by dissipating the exceeding power produced by the solar array
- Power Charge Regulator and Power Dis-charge Regulator (PCPPDR): controlling the charge and discharge of the batteries
- Power Distribution Unit (PDU): managing the load activation state and manages the fault detection and recovery
- Mode controller: deciding the active power sources and regulating the power flow to the PDU

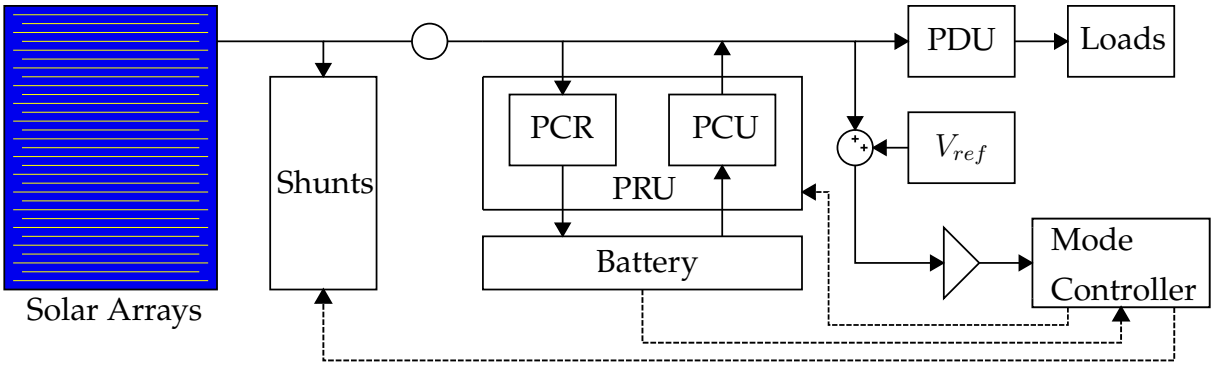

Figure 2.6: EPS architecture

2.2.2 Solar arrays and SADA

The solar cells of the EUTELSAT 172B are SpectroLab Ultra Triple Junction (UTJ) GaAs solar cells. These type of cells are specific made for space environment and they feature a maximum efficiency of 28.3% at BoL and 24.3% at EoL [25].
The solar arrays, as the definition suggests, are an combination of multiple solar cells connected in parallel and series. There are 319 strings connected in parallel of 66 cells

connected in series, resulting in 21054 cells mounted on each surface. The solar cells are mounted on both sides the two panels. The maximum active solar surface during the mission is equivalent to 134.74 m^2.

The Solar Array Drive Actuator (SADA) system is responsible for the rotation of the solar arrays and the power transfer from the solar cells to the EPS subsystem. The SADA system main components are: a Permanent Magnet Synchronous Motor (PMSM) for the motion and a series of slip rings for the power transfer. The power consumption of this system is generally low. For example the Ruag SEPTA 24, shown in figure 2.7, that is designed to fit in satellites similar in size with Eutelsat 172B, has a peak power consumption of 60 W [26].

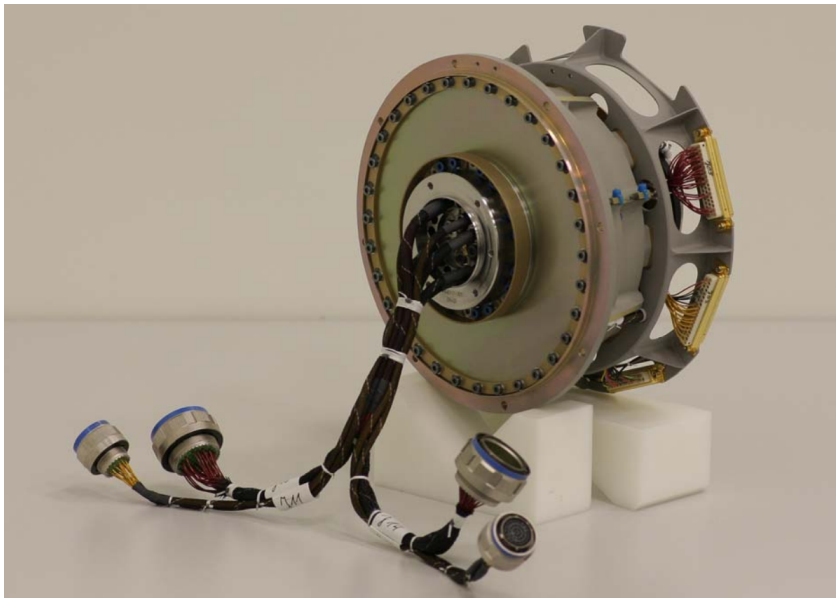

Figure 2.7: Ruag Septa 24 [credit Ruag Space]

2.3 Propulsion system

The propulsion subsystem is responsible for all the satellite maneuvers needed from the orbit raising phase to the operational phase [24]. The orbital control system is assumed to be decoupled from attitude control in this thesis. Hence, the propulsion subsystem is divided in two subsystems, one for the orbital control and the other for the attitude control.
The peculiarity of the Eutelsat 172B is that it is designed to mount Hall Effect Thruster (HET). This type of electrostatic thruster utilizes a cross-field discharge described by the Hall effect to generate the plasma. An electric field established perpendicular to an applied magnetic field electrostatically accelerates ions to high exhaust velocities, while the transverse magnetic field inhibits electron motion that would tend to short out the electric field. HET efficiency and specific impulse is somewhat less than that achievable in ion thrusters, but the thrust at a given power is higher and the device is

much simpler and requires fewer power supplies to operate [27]. The propellant fluid used to supply the HETs is Xenon and it is stored in a tank inside the main body.

2.3.1 Orbital propulsion

Orbital propulsion, as the name suggest, is the propulsion subsystem devoted for the orbital maneuvers. The Eutelsat 172B mounts four Fakel SPT140D, each one connected to the main body by a two axes gimbal system called Thruster Pointing Mechanism (TPM) [11]. An image of the Fakel unit in action is shown in figure 2.8. This thruster is a mid-sized HET which characteristics are reported in table 2.5.

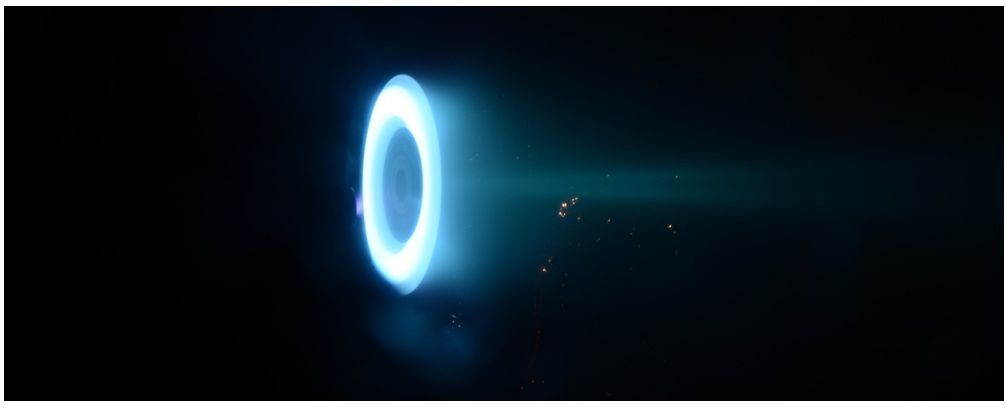

Figure 2.8: Fakel SPT140 Hall effect thruster [credit SSL]

parameter	value	unit
thrust range	170-290	mN
I_{sp}	900-1900	s
power	3-5	kW

Table 2.5: SPT140 characteristics [28]

This thruster is employed for the orbit raising maneuvers from Low Earth Orbit (LEO) to GEO and for the station keeping maneuvers [23]. Electric thrusters for station keeping create a low level of disturbance with respect to the chemical rocket thrusters, due to the lower levels of produced force, the lower speed of the manouvers and the possibility to modify the orientation of the station keeping thrusters, thanks to the TPM [22].

2.3.2 Attitude propulsion

The original design of the Eutelsat 172B employed four reaction wheels for the attitude control of the satellite [11]. The attitude control actuator system proposed in this thesis is the attitude propulsion subsystem, which is composed by mini-HETs. Typically the HET thruster is commanded as on/off actuator with constraints on firing time, shutdown time and switching frequency [14]. By employing this attitude propulsion system instead of the standard reaction wheel we eliminate the typical problems related

parameter	value	unit
dynamic thrust range	10-390	μN
I_{sp}	1500-6000	s
power	5-40	W

Table 2.6: Enpulsion NANO R^3 characteristics [30]

to reaction wheel, i.e. wheel momentum saturation [15]. In this thesis work the mini-HET operational use is simplified. The thrust range for each actuator is considered between zero and it maximum thrust value and time related constraints are neglected. The thruster arrangement is based on the general guidelines of the chemical thrusters [29]. The thrusters are located such that the ion beams generated avoid collisions with the solar arrays and the antennas. The position and direction of the thrusters is shown in figure 2.9.

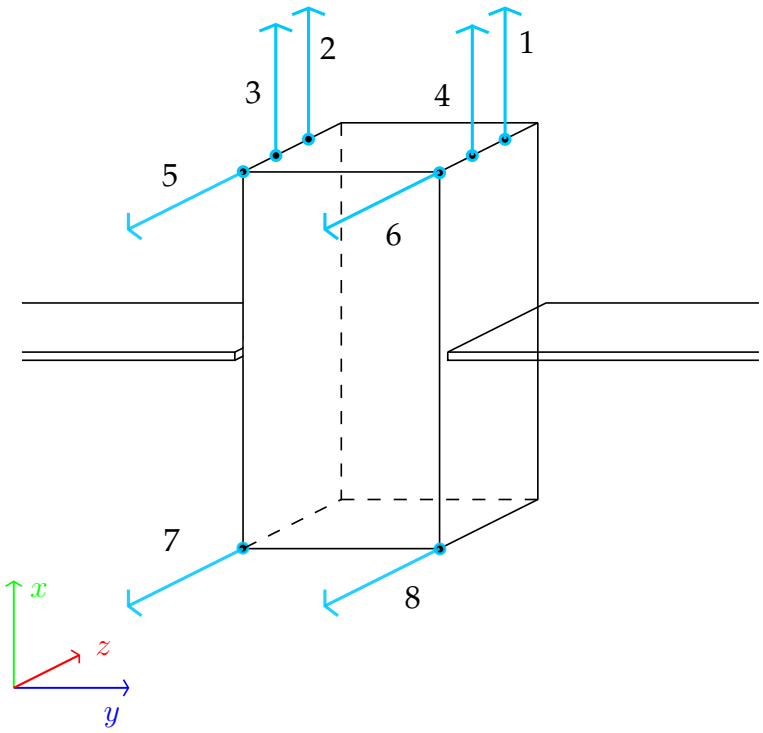

Figure 2.9: Satellite thrusters scheme

The selected thruster is the Enpulsion Nano 3R, shown in figure 2.10, which features the specifications reported in table 2.6.
There are 8 thruster positions, as shown in figure 2.9, each including 4 thrusters. The thrust range produced by this thruster configuration is compatible with thrust required by the control as it will be described in section 4.9.

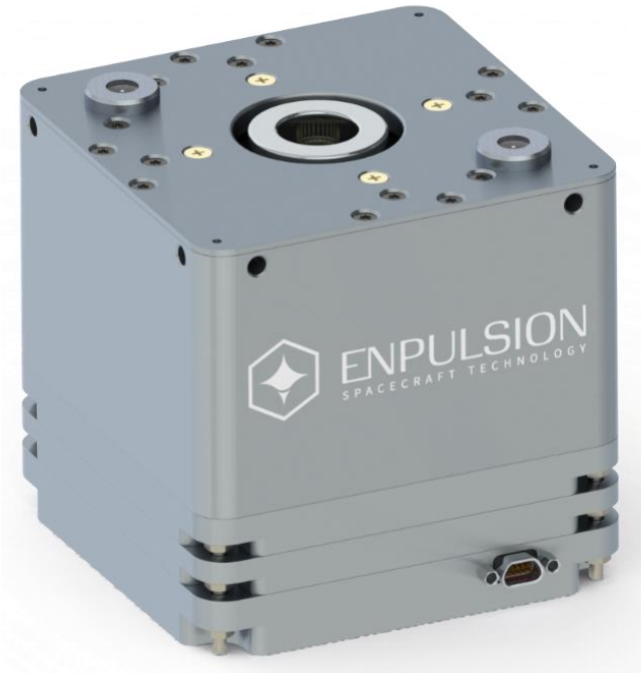

Figure 2.10: Enpulsion NANO R^3 [credit Enpulsion GmbH]

Chapter 3

Space Environment Modeling

This chapter is devoted to the space environment description. The sun relevant information, the reference frames and the main sources of disturbances are presented. The reference book for this chapter is [3].

3.1 Space reference frames

The satellite motion can be described exploiting different reference frames. In general, a reference frame is specified by the location of its origin and the orientation of its coordinate axes. Hereafter, the reference frames used in the follows are presented.

3.1.1 Rotations

Define two reference frames: the fixed reference frame whose axes are $\{\mathbf{e}_1, \mathbf{e}_2, \mathbf{e}_3\}$ and the mobile reference frame whose axes are $\{\boldsymbol{\epsilon}_1, \boldsymbol{\epsilon}_2, \boldsymbol{\epsilon}_3\}$.

The rotation operator $\mathbf{R}$ applied to a vector $\mathbf{u}$ represented in the fixed reference frame returns the representation of the vector $\mathbf{u}$ in the mobile reference frame.

$$\mathbf{v}_\epsilon = \mathbf{R}\mathbf{v}_e \tag{3.1}$$

The inverse of rotation matrix is called the transformation matrix and performs the opposite operation, ie returns the representation of a vector $\mathbf{u}$, represented in the mobile reference frame, into the fixed reference frame

$$\mathbf{v}_e = \mathbf{T}\mathbf{v}_\epsilon \tag{3.2}$$

The columns of the transformation matrix $\mathbf{T}$ are the axis of the mobile frame with respect to the fixed frame. The matrix $\mathbf{T}$ is also known as the Direct Cosine Matrix (DCM).

3.1.2 Earth Centered Intertial reference frame

The Earth Centered Intertial (ECI) reference frame is an approximated inertial frame that has its origin at the center of mass of the Earth. This frame has a linear acceleration due to the Earth orbit around the Sun. The axes are fixed with respect to the stars.

- x-axis: points towards the inertial reference direction (fixed stars)
- z-axis: points towards the north pole
- y-axis: completes the right hand triad

The axes are depicted in Figure 3.1 and are denoted as $\{\mathbf{i}_1, \mathbf{i}_2, \mathbf{i}_3\}$. This reference frame is the basis for the attitude dynamics equations.

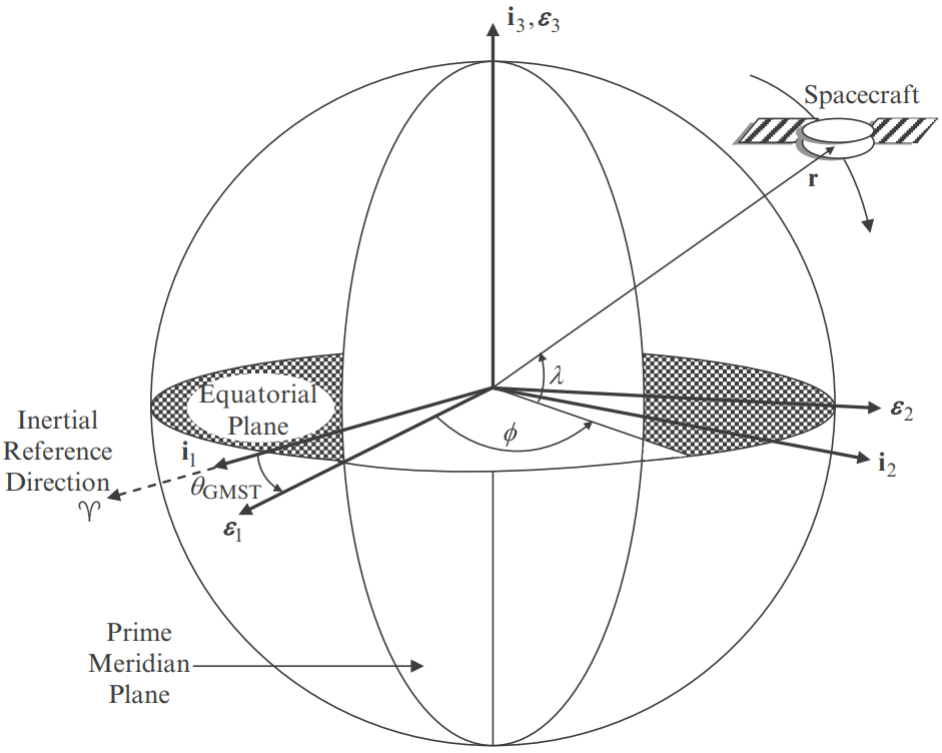

Figure 3.1: Definition of reference frames ECEF ε_i, ECI $\boldsymbol{i}_i$ (Figure 2.3 [3])

3.1.3 Earth Centered Earth Fixed reference frame

The Earth Centered Earth Fixed (ECEF) reference frame has the z-axis in common with the ECI reference frame. The x-axis and y-axis solidly rotates with the Earth. The x-axis points in the direction of the Earth's prime meridian and the y-axis completes the right handed triad. The rotation angle is known as the Greenwich Mean Sideral Time (GMST) angle and it is denoted as θ_{GMST}. The axes are denoted as $\{\varepsilon_1, \varepsilon_2, \varepsilon_3\}$ and are depicted in Figure 3.1.
The transformation of a position vector $\mathbf{r}_I$ from its ECI representation to its ECEF representation $\mathbf{r}_E$ is given by

$$\mathbf{r}_I = \mathbf{T}_{IE}\mathbf{r}_E = \begin{bmatrix} \cos(\theta_{GMST}) & -\sin(\theta_{GMST}) & 0 \\ \sin(\theta_{GMST}) & \cos(\theta_{GMST}) & 0 \\ 0 & 0 & 1 \end{bmatrix} \mathbf{r}_E \tag{3.3}$$

To determine the GMST angle the Julian Date (JD) is required, which is defined by equation 3.13. The equation to compute the angle θ_{GMST} can be find [3] section 2.6.3.

3.1.4 Local Vertical Local Horizontal reference frame

For nadir pointing satellites, as the one considered in this work, it is important to define a reference frame referenced to the satellite orbit. The most common frame is the Local Vertical Local Horizontal (LVLH) orbit frame, shown in Figure 3.2, centered in the satellite CoM. The z-axis $\mathbf{o}_3$ vector is pointing along the nadir vector, directly toward the center of the Earth from the satellite. The y-axis $\mathbf{o}_2$ is pointing along the negative orbit normal, in the direction opposite to the satellite orbital angular velocity. The x-axis $\mathbf{o}_1$ completes the right-handed triad. The representations of these vectors in an inertial frame ECI are

$$\mathbf{o}_3 = -\frac{\mathbf{r}_{ECI}}{\|\mathbf{r}_{ECI}\|} \quad \mathbf{o}_2 = -\frac{(\mathbf{r}_{ECI} \times \mathbf{v}_{ECI})}{\|\mathbf{r}_{ECI} \times \mathbf{v}_{ECI}\|} \tag{3.4}$$

$$\mathbf{o}_1 = \mathbf{o}_2 \times \mathbf{o}_3 = \frac{(\mathbf{r}_{ECI} \times \mathbf{v}_{ECI}) \times \mathbf{r}_{ECI}}{\|\mathbf{r}_{ECI}\|\|\mathbf{r}_{ECI} \times \mathbf{v}_{ECI}\|} \tag{3.5}$$

where $\mathbf{r}_{ECI}$ and $\mathbf{v}_{ECI}$ are the spacecraft position and velocity in the ECI frame. The transformation matrix from the LVLH frame to the ECI frame can be expressed as

$$\mathbf{T}_{LI} = \begin{bmatrix} \mathbf{o}_1 & \mathbf{o}_2 & \mathbf{o}_3 \end{bmatrix} \tag{3.6}$$

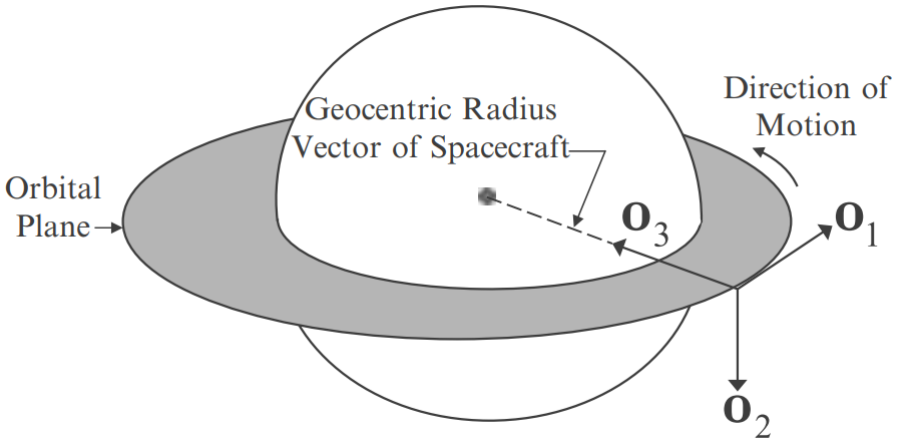

Figure 3.2: Definition of reference frames LVLH (Figure 2.5 [3])

3.1.5 Perifocal Reference Frame

The PQW is a Cartesian coordinate system fixed in space and centered at the focus of the orbit. For circular orbit, such as GEO orbit, the focus coincides with the orbit center. Its xy plane coincides with the orbit plane, and its x-axis is directed from the focus through the periapsis, as illustrated in figure 3.3. The unit vector along the x-axis (the apse line) is denoted $\mathbf{p}$. The z-axis, with unit vector $\mathbf{w}$, is normal to the plane of the orbit in the direction of the angular momentum vector $\mathbf{h}$. The y-axis, with unit vector $\mathbf{q}$, completes the right hand triad. The true anomaly ν is the angle between the x-axis and the current position of the body as in Figure 3.4. In the PQW frame, the position vector $\mathbf{r}$ is written as

$$\mathbf{r} = x\mathbf{p} + y\mathbf{q} \tag{3.7}$$

where the scalar components are defined as

$$x = \|\mathbf{r}\|\cos(\nu) \quad y = \|\mathbf{r}\|\sin(\nu) \tag{3.8}$$

The velocity can be computed by taking the time derivative of $\mathbf{r}$

$$\mathbf{v} = \dot{\mathbf{r}} = \dot{x}\mathbf{p} + \dot{y}\mathbf{q} \tag{3.9}$$

Thus the scalar components are defined by

$$\begin{cases} \dot{x} &= \dot{r}\cos(\theta) - r\dot{\theta}\sin(\theta) \\ \dot{y} &= \dot{r}\sin(\theta) + r\dot{\theta}\cos(\theta) \end{cases} \tag{3.10}$$

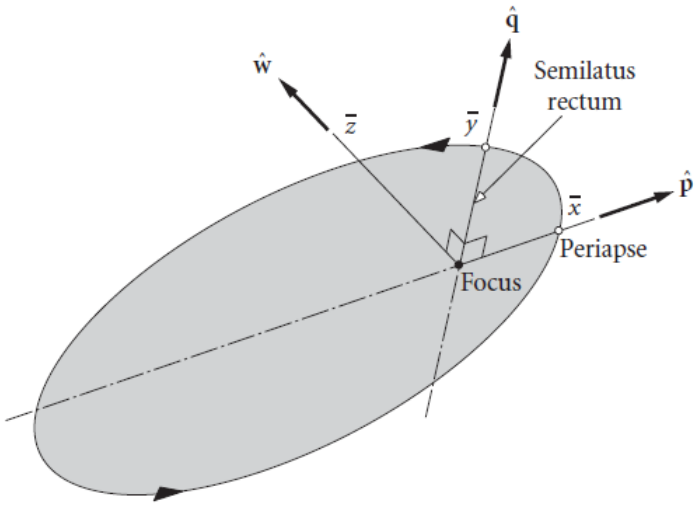

Figure 3.3: Definition of reference frames PQW (Figure 2.29 [4])

3.1.6 Body and Solar array reference frame

The satellite under analysis can rotate its solar arrays around its body y-axis, thus two different frame have been defined. The first reference frame is the one attached to the satellite body and its direction are defined as shown in Figure 3.5.

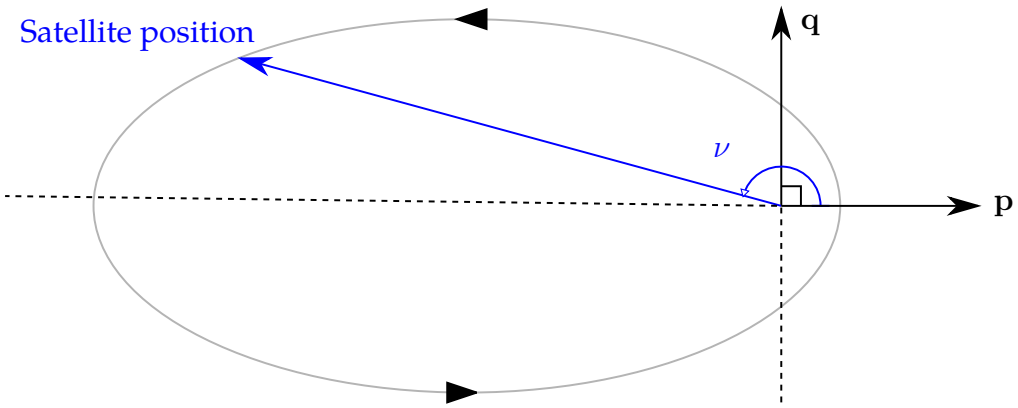

Figure 3.4: PQW reference frame 2D view

- x-axis : is parallel to the payload normal vector in opposite direction
- y-axis : points along solar array rotations axis
- z-axis : completes the right handed triad

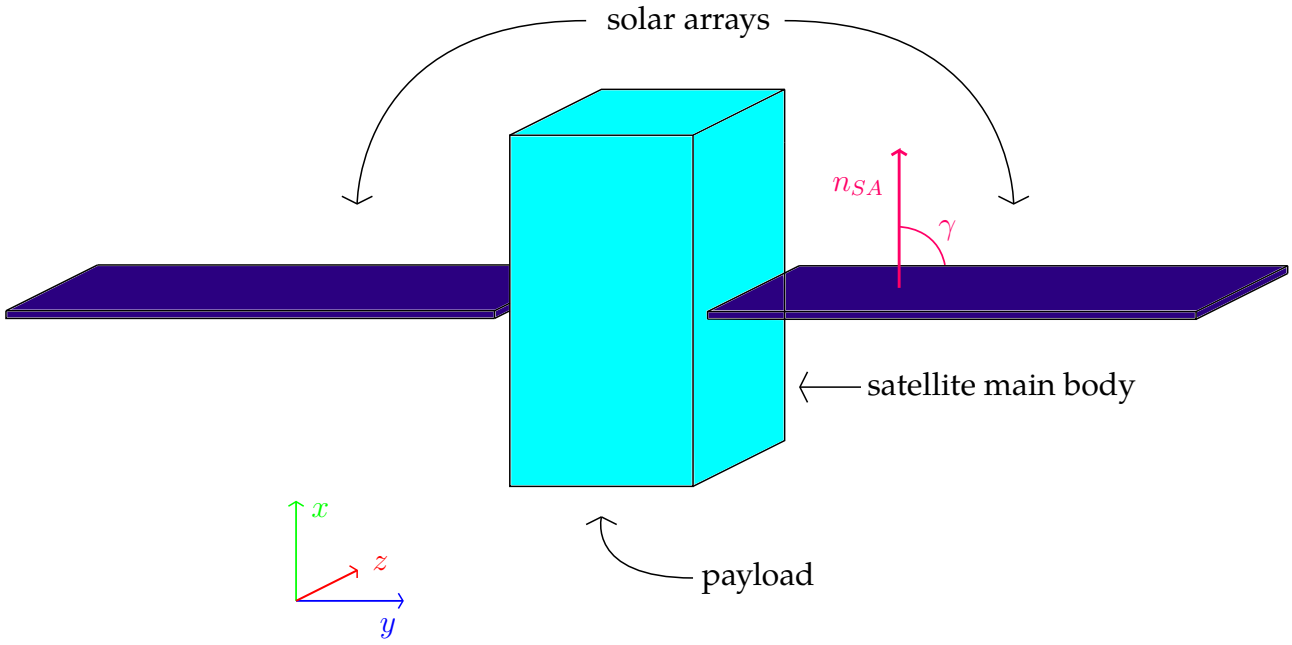

Figure 3.5: Satellite multibody scheme

For the solar arrays, as mentioned before, the rotation angle is γ. The reference frame of the solar arrays origin coincides with the body reference frame origin. When the angle $\gamma = 0$ the solar array reference frame coincides with the body reference frame. The normal vector of the solar array $\mathbf{n}_{SA}$ in the solar array frame is

$$\mathbf{n}_{SA} = \begin{bmatrix} 0 \\ 0 \\ 1 \end{bmatrix} \tag{3.11}$$

The transformation matrix that relates the two reference frames is

$$\mathbf{r}_B = \mathbf{T}_{BSA}\mathbf{r}_{SA} = \begin{bmatrix} \cos(\gamma) & 0 & \sin(\gamma) \\ 0 & 1 & 0 \\ -\sin(\gamma) & 0 & \cos(\gamma) \end{bmatrix} \mathbf{r}_{SA} \tag{3.12}$$

3.2 Sun relevant information

3.2.1 Sun position

The relative position of the Sun with respect to Earth is necessary to determine all the quantities related to the Sun interaction with the Earth and the satellite.
The position of the Sun with respect to the Earth can be determined using the DE405 Ephemeris model computed by the Jet Propulsion Laboratory (JPL) [31]. The model consists of numeric representations of positions, velocities and accelerations of main Solar System bodies, tabulated at equally spaced intervals of time, covering a specified span of years. Specifically the DE405 covers a period of time that range from year 1660 to year 2200. The input required to access the data of DE405 is the JD. The JD at time $t = [Y, M, G, h, m, s]$ is given by

$$\begin{aligned} JD(Y, M, D, h, m, s) = 1721013,5 + 367Y - \text{INT}\left\{\frac{7}{4}\left[Y + \text{INT}\left(\frac{M+9}{12}\right)\right]\right\} \\ + \text{INT}\left(\frac{275M}{9}\right) + D + \frac{3600h + 60m + s}{86400} \end{aligned} \tag{3.13}$$

3.2.2 Satellite solar eclipse

The satellite solar eclipse occurs when the satellite is shadowed by the Earth, which fully blocks sunlight. This occurs when the Sun, Earth and satellite are in a particular alignment condition. Given the position vector of the spacecraft and the Sun with respect to Earth, the eclipse condition can now be determined. The method assume that the shadow created by the Earth is a cylindrical projection of the Earth's diameter along the direction of the Sun to the Earth as can be seen in Figure 3.6.
In the cylindrical approximation the spacecraft is shadowed if and only if

$$r = \|\mathbf{r}_{ECI}\|, \quad \mathbf{e} = \frac{\mathbf{s}_{ECI}}{\|\mathbf{s}_{ECI}\|}, \quad \mathbf{r}_{ECI} \cdot \mathbf{e} < -\sqrt{r^2 - R_\oplus^2} \tag{3.14}$$

where $\mathbf{e}$ is the unit vector direction from the Earth to the Sun, $\mathbf{r}_{ECI}$ is the spacecraft position vector with respect to Earth, r is the spacecraft distance from the Earth's center and $R_\oplus$ is the equatorial radius of the Earth.
Based on data of the orbit of the Earth around the Sun and the orbit of the satellite, eclipse status and duration can be computed. Figure 3.7 shows the result of the eclipse occurrences and duration for the Eutelsat 172B. The computation of these quantities is carried out using the tool provided in [32].

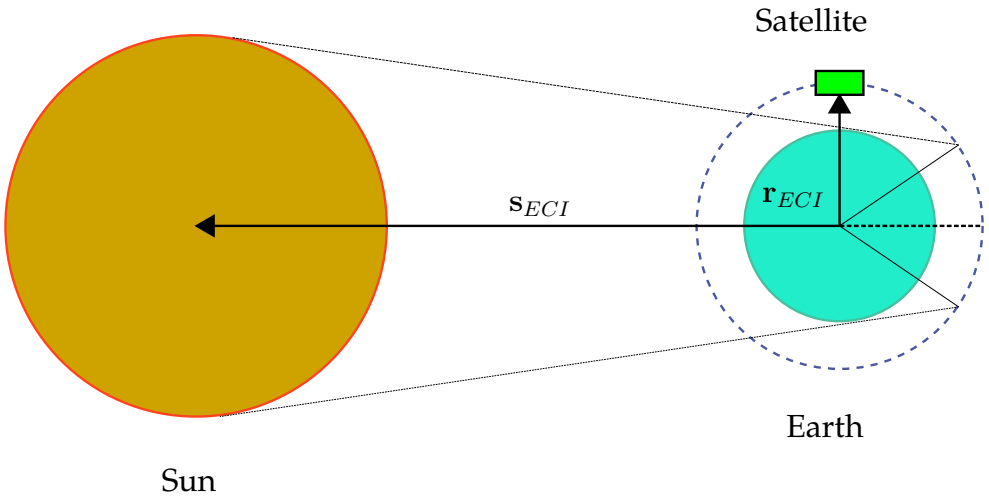

Figure 3.6: Eclipse scheme

3.2.3 Solar radiation

Solar radiation is the main source for the energy production, but it is also a source of disturbance as it will be described later in subsection 3.3.2. This quantity strictly depends on the distance between the object and the Sun. The solar radiation received by an object distant r_{sat} from the sun is given by

$$P_{\odot} = \frac{\mathcal{F}_{\odot}}{c r_{sat}^2} \tag{3.15}$$

where $\mathcal{F}_{\odot}$ is the solar constant, which is the sun irradiance at 1 Astronomical Unit (AU) and c is the speed of light.

3.3 Spacecraft disturbances

The spacecraft environment generate disturbance torques acting on the satellite. The main sources of disturbance torque are presented in this section.

3.3.1 Aerodynamic drag torque

Aerodynamic disturbances are caused by non-conservative forces produced by the satellite relative motion with respect to a surrounding fluid. Aerodynamic drag torque is computed by modeling the spacecraft as a collection of N plates of area S_i and outward normal unit vector $\boldsymbol{n}_B^i$ expressed in the spacecraft body-fixed frame. The torque depends on the velocity of the spacecraft relative to the atmosphere. Assuming that the atmosphere corotates with the Earth, the relative velocity in ECI frame is defined as

$$\mathbf{v}_r = \mathbf{v}_{ECI} + \boldsymbol{\omega}_E \times \mathbf{r}_{ECI} \tag{3.16}$$

where $\mathbf{v}_{ECI}$ is the satellite velocity in ECI, $\mathbf{r}_{ECI}$ is the position of the satellite in ECI and $\boldsymbol{\omega}_E$ is the Earth angular velocity. The inclination of the i-th plate with respect to the

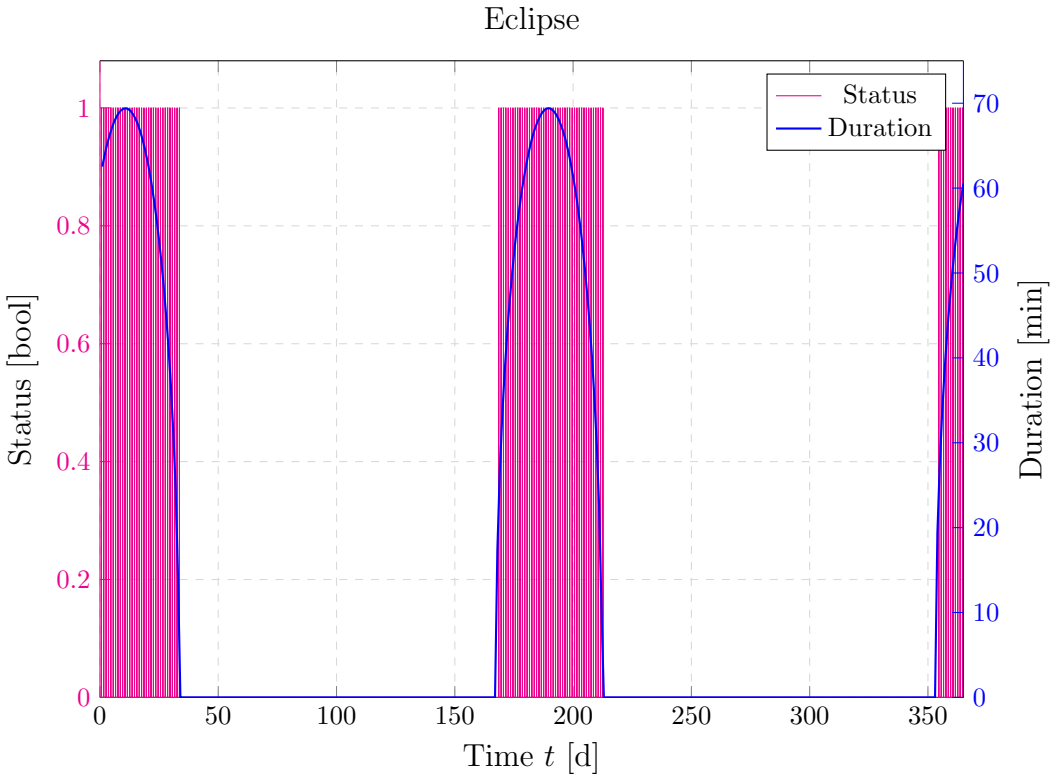

Figure 3.7: Eclipse occurrences and duration

relative velocity is given by

$$\cos\theta^i = \frac{\mathbf{n}_B^i \cdot \mathbf{v}_r}{\|\mathbf{v}_r\|} \tag{3.17}$$

The aerodynamic force acting on the i-th plate can be computed as

$$\mathbf{F}_{aero}^i = -\frac{1}{2}\rho C_D \|\boldsymbol{v}_r\| \boldsymbol{v}_r S_i \max(\cos\theta^i, 0) \tag{3.18}$$

where ρ is the atmospheric density and C_D is the drag coefficient. The coefficient C_D is determined empirically. The employed atmospheric density model is the exponential atmospheric model described in section D.2 of [3]. Given the force acting on the panels and the panel center positions the aerodynamic torque acting on the i-th panel is given by

$$\mathbf{T}_{aero}^i = \mathbf{r}_i \times \mathbf{F}_{aero}^i \tag{3.19}$$

where $\mathbf{r}_i$ is the position of the center of the i-th plate with respect to the body reference frame.

3.3.2 Solar Radiation Pressure

Solar Radiation Pressure (SRP) is another non-conservative force acting on spacecraft caused by the Sun radiation. It generally outweigh drag perturbation in higher altitude orbits (more than 800 km). The mechanism by which SRP affects the orbit of a spacecraft is through momentum exchange between the spacecraft and photons incident on the spacecraft. Because of this, SRP only contributes as times when the spacecraft is not shadowed by the Earth or other bodies [3]. As for aerodynamic disturbances, the satellite is modeled as a set of N flat plates of area S_i and normal direction $\mathbf{n}_B^i$. There are some material depending parameters entering the model: the specular reflection coefficient R_{spec}^i, the diffuse reflection coefficient R_{diff}^i and the absorption coefficient R_{abs}^i. The spacecraft to sun unit vector in the body reference frame is defined as $\mathbf{s}$. Given vector $\mathbf{s}$ and the normal plate direction $\mathbf{n}_B^i$, the angle between the sun vector and the normal to the i-th plate is given by

$$\cos\theta_{SRP}^i = \mathbf{n}_B^i \cdot \mathbf{s} \tag{3.20}$$

then, the force on the i-th plate can be computed as

$$\mathbf{F}_{SRP}^i = -P_\odot S_i \left[2\left(\frac{R_{diff}^i}{3} + R_{spec}^i \cos\theta_{SRP}^i \right) \mathbf{n}_B^i + (1 - R_{spec}^i)\mathbf{s} \right] \max(\cos\theta_{SRP}^i, 0) \tag{3.21}$$

where $P_\odot$ is defined in Equation 3.15. The SRP torque on i-th plate of the satellite is then

$$\mathbf{L}_{SRP}^i = \sum_i \mathbf{r}_i \times \mathbf{F}_{SRP}^i \tag{3.22}$$

where $\mathbf{r}_i$ is the position of the center of the i-th plate with respect to the body reference frame.

3.3.3 Magnetic dipole

The liquid iron core of the Earth works like a large dynamo creating a magnetic field around the planet. The field is large enough to be relevant for space flight. Any interaction with a satellite Residual Magnetic Dipole Moment (RDM) generates a torque that has an influence on the attitude. Satellites have a typical RDM range of 0.1 - 20 $\mathrm{A\,m^2}$. The satellite's RDM value can be in the higher range especially in high power satellites, such as Eutelsat 172B [33, 34]. The torque generated by a magnetic dipole $\mathbf{m}$ in a magnetic field $\mathbf{B}$ is given by

$$\mathbf{L}_{mag} = \mathbf{m} \times \mathbf{B}_B \tag{3.23}$$

The most basic source of a magnetic dipole is a current loop. A current of I amperes flowing in a planar loop of area A produces a dipole of magnitude $m = AI$ in the direction normal to the plane of the loop and satisfying the right hand rule. The value of $\mathbf{m}$ can not determined easily due to the complexity of the EPS arrangement. The value of $\mathbf{m}$ also varies during time since it depends on the currents flowing into the EPS

thus depending on instantaneous satellite power requirements. Another important quantity to be determined to compute the magnetic torque is the magnetic field vector. The model used to compute the magnetic field is Internationl Geomagnetic Reference Field (IGRF). The outcome of the IGRF is given in the ECEF reference frame; since the magnetic field $\mathbf{B}_E$ shall be referenced to the body frame the quantity is converted to the body reference frame by using

$$\mathbf{B}_B = \mathbf{T}_{BE}\mathbf{B}_E \tag{3.24}$$

3.3.4 Gravity gradient

An object orbiting around a planet experiences different gravitational attraction in distinct parts of it depending on their distance from the center of the planet. This force is relatively weak but it helps stabilizing the satellite in body vertical orientation relative to the nadir orientation. Hence, this phenomenon can help the attitude control of nadir pointing satellites like Eutelsat 172B. The gravity gradient torque is computed by summing the contribution of the gravitational forces on the various point masses constituting the rigid body. The gravitational force acting on the $i-$th particle is assuming first order variation in the gravitational field

$$\mathbf{F}^i = m_i\mathbf{g}(\mathbf{r_i^c} + \mathbf{r_c^0}) = m_i[\mathbf{g}(\mathbf{r_c^0}) + G(\mathbf{r}_c^0)\mathbf{r}_i^c] \tag{3.25}$$

where the term $G(\mathbf{r}_c^0)$ is the gravity gradient tensor evaluated at the center of mass of the satellite, m_i is the discrete mass in position $\mathbf{r_i^c}$ relative to the satellite center of mass and $\mathbf{g}(\mathbf{r_i})$ is the gravitational field in position $\mathbf{r_i}$ relative to the ECI reference system. The resulting torque generated by these forces is

$$\mathbf{M}_{gg} = \sum_i m_i\mathbf{r^{ic}} \times [G(\mathbf{r}_c^0)\mathbf{r}_i^c] \tag{3.26}$$

In the case of spherical gravity field the gravity gradient tensor can be modeled as

$$G(\mathbf{r}) = \frac{\mu}{r^3}\left(I_3 - 3\frac{\mathbf{r}\mathbf{r}^T}{r^2}\right) \tag{3.27}$$

When nadir vector is available, some simplification can be made. Let $\mathbf{r}_c^0 = -r\mathbf{n}_{nad}$, the resulting torque is

$$\mathbf{M}_{gg} = \frac{3\mu}{r^3}\mathbf{n}_{nad} \times \sum_{i=1}^{n} m_i[\|\mathbf{r}_i^c\|^2\mathbf{I} - (\mathbf{r}_i^c)(\mathbf{r}_i^c)^T]\mathbf{n}_{nad} = \frac{3\mu}{r^3}\mathbf{n}_{nad} \times (\mathbf{J}\mathbf{n}_{nad}) \tag{3.28}$$

where $\mathbf{I}$ is the identity matrix and $\mathbf{J}$ is the tensor of inertia of the satellite.

Chapter 4

Satellite modeling

This chapter is focused on the modeling of the satellite. Hereafter the dynamical model of the satellite, the satellite actuators and the analysis of the trajectory and the disturbances will be presented.

The satellite can rotate the solar panels and this feature cannot be effectively model by means of single rigid body model, thus a more complex model including this feature is derived. The satellite is modeled as an ensemble of three parallelepipeds, the main body and two SA. The spacecraft main body is modeled as a rigid body whose mass varies with the fuel consumption whereas the SA are modeled as fixed mass rigid body. The two SA are rigidly connected by a massless rod passing through the central body which length is equal to the satellite length along y-direction. The rotational joint position that connects the body to the solar arrays is placed at the CoM of the body and coincides with the CoM of the SA.

4.1 Satellite Inertia Tensor

We are interested in the tensors of inertia of the main body and the two sSA. The inertia tensor of a homogeneous parallelepiped is given by

$$\mathbf{I} = \frac{1}{12} m \begin{bmatrix} l_y^2 + l_z^2 & 0 & 0 \\ 0 & l_x^2 + l_z^2 & 0 \\ 0 & 0 & l_x^2 + l_y^2 \end{bmatrix} \tag{4.1}$$

where l_x, l_y and l_z are the parallelepiped edges length along the principal axes and m is the mass of the parallelepiped [35]. The inertia tensor of the main body with respect to its geometrical center is

$$\mathbf{I}_1 = \frac{1}{12}(m_d + m_f(t)) \begin{bmatrix} l_{ySC}^2 + l_{zSC}^2 & 0 & 0 \\ 0 & l_{xSC}^2 + l_{zSC}^2 & 0 \\ 0 & 0 & l_{xSC}^2 + l_{ySC}^2 \end{bmatrix} \tag{4.2}$$

The inertia tensor of the generic SA with respect to its geometrical center is

$$\mathbf{I}_{SA} = \frac{1}{12} m_{SA} \begin{bmatrix} l_{ySA}^2 + l_{zSA}^2 & 0 & 0 \\ 0 & l_{xSA}^2 + l_{zSA}^2 & 0 \\ 0 & 0 & l_{xSA}^2 + l_{ySA}^2 \end{bmatrix} \tag{4.3}$$

By using the Parallel Axis theorem [35] the inertia tensor of both SA with respect to the body reference frame is given by

$$\mathbf{S} = 2\mathbf{I}_{SA} + 2m_{SA} \left(\frac{l_y + l_{SA}}{2} \right)^2 \mathbf{e}_2 \tag{4.4}$$

which is a diagonal matrix and $\mathbf{e}_2 = [\,0\,1\,0\,]$. The SA can rotate around the y-axis by the angle γ thus the inertia tensor considering the rotation of the SA is given by

$$\mathbf{I}_2 = \mathbf{T}(\gamma)\mathbf{S}\mathbf{T}^T(\gamma) \tag{4.5}$$

where $\mathbf{T}$ is the rotation matrix

$$\mathbf{T}(\gamma) = \begin{bmatrix} c_\gamma & 0 & s_\gamma \\ 0 & 1 & 0 \\ -s_\gamma & 0 & c_\gamma \end{bmatrix} \tag{4.6}$$

Thus the inertia $\mathbf{I}_2$ of the second body is defined as

$$\mathbf{I}_2(\gamma) = \begin{bmatrix} S_{11}c_\gamma^2 + S_{33}s_\gamma^2 & 0 & -S_{11}c_\gamma s_\gamma + S_{33}s_\gamma c_\gamma \\ 0 & S_{22} & 0 \\ -S_{11}c_\gamma s_\gamma + S_{33}s_\gamma c_\gamma & 0 & S_{11}s_\gamma^2 + S_{33}c_\gamma^2 \end{bmatrix} \tag{4.7}$$

In the multibody model in section 4.4, some derivatives of the inertia tensors are required in equation 4.39. These quantities, which are the partial derivative of $\mathbf{I}_2$ with respect to γ and the derivative with respect to time of $\mathbf{I}_1$, are reported below

$$\frac{\partial \mathbf{I}_2}{\partial \gamma} = (S_{33} - S_{11}) \begin{bmatrix} s_{2\theta} & 0 & c_{2\theta} \\ 0 & 0 & 0 \\ c_{2\theta} & 0 & s_{2\theta} \end{bmatrix} \tag{4.8}$$

$$\dot{\mathbf{I}}_1 = \frac{1}{12} \dot{m}_p \begin{bmatrix} l_{ySC}^2 + l_{zSC}^2 & 0 & 0 \\ 0 & l_{xSC}^2 + l_{zSC}^2 & 0 \\ 0 & 0 & l_{xSC}^2 + l_{ySC}^2 \end{bmatrix} \tag{4.9}$$

4.2 Spacecraft attitude representation

4.2.1 Euler angles

The Euler angles are a set of orientation parameters that describe a 3D rotation matrix. There are several Euler angles sets that differ from each other by the sequence of rotation axes. In this work a 313 Euler angles (ϕ, θ, ψ) set is employed. Let's define

with XYZ the fixed reference frame and with xyz a mobile one, as in [35]. Then, the sequence of rotation is

- First rotation: rotate the XYZ system to the $x'y'z'$ system through a rotation ϕ about Z

$$\begin{bmatrix} x' \\ y' \\ z' \end{bmatrix} = \begin{bmatrix} c_\phi & s_\phi & 0 \\ -s_\phi & c_\phi & 0 \\ 0 & 0 & 1 \end{bmatrix} \begin{bmatrix} X \\ Y \\ Z \end{bmatrix} = \mathbf{R}_1(\phi) \begin{bmatrix} X \\ Y \\ Z \end{bmatrix} \tag{4.10}$$

- Second rotation: rotate the $x'y'z'$ system to the $x''y''z''$ system through a rotation θ about x'

$$\begin{bmatrix} x'' \\ y'' \\ z'' \end{bmatrix} = \begin{bmatrix} 1 & 0 & 0 \\ 0 & c_\phi & s_\phi \\ 0 & -s_\phi & c_\phi \end{bmatrix} \begin{bmatrix} x' \\ y' \\ z' \end{bmatrix} = \mathbf{R}_2(\theta) \begin{bmatrix} x' \\ y' \\ z' \end{bmatrix} \tag{4.11}$$

- Third rotation: rotate the $x''y''z''$ system to the xyz system through a rotation ψ about z''

$$\begin{bmatrix} x \\ y \\ z \end{bmatrix} = \begin{bmatrix} c_\psi & s_\psi & 0 \\ -s_\psi & c_\psi & 0 \\ 0 & 0 & 1 \end{bmatrix} \begin{bmatrix} x'' \\ y'' \\ z'' \end{bmatrix} = \mathbf{R}_3(\psi) \begin{bmatrix} x'' \\ y'' \\ z'' \end{bmatrix} \tag{4.12}$$

The sequence of rotations is sketched in Figure 4.1. The resulting rotation matrix from the system XYZ to the system xyz is then

$$\mathbf{v}_{xyz} = \mathbf{R}_3(\psi)\mathbf{R}_2(\theta)\mathbf{R}_1(\phi)\mathbf{v}_{XYZ} = \mathbf{R}_{313}(\phi, \theta, \psi)\mathbf{v}_{XYZ} \tag{4.13}$$

The corresponding Direct Cosine Matrix (DCM) of the rotation matrix $\mathbf{R}_{313}$ is

$$\mathbf{v}_{XYZ} = \mathbf{T}_{313}(\phi, \theta, \psi)\mathbf{v}_{xyz} \tag{4.14}$$

where $\mathbf{T}_{313}(\phi, \theta, \psi)$ is

$$\mathbf{T}_{313}(\phi, \theta, \psi) = \begin{bmatrix} c_\phi c_\psi - s_\phi c_\theta s_\psi & -c_\phi s_\psi - s_\phi c_\theta c_\psi & s_\phi s_\theta \\ s_\phi c_\psi + c_\phi c_\theta s_\psi & -s_\phi s_\psi + c_\phi c_\theta c_\psi & -c_\phi s_\theta \\ s_\theta s_\psi & s_\theta c_\psi & c_\theta \end{bmatrix} \tag{4.15}$$

4.2.2 Quaternion

Quaternion are an alternative method to represent 3D rotations. The main differences with respect to the Euler Angles is that the quaternion does not present singularity points and it use four parameters instead of three used in Euler angles. A rotation in the 3D space is completely described by a rotation axis $\mathbf{u}$ and a rotation angle θ by Euler theorem [35]. The quaternion is defined from the tuple $(\mathbf{u}, \theta)$ as

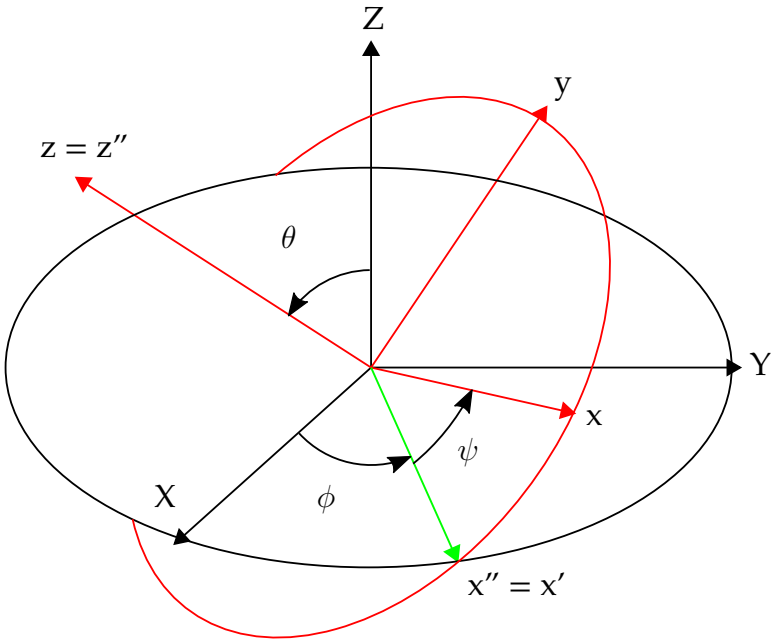

Figure 4.1: Euler angles

$$\mathfrak{q} = \begin{bmatrix} q_0 \\ \mathbf{q} \end{bmatrix} = \begin{bmatrix} q_0 \\ q_1 \\ q_2 \\ q_3 \end{bmatrix} = \begin{bmatrix} \cos(\theta) \\ \mathbf{u}\sin(\theta) \end{bmatrix} = \begin{bmatrix} \cos(\theta) \\ u_1\sin(\theta) \\ u_2\sin(\theta) \\ u_3\sin(\theta) \end{bmatrix} \tag{4.16}$$

The DCM matrix of a quaternion representation is defined as in [3]

$$\mathbf{T}(\mathfrak{q}) = \begin{bmatrix} q_0^2+q_1^2-q_2^2-q_3^2 & 2(q_1q_2-q_0q_3) & 2(q_1q_3+q_0q_2) \\ 2(q_1q_2+q_0q_3) & q_0^2-q_1^2+q_2^2-q_3^2 & 2(q_2q_3-q_0q_1) \\ 2(q_1q_3-q_0q_2) & 2(q_2q_3+q_0q_1) & q_0^2-q_1^2-q_2^2+q_3^2 \end{bmatrix} \tag{4.17}$$

4.2.3 Euler 313 and Quaternion conversions

In the previous Section, the relationship among Euler angles, quaternion and DCM has been described. The inverse relationship, i.e. DCM to Euler angles and quaternion is now described [3]. The first conversion is given by

$$\phi = \text{atan2}(T_{13}, -T_{23}) \quad \theta = \text{atan}\left(\frac{\sqrt{1-T_{33}}}{T_{33}}\right) \quad \psi = \text{atan2}(T_{31}, T_{32}) \tag{4.18}$$

The second conversion is given by

$$q_0 = 0.5\sqrt{T_{11}+T_{22}+T_{33}+1} \quad q_1 = \frac{1}{4q_0}\sqrt{T_{32}-T_{23}} \tag{4.19}$$

$$q_2 = \frac{1}{4q_0}\sqrt{T_{13}-T_{31}} \quad q_3 = \frac{1}{4q_0}\sqrt{T_{21}-T_{12}} \tag{4.20}$$

The transformation between Euler angles and quaternion are performed converting the Euler angles representation to the DCM and then from the DCM the quaternion are obtained. The same process applies for the quaternion to Euler angles conversion.

4.3 Spacecraft attitude kinematics

The spacecraft kinematics equations provide a relationship between the velocities and the position. The satellite pose, which is the set of parameters that uniquely define its position in $\mathbb{R}^3$, is defined using two set of coordinates presented before, i.e. the Euler angles and the quaternions.

The kinematic equations for Euler 313 angles are [35]

$$\begin{bmatrix} \dot{\phi} \\ \dot{\theta} \\ \dot{\psi} \end{bmatrix} = \frac{1}{s_\theta} \begin{bmatrix} s_\psi & c_\psi & 0 \\ s_\theta c_\psi & -s_\theta s_\psi & 0 \\ -c_\theta s_\psi & -c_\theta c_\psi & s_\theta \end{bmatrix} \begin{bmatrix} \omega_1 \\ \omega_2 \\ \omega_3 \end{bmatrix} \tag{4.21}$$

$$\begin{bmatrix} \omega_1 \\ \omega_2 \\ \omega_3 \end{bmatrix} = \begin{bmatrix} s_\theta s_\psi & c_\psi & 0 \\ s_\theta c_\psi & -s_\psi & 0 \\ c_\theta & 0 & 1 \end{bmatrix} \begin{bmatrix} \dot{\phi} \\ \dot{\theta} \\ \dot{\psi} \end{bmatrix} \tag{4.22}$$

The kinematic equations for quaternions are [36]

$$\mathfrak{q} = \frac{1}{2}\mathbf{Q}\boldsymbol{\omega} \quad \text{where} \quad \mathbf{Q} = \begin{bmatrix} -q_1 & -q_2 & -q_3 \\ q_0 & -q_3 & q_2 \\ q_3 & q_0 & -q_1 \\ q_2 & q_1 & q_0 \end{bmatrix} \tag{4.23}$$

Two equivalent kinematics model are presented. The kinematic model based on Euler 313 angles is employed in the attitude dynamics model and in the TRMPC controller, whereas the kinematic model based on quaternion is used in the SMC.

4.4 Spacecraft attitude dynamics

The spacecraft attitude dynamics is usually modeled as rigid body dynamics by the canonical equation

$$\mathbf{I}\dot{\boldsymbol{\omega}} + \boldsymbol{\omega} \times \mathbf{I}\boldsymbol{\omega} = \boldsymbol{\tau} \tag{4.24}$$

where $\mathbf{I}$ is the satellite inertia tensor computed with respect to the body frame centered at the COM and $\boldsymbol{\omega}$ is the angular velocity with respect to the body frame. This model works when the satellite has small articulated components that do not vary the inertia significantly or do not produce significant disturbances. The equation (4.24) is used to simulate the satellite in fixed SA configuration. The SA rotation feature requires a multibody model which is derived in this Section using the Lagrange approach. The

angle γ is the angle of rotation of the SA with respect to the main body. The angular velocity of the main body is $\boldsymbol{\omega}$, whereas the angular velocity of the SA is the angular velocity of the main body plus the angular velocity of the SA with respect to the main body which is $\dot{\gamma}\boldsymbol{e}_2$.
The kinetic energy for the attitude dynamics is the sum of the kinetic energy of the main body and the kinetic energy of the solar arrays since they share the same COM and it can be defined as

$$T = \frac{1}{2}\boldsymbol{\omega}^T\mathbf{I}_1\boldsymbol{\omega} + \frac{1}{2}(\boldsymbol{\omega} + \dot{\gamma}\boldsymbol{e}_2)^T\mathbf{I}_2(\boldsymbol{\omega} + \dot{\gamma}\mathbf{e}_2) \tag{4.25}$$

$$T = \frac{1}{2}\boldsymbol{\omega}^T(\mathbf{I}_1 + \mathbf{I}_2)\boldsymbol{\omega} + \boldsymbol{\omega}^T\mathbf{I}_2\dot{\gamma}\mathbf{e}_2 + \frac{1}{2}\mathbf{e}_2^T\mathbf{I}_2\mathbf{e}_2\dot{\gamma}^2 \tag{4.26}$$

Defining the total inertia as $\mathbf{I}_T = \mathbf{I}_1 + \mathbf{I}_2$, the total kinetic energy of the system becomes

$$T = \frac{1}{2}\boldsymbol{\omega}^T\mathbf{I}_T\boldsymbol{\omega} + \boldsymbol{\omega}^T\mathbf{I}_2\dot{\gamma}\mathbf{e}_2 + \frac{1}{2}\mathbf{e}_2^T\mathbf{I}_2\mathbf{e}_2\dot{\gamma}^2 \tag{4.27}$$

The generalized coordinated are the Euler angles $\mathbf{a} = \begin{bmatrix}\phi & \theta & \psi\end{bmatrix}^T$ and the SA rotation angle γ. The Jacobian matrix $\mathbf{J}$ relates $\boldsymbol{\omega} = \mathbf{J}(\mathbf{a})\dot{\mathbf{a}}$. All the Jacobian matrix derivatives needed for the equations are listed below [3].

$$\mathbf{J}(\mathbf{a}) = \begin{bmatrix} s_\theta s_\psi & c_\psi & 0 \\ s_\theta c_\psi & -s_\psi & 0 \\ c_\theta & 0 & 1 \end{bmatrix} \quad \dot{\mathbf{J}}(\mathbf{a},\dot{\mathbf{a}}) = \begin{bmatrix} \dot{\theta}c_\theta s_\psi + \dot{\psi}s_\theta c_\psi & -\dot{\psi}s_\psi & 0 \\ \dot{\theta}c_\theta c_\psi - \dot{\psi}s_\theta s_\psi & -\dot{\psi}c_\psi & 0 \\ -\dot{\theta}s_\theta & 0 & 0 \end{bmatrix} \tag{4.28}$$

$$\frac{\partial\mathbf{J}}{\partial\theta} = \begin{bmatrix} c_\theta s_\psi & 0 & 0 \\ c_\theta c_\psi & 0 & 0 \\ -s_\theta & 0 & 0 \end{bmatrix} \quad \frac{\partial\mathbf{J}}{\partial\psi} = \begin{bmatrix} s_\theta c_\psi & -s_\psi & 0 \\ -s_\theta s_\psi & -c_\psi & 0 \\ 0 & 0 & 0 \end{bmatrix} \quad \frac{\partial\mathbf{J}}{\partial\phi} = \begin{bmatrix} 0 & 0 & 0 \\ 0 & 0 & 0 \\ 0 & 0 & 0 \end{bmatrix} \tag{4.29}$$

Using Lagrange approach the derivatives with respect to the generalized coordinates and velocities are computed as follows

$$\frac{\partial T}{\partial a_i} = \dot{\mathbf{a}}^T\mathbf{J}^T\mathbf{I}_T\frac{\partial\mathbf{J}}{\partial a_i}\dot{\mathbf{a}} + \mathbf{e}_2^T\mathbf{I}_2\frac{\partial\mathbf{J}}{\partial a_i}\dot{\mathbf{a}}\dot{\gamma} \tag{4.30}$$

$$\frac{\partial T}{\partial \gamma} = \frac{1}{2}\boldsymbol{\omega}^T\frac{\partial\mathbf{I}_2}{\partial\gamma}\boldsymbol{\omega} + \boldsymbol{\omega}^T\frac{\partial\mathbf{I}_2}{\partial\gamma}\mathbf{e}_2 \tag{4.31}$$

$$\frac{\partial T}{\partial \dot{a}_i} = (\mathbf{J})_i^T\mathbf{I}_T\mathbf{J}\dot{\boldsymbol{a}} + (\mathbf{J})_i^T\mathbf{I}_2\mathbf{e}_2\dot{\gamma} \tag{4.32}$$

$$\frac{\partial T}{\partial \dot{\gamma}} = I_2^{22}\dot{\gamma} + \mathbf{e}_2^T\mathbf{I}_2\boldsymbol{\omega} + \mathbf{e}_2^T\frac{\partial\mathbf{I}_2}{\partial\gamma}\boldsymbol{\omega}\dot{\gamma}^2 \tag{4.33}$$

and the derivatives with respect to the time are computed as

$$\frac{d}{dt}\left(\frac{\partial T}{\partial \dot{a}_i}\right) = (\dot{\mathbf{J}})_i^T\mathbf{I}_T\boldsymbol{\omega} + (\mathbf{J})_i^T\dot{\mathbf{I}}_1\boldsymbol{\omega} + (\mathbf{J})_i^T\frac{\partial\mathbf{I}_2}{\partial\gamma}\boldsymbol{\omega}\dot{\gamma} + (\mathbf{J})_i^T\mathbf{I}_T\dot{\boldsymbol{\omega}} + (\dot{\mathbf{J}})_i^T\mathbf{I}_2\mathbf{e}_2\dot{\gamma} + (\mathbf{J})_i^T\mathbf{I}_2\mathbf{e}_2\ddot{\gamma} \tag{4.34}$$

$$\frac{d}{dt}\left(\frac{\partial T}{\partial \dot{\gamma}}\right) = I_2^{22}\ddot{\gamma} + \mathbf{e}_2^T\mathbf{I}_2\dot{\boldsymbol{\omega}} \tag{4.35}$$

The generalized torque is derived starting from virtual power as

$$\begin{aligned}\delta W &= \boldsymbol{\tau}^T\delta\boldsymbol{\omega} + T_m\delta\dot{\gamma} \\ &= \boldsymbol{\tau}^T\boldsymbol{J}\delta\dot{\mathbf{a}} + T_m\delta\dot{\gamma} \\ &= \begin{bmatrix}\mathbf{J}^T\boldsymbol{\tau} & T_m\end{bmatrix}\begin{bmatrix}\delta\dot{\mathbf{a}} \\ \delta\dot{\gamma}\end{bmatrix}\end{aligned} \tag{4.36}$$

Finally, the total torque is given as

$$\mathbf{Q} = \begin{bmatrix}Q_1 \\ Q_2 \\ Q_3 \\ Q_4\end{bmatrix} = \begin{bmatrix}\mathbf{J}^T\boldsymbol{\tau} \\ T_m\end{bmatrix} \tag{4.37}$$

Lagrange equations are defined as

$$\frac{d}{dt}\left(\frac{\partial T}{\partial \dot{q}_i}\right) - \frac{\partial T}{\partial q_i} = Q_i \tag{4.38}$$

which lead to the final reformulation reported below

$$\begin{aligned}&(\dot{\mathbf{J}})_i^T\mathbf{I}_T\boldsymbol{\omega} + (\mathbf{J})_i^T\dot{\mathbf{I}}_1\boldsymbol{\omega} + (\mathbf{J})_i^T\frac{\partial\mathbf{I}_2}{\partial\gamma}\boldsymbol{\omega}\dot{\gamma} + (\mathbf{J})_i^T\mathbf{I}_T\dot{\boldsymbol{\omega}} + (\dot{\mathbf{J}})_i^T\mathbf{I}_2\mathbf{e}_2\dot{\gamma} \\ &+ (\mathbf{J})_i^T\mathbf{I}_2\mathbf{e}_2\ddot{\gamma} - \dot{\mathbf{a}}^T\mathbf{J}^T\mathbf{I}_T\frac{\partial\mathbf{J}}{\partial a_i}\dot{\mathbf{a}} - \mathbf{e}_2^T\mathbf{I}_2\frac{\partial\mathbf{J}}{\partial a_i}\dot{\mathbf{a}}\dot{\gamma} = [\mathbf{J}^T\boldsymbol{\tau}]_i\end{aligned} \tag{4.39}$$

$$I_2^{22}\ddot{\gamma} + c_\gamma\dot{\gamma} + \mathbf{e}_2^T\mathbf{I}_2\dot{\boldsymbol{\omega}} - \frac{1}{2}\boldsymbol{\omega}^T\frac{\partial\mathbf{I}_2}{\partial\gamma}\boldsymbol{\omega} = T_m \tag{4.40}$$

Defining the state vector as $\mathbf{x} = \begin{bmatrix}\boldsymbol{\omega} & \dot{\gamma}\end{bmatrix}^T$ and the SADA damping as c_γ , the final coupled multibody equation model is given by

$$\mathbf{M}(\mathbf{a})\dot{\mathbf{x}} + \mathbf{C}(\mathbf{a})\mathbf{x} + \mathbf{H} = \mathbf{T} \tag{4.41}$$

where the matrices $\mathbf{M}$, $\mathbf{C}$ and $\mathbf{H}$ are computed starting from equations (4.39)-(4.40) and are defined below

$$\mathbf{M}(\mathbf{a}) = \begin{bmatrix}\mathbf{J}^T\mathbf{I}_T & \mathbf{J}^T\mathbf{I}_2\mathbf{e}_2 \\ \mathbf{e}_2^T\mathbf{I}_2 & I_2^{22}\end{bmatrix} \tag{4.42}$$

$$\mathbf{C}(\mathbf{a}) = \begin{bmatrix}\dot{\mathbf{J}}^T\mathbf{I}_T + (\mathbf{J})_i^T\dot{\mathbf{I}}_1 & \dot{\mathbf{J}}^T\mathbf{I}_2\mathbf{e}_2 \\ \mathbf{0}_{1\times3} & c_\gamma\end{bmatrix} \tag{4.43}$$

$$\mathbf{H} = \begin{bmatrix} -\dot{\mathbf{a}}^T \left(\frac{\partial \mathbf{J}}{\partial \phi}\right)^T (\mathbf{I}_T \boldsymbol{\omega} + \mathbf{I}_2 \mathbf{e}_2 \dot{\gamma}) + (\mathbf{J})_1^T \frac{\partial \mathbf{I}_2}{\partial \gamma} \boldsymbol{\omega} \dot{\gamma} \\ -\dot{\mathbf{a}}^T \left(\frac{\partial \mathbf{J}}{\partial \theta}\right)^T (\mathbf{I}_T \boldsymbol{\omega} + \mathbf{I}_2 \mathbf{e}_2 \dot{\gamma}) + (\mathbf{J})_2^T \frac{\partial \boldsymbol{I}_2}{\partial \gamma} \boldsymbol{\omega} \dot{\gamma} \\ -\dot{\mathbf{a}}^T \left(\frac{\partial \mathbf{J}}{\partial \psi}\right)^T (\mathbf{I}_T \boldsymbol{\omega} + \mathbf{I}_2 \mathbf{e}_2 \dot{\gamma}) + (\mathbf{J})_3^T \frac{\partial \mathbf{I}_2}{\partial \gamma} \boldsymbol{\omega} \dot{\gamma} \\ -\frac{1}{2} \boldsymbol{\omega}^T \frac{\partial \mathbf{I}_2}{\partial \gamma} \boldsymbol{\omega} \end{bmatrix} \tag{4.44}$$

$$\boldsymbol{T} = \begin{bmatrix} \boldsymbol{J}^T \boldsymbol{\tau} \\ T_m \end{bmatrix} \tag{4.45}$$

4.5 Inertia Matrix inversion

The solution of the dynamics equation of the multibody satellite requires the inversion of the matrix $\mathbf{M}(\mathbf{x})$ of Equation 4.41. In order to reduce the computational burden, i.e. avoid the use of standard inversion algorithms, a close form solution for the computation of the inverse is presented here. Let us define the matrix

$$\mathbf{M} = \begin{bmatrix} \mathbf{A} & \mathbf{B} \\ \mathbf{C} & \mathbf{D} \end{bmatrix} \tag{4.46}$$

where the terms are given by

$$\mathbf{A} = \mathbf{J}^T(\mathbf{I}_1 + \mathbf{I}_2) \quad \mathbf{B} = \mathbf{J}^T \mathbf{I}_2 \mathbf{e}_2 \quad \mathbf{C} = \mathbf{e}_2^T \mathbf{I}_2 \quad \mathbf{D} = I_2^{22} \tag{4.47}$$

The matrix inversion formula presented in [37], can be defined as

$$\mathbf{M}^{-1} = \begin{bmatrix} \mathbf{A}^{-1} + \mathbf{A}^{-1}\mathbf{B}\mathbf{H}\mathbf{C}\mathbf{A}^{-1} & -\mathbf{A}^{-1}\mathbf{B}\mathbf{H} \\ -\mathbf{H}\mathbf{C}\mathbf{A}^{-1} & \mathbf{H} \end{bmatrix} \quad \text{where} \quad \mathbf{H} = (\mathbf{D} - \mathbf{C}\mathbf{A}^{-1}\mathbf{B})^{-1} \tag{4.48}$$

The inverse can be computed if and only if $(\mathbf{D} - \mathbf{C}\mathbf{A}^{-1}\mathbf{B})$ is invertible. During the simulation, this matrix has proved to be always invertible, anyhow in case the matrix $(\mathbf{D} - \mathbf{C}\mathbf{A}^{-1}\mathbf{B})$ results to be non-invertible an alternative inversion algorithm is called as recovery mode. Notice that $\mathbf{D}$ is a scalar, so the only matrix which needs the computation of the inverse is $\mathbf{A}$, i.e.

$$\mathbf{A}^{-1} = (\mathbf{J}^T(\mathbf{I}_1 + \mathbf{I}_2))^{-1} = (\mathbf{I}_1 + \mathbf{I}_2)^{-1}(\mathbf{J}^T)^{-1} \tag{4.49}$$

The objective is to find a closed analytic form of equation 4.49. The inverse of the transpose Jacobian matrix is given by

$$(\mathbf{J}^T)^{-1} = \frac{1}{s_\theta} \begin{bmatrix} s_\psi & c_\psi s_\theta & -c_\theta s_\psi \\ c_\psi & -s_\psi s_\theta & -c_\theta c_\psi \\ 0 & & s_\theta \end{bmatrix} \tag{4.50}$$

The sum of the inertia matrices $\mathbf{I}_1$ and $\mathbf{I}_2$ is $\mathbf{I}_T$. Given the structure of $\mathbf{I}_1$ and $\mathbf{I}_2$, respectively defined in 4.2 and 4.7, matrix $\mathbf{I}_T$ can be written as

$$\mathbf{I}_T = \mathbf{M} = \begin{bmatrix} M_{11} & 0 & M_{13} \\ 0 & M_{22} & 0 \\ M_{13} & 0 & M_{33} \end{bmatrix} \tag{4.51}$$

The inversion of matrix M can be computed exploiting the Shermann-Morrison formula reported in [38]

$$(\mathbf{E} + \mathbf{u}\mathbf{v}^T)^{-1} = \mathbf{E}^{-1} + \frac{\mathbf{E}^{-1}\mathbf{u}\mathbf{v}^T\mathbf{A}^{-1}}{1 + \mathbf{v}^T\mathbf{A}^{-1}\mathbf{u}} \tag{4.52}$$

The objective is to define a diagonal matrix $\mathbf{E}$ and a matrix $\mathbf{u}\mathbf{v}^T$ such that $\mathbf{J} = (\mathbf{E}+\mathbf{u}\mathbf{v}^T)$. The advantage is that the inversion of matrix $\mathbf{E}$ needs only three divisions and then the computation of the matrix $\mathbf{J}$ just needs few simple operations. A possible set up is the following

$$\mathbf{E} = \begin{bmatrix} M_{11} - M_{13} & 0 & 0 \\ 0 & M_{22} & 0 \\ 0 & 0 & M_{33} - M_{13} \end{bmatrix} \tag{4.53}$$

$$\mathbf{E}^{-1} = \begin{bmatrix} \frac{1}{M_{11}-M_{13}} & 0 & 0 \\ 0 & \frac{1}{M_{22}} & 0 \\ 0 & 0 & \frac{1}{M_{33}-M_{13}} \end{bmatrix} \tag{4.54}$$

$$\mathbf{u} = \text{sign}(M_{13}) \begin{bmatrix} \sqrt{|M_{13}|} \\ 0 \\ \sqrt{|M_{13}|} \end{bmatrix} \tag{4.55}$$

$$\mathbf{v} = \begin{bmatrix} \sqrt{|M_{13}|} \\ 0 \\ \sqrt{|M_{13}|} \end{bmatrix} \tag{4.56}$$

The simplified expression for the computation of the inverse of the generic inertia matrix M is given by

$$\mathbf{I}^{-1} = \begin{bmatrix} \gamma_1 & 0 & 0 \\ 0 & \gamma_2 & 0 \\ 0 & 0 & \gamma_3 \end{bmatrix} + \frac{1}{M_{13}(\gamma_1\gamma_3)} \begin{bmatrix} \gamma_1^2 M_{13} & 0 & \gamma_1\gamma_3 M_{13} \\ 0 & 0 & 0 \\ \gamma_1\gamma_3 M_{13} & 0 & \gamma_3^2 M_{13} \end{bmatrix} \tag{4.57}$$

where the terms γ_i are defined as

$$\gamma_1 = \frac{1}{M_{11} - M_{13}} \quad \gamma_2 = \frac{1}{M_{22}} \quad \gamma_3 = \frac{1}{M_{33} - M_{13}} \tag{4.58}$$

The application of this technique instead of the standard inversion make the computations 50 times faster [1], providing the exact inversion.

[1] Comparison of the time needed to perform 10000 inversions using the aforementioned method and the standard MATLAB command

4.6 Attitude trajectory

The attitude trajectory generation is a key process to make the mission successful. All the pointing requirements, e.g. the payload pointing, are translated into a sequence of poses that the satellite shall assume driven by the attitude controller. The sequence of poses is the attitude trajectory. The goal of the Eutelsat 172B is to maintain the payload pointed towards the Earth, while maximizing the energy produced with the solar arrays. The satellite orbit around the Earth is defined in the Eutelsat 172B specifications [11] and the sun position in the ECI reference frame can be obtained by using the model presented in subsection 3.2.1. The orbit of the Earth around the Sun and the satellite orbit around the Earth are depicted in Figure 4.2.

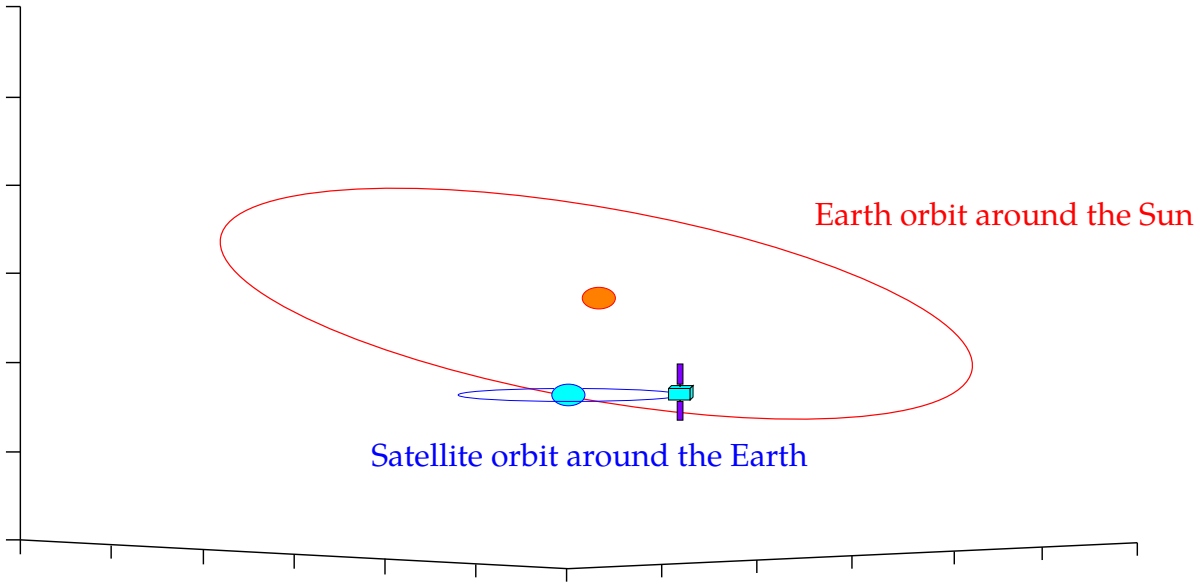

Figure 4.2: Sun and Satellite orbits in ECI (Earth and satellite dimensions are magnified)

The easiest way to define an attitude trajectory to fulfill the tasks is to exploit the LVLH reference frame. The Earth pointing payload requirement can be fulfilled by imposing that the payload points toward the LVLH z-axis direction. By imposing the Earth pointing constraints, 2 Degrees of Freedom (DoF) are now blocked. The remaining DoF are the rotation of the satellite around the LVLH z-axis and the rotation of the solar arrays around the body reference frame y-axis. The orbit periods of the Earth around the Sun and the Satellite around the Earth are different and, in first approximation, can be considered respectively equal to one year and one day. The trajectory planning is conceived considering the Sun fixed and the satellite orbiting around the Earth, considering a one day time horizon. By using this idea, the natural choice is to point the solar array rotational axis along the satellite orbit normal vector to make the solar arrays be impacted by the sunlight at almost 90 ^{o}. This idea can be visualized in Figure 4.3. Figure 4.4 visually summarizes the geometry of the Earth and Satellite orbital trajectories, the ECI and the LVLH reference systems and the satellite orientation.

The reference attitude matrix is then computed as

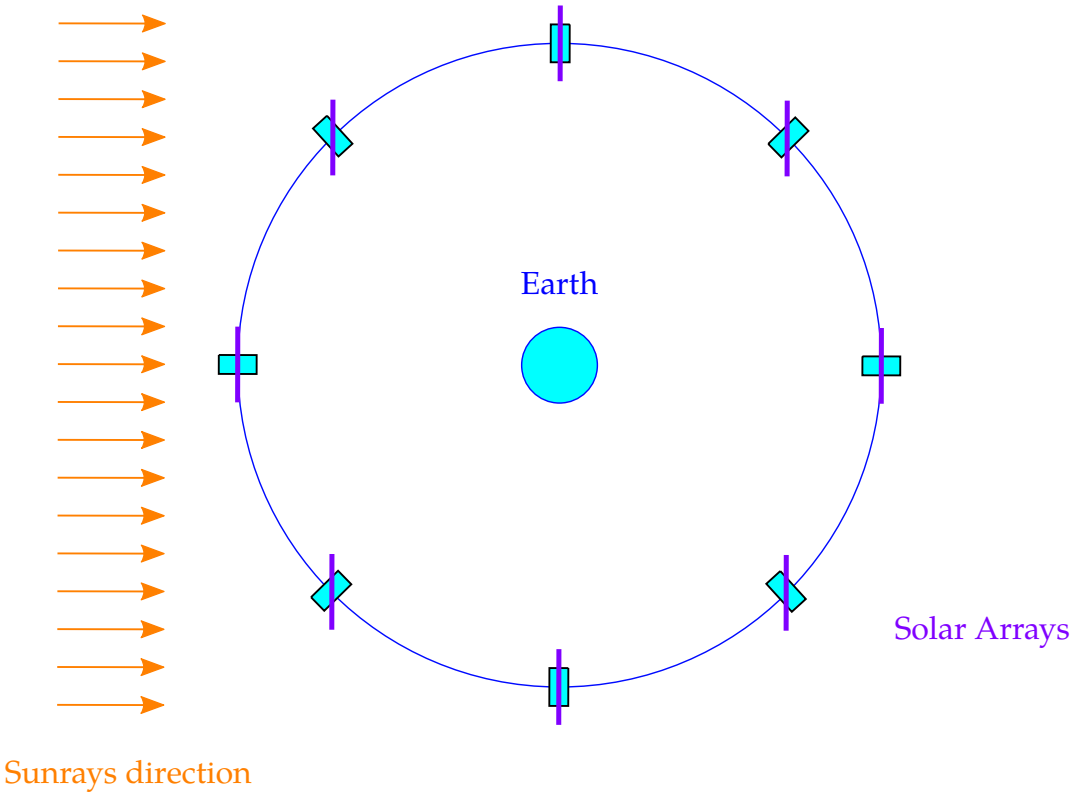

Figure 4.3: Earth and Satellite orbits (satellite orbit normal view)

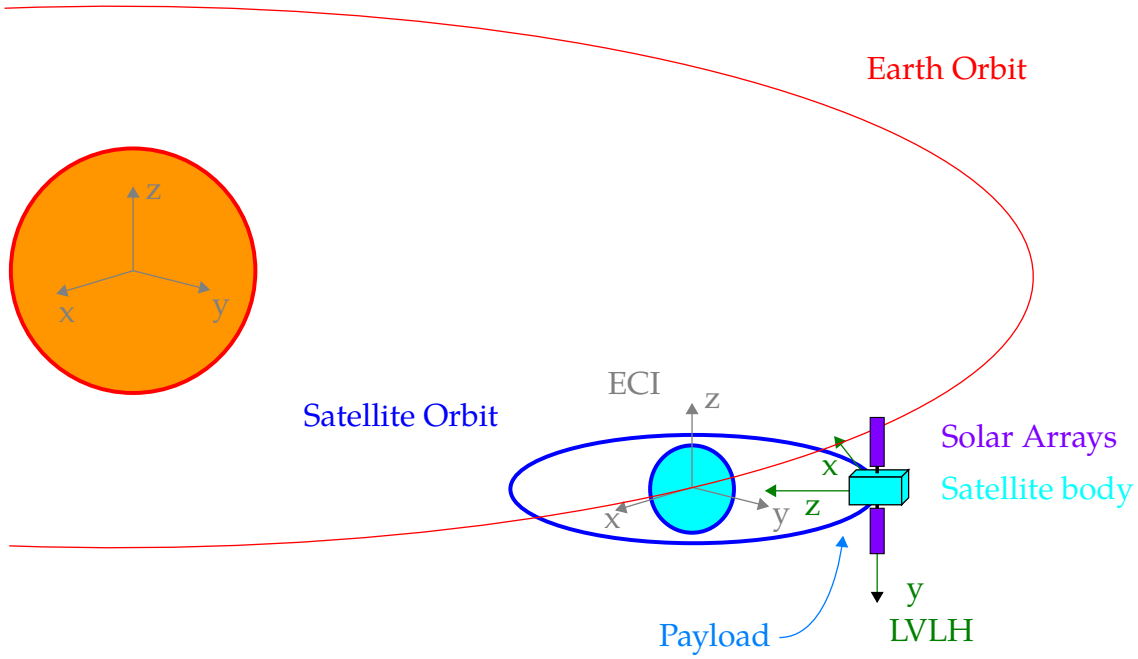

Figure 4.4: Earth and Satellite orbits

$$\mathbf{T}_{ref} = \mathbf{T}_{LI}\mathbf{T}_{RL} \quad \mathbf{T}_{RL} = \begin{bmatrix} 0 & 0 & 1 \\ 0 & 1 & 0 \\ -1 & 0 & 0 \end{bmatrix} \tag{4.59}$$

where $\mathbf{T}_{RL}$ is the transformation matrix that position the satellite as described in the last paragraph, i.e. the payload that points along the LVLH z-axis and the SA rotation axis is parallel to the LVLH y-axis. The controller requires a Euler 313 reference signal, thus a conversion from attitude matrix $\mathbf{T}_{ref}$ to Euler 313 shall be implemented. We consider the satellite position and velocity at time t as $\mathbf{r}_{ECI} = [\, r\cos(\omega_\oplus t)\, r\sin(\omega_\oplus t)\, 0\,]^T$ and $\mathbf{v}_{ECI} = [\, -r\sin(\omega_\oplus t)\, r\cos(\omega_\oplus t)\, 0\,]^T$. Hence, the evolution in time of the matrix $\mathbf{T}_{LI}$, given the definitions in subsection 3.1.4, is

$$\mathbf{T}_{LI} = \begin{bmatrix} -\sin(\omega_\oplus t) & 0 & -\cos(\omega_\oplus t) \\ \cos(\omega_\oplus t) & 0 & -\sin(\omega_\oplus t) \\ 0 & -1 & 0 \end{bmatrix} \tag{4.60}$$

where r is the magnitude of the orbit radius and $\omega_\oplus$ is the Earth angular velocity magnitude in ECI. The matrix $\mathbf{T}_{ref}$ can be computed using Equation (4.59). Finally, by using the conversion equations described in Equations (4.18), the attitude trajectory in Euler 313 given by

$$\bar{\mathbf{x}}_r = \begin{bmatrix} \phi \\ \theta \\ \psi \end{bmatrix} = \begin{bmatrix} \omega_\oplus t - \pi \\ \pi/2 \\ \pi \end{bmatrix} \tag{4.61}$$

Given the above definition of Euler 313 trajectory, by taking its derivative with respect to time considering the kinematic equation 4.22, we obtain reference trajectory for the angular velocity, which is constant in time and is given by

$$\boldsymbol{\omega}_r = \begin{bmatrix} 0 \\ -\omega_\oplus \\ 0 \end{bmatrix} \tag{4.62}$$

4.7 Linearized Attitude Dynamics equations

Attitude control methods based on linear controllers, such as MPC, need a linear model of the plant to be designed. Attitude dynamics and kinematics equations linearization for attitude control is a standard practice when the satellite states stay in a neighborhood of the linearization point [29]. The attitude dynamics equation for a rigid body is given by equation (4.24) and the kinematic equation is given by equation (4.22). Here we suppose that the inertia matrix of the spacecraft is constant and diagonal. The offdiagonal terms are neglected because are smaller with respect to the diagonal elements. Hence, the inertia matrix used for the linearized model is

$$\tilde{\mathbf{I}} = \begin{bmatrix} \mathbf{I}_T(1,1) & 0 & 0 \\ 0 & \mathbf{I}_T(2,2) & 0 \\ 0 & 0 & \mathbf{I}_T(3,3) \end{bmatrix} \tag{4.63}$$

where the entries of the $\tilde{\mathbf{I}}$ matrix are the diagonal terms of the matrix $\mathbf{I}_T$, defined in section 4.1, considering angle $\gamma = 0$. The linearized model is derived in this section and includes both dynamics and kinematics.
The linearization procedure around the linearization point is described in [39] and hereafter is briefly recalled. The dynamic differential equation is in the form $\dot{\mathbf{x}} = \mathbf{f}(\mathbf{x}, \mathbf{u})$ where $\mathbf{x}$ is the state vector and $\mathbf{u}$ is the input vector. The Taylor expansion at state $\bar{\mathbf{x}}$ and input $\bar{\mathbf{u}}$ stopped at first order is

$$\begin{aligned} \mathbf{f}(\mathbf{x}, \mathbf{u}) &\approx \mathbf{f}(\bar{\mathbf{x}}, \bar{\mathbf{u}}) + \left.\frac{\partial \mathbf{f}}{\partial \mathbf{x}}\right|_{\bar{\mathbf{x}}, \bar{\mathbf{u}}} (\mathbf{x} - \bar{\mathbf{x}}) + \left.\frac{\partial \mathbf{f}}{\partial \mathbf{u}}\right|_{\bar{\mathbf{x}}, \bar{\mathbf{u}}} (\mathbf{u} - \bar{\mathbf{u}}) \\ &\approx \dot{\bar{\mathbf{x}}} + \mathbf{A}\tilde{\mathbf{x}} + \mathbf{B}\tilde{\mathbf{u}} \end{aligned} \tag{4.64}$$

where the tilde quantities are $\tilde{\mathbf{x}} = \mathbf{x} - \bar{\mathbf{x}}$ and $\tilde{\mathbf{u}} = \mathbf{u} - \bar{\mathbf{u}}$. Subtracting $\dot{\bar{\mathbf{x}}}$ from both sides of the equation 4.64 returns

$$\dot{\tilde{\mathbf{x}}} = \mathbf{A}\tilde{\mathbf{x}} + \mathbf{B}\tilde{\mathbf{u}} \tag{4.65}$$

The equation is linear in terms of $\tilde{\mathbf{x}}$ and $\tilde{\mathbf{u}}$. The equation (4.65) is a linear equation for the deviations of the state and the control from their nominal values. The integration procedure for the linearized model is summarized in Figure 4.5.

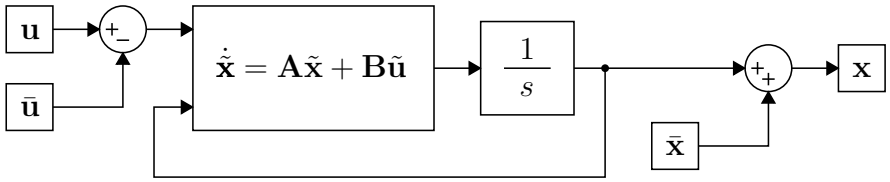

Figure 4.5: Integration of linearized model

The reference frame for the attitude equation is ECI, thus there is no single linearization point. The attitude equation is linearized along the trajectory, possibly resulting in different matrix $\mathbf{A}$ and $\mathbf{B}$. The reference trajectory is defined in subsection 4.6. The linearization point is

$$\bar{\mathbf{x}} = \begin{bmatrix} \phi \\ \theta \\ \psi \\ \omega_1 \\ \omega_2 \\ \omega_3 \end{bmatrix} = \begin{bmatrix} \omega_\oplus t - \pi \\ \pi/2 \\ \pi \\ 0 \\ -\omega_\oplus \\ 0 \end{bmatrix} \tag{4.66}$$

and the input linearization point is set to

$$\bar{\mathbf{u}} = \begin{bmatrix} \tau_x \\ \tau_y \\ \tau_z \end{bmatrix} = \begin{bmatrix} 0 \\ 0 \\ 0 \end{bmatrix} \tag{4.67}$$

The equation 4.24 is the general form when the inertia matrix is non-diagonal. In the case when the inertia matrix is diagonal, equation 4.24 reduces to

$$\dot{\omega}_1 = \omega_2\omega_3\frac{\tilde{I}_{33} - \tilde{I}_{22}}{\tilde{I}_1 1} + \frac{\tau_1}{\tilde{I}_{11}} \tag{4.68}$$

$$\dot{\omega}_2 = \omega_1\omega_3\frac{\tilde{I}_{11} - \tilde{I}_{33}}{\tilde{I}_2 2} + \frac{\tau_2}{\tilde{I}_{22}} \tag{4.69}$$

$$\dot{\omega}_3 = \omega_1\omega_2\frac{\tilde{I}_{22} - \tilde{I}_{11}}{\tilde{I}_3 3} + \frac{\tau_3}{\tilde{I}_{33}} \tag{4.70}$$

The system of equations for attitude dynamics and kinematics for the Euler angles 313 is given by

$$\mathbf{f}(\mathbf{x},\mathbf{u}) = \begin{cases} \dot{\phi} = \frac{s_\psi}{s_\theta}\omega_1 + \frac{c_\psi}{s_\theta}\omega_2 \\ \dot{\theta} = c_\psi\omega_1 - s_\psi\omega_2 \\ \dot{\psi} = \frac{c_\theta s_\psi}{s_\theta}\omega_1 - \frac{c_\theta c_\psi}{s_\theta}\omega_2 + \omega_3 \\ \dot{\omega}_1 = \omega_2\omega_3\frac{\tilde{I}_{33}-\tilde{I}_{22}}{\tilde{I}_1 1} + \frac{\tau_1}{\tilde{I}_{11}} \\ \dot{\omega}_2 = \omega_1\omega_3\frac{\tilde{I}_{11}-\tilde{I}_{33}}{\tilde{I}_2 2} + \frac{\tau_2}{\tilde{I}_{22}} \\ \dot{\omega}_3 = \omega_1\omega_2\frac{\tilde{I}_{22}-\tilde{I}_{11}}{\tilde{I}_3 3} + \frac{\tau_3}{\tilde{I}_{33}} \end{cases} \tag{4.71}$$

The state matrix $\mathbf{A}$ of the linearized attitude equation is given by

$$\mathbf{A} = \left.\frac{\partial \mathbf{f}}{\partial \mathbf{x}}\right|_{\bar{\mathbf{x}},\bar{\mathbf{u}}} = \begin{bmatrix} 0 & 0 & 0 & 0 & -1 & 0 \\ 0 & 0 & -\omega_\oplus & -1 & 0 & 0 \\ 0 & \omega_\oplus & 0 & 0 & 0 & 1 \\ 0 & 0 & 0 & 0 & 0 & \omega_\oplus\frac{\tilde{I}_{22}-\tilde{I}_{33}}{\tilde{I}_{11}} \\ 0 & 0 & 0 & 0 & 0 & 0 \\ 0 & 0 & 0 & \omega_\oplus\frac{\tilde{I}_{11}-\tilde{I}_{22}}{\tilde{I}_{33}} & 0 & 0 \end{bmatrix} \tag{4.72}$$

The input matrix $\mathbf{B}$ of the linearized attitude equation is given by

$$\mathbf{B} = \left.\frac{\partial \mathbf{f}}{\partial \mathbf{u}}\right|_{\bar{\mathbf{x}},\bar{\mathbf{u}}} = \begin{bmatrix} 0 & 0 & 0 \\ 0 & 0 & 0 \\ 0 & 0 & 0 \\ \frac{1}{\tilde{I}_{11}} & 0 & 0 \\ 0 & \frac{1}{\tilde{I}_{22}} & 0 \\ 0 & 0 & \frac{1}{\tilde{I}_{33}} \end{bmatrix} \tag{4.73}$$

Notice that the the first component of the linearization point in 4.66 is time varying, but the time variable does not enters in matrix $\mathbf{A}$. Both matrices $\mathbf{A}$ and $\mathbf{B}$ are composed by constant terms, thus the attitude dynamics deviation equation is given by

$$\begin{bmatrix} \dot{\tilde{\phi}} \\ \dot{\tilde{\theta}} \\ \dot{\tilde{\psi}} \\ \dot{\tilde{\omega}}_1 \\ \dot{\tilde{\omega}}_2 \\ \dot{\tilde{\omega}}_3 \end{bmatrix} = \begin{bmatrix} 0 & 0 & 0 & 0 & -1 & 0 \\ 0 & 0 & -\omega_\oplus & -1 & 0 & 0 \\ 0 & \omega_\oplus & 0 & 0 & 0 & 1 \\ 0 & 0 & 0 & 0 & 0 & \omega_\oplus \frac{\tilde{I}_{22}-\tilde{I}_{33}}{\tilde{I}_{11}} \\ 0 & 0 & 0 & 0 & 0 & 0 \\ 0 & 0 & 0 & \omega_\oplus \frac{\tilde{I}_{11}-\tilde{I}_{22}}{\tilde{I}_{33}} & 0 & 0 \end{bmatrix} \begin{bmatrix} \tilde{\phi} \\ \tilde{\theta} \\ \tilde{\psi} \\ \tilde{\omega}_1 \\ \tilde{\omega}_2 \\ \tilde{\omega}_3 \end{bmatrix} + \begin{bmatrix} 0 & 0 & 0 \\ 0 & 0 & 0 \\ 0 & 0 & 0 \\ \frac{1}{\tilde{I}_{11}} & 0 & 0 \\ 0 & \frac{1}{\tilde{I}_{22}} & 0 \\ 0 & 0 & \frac{1}{\tilde{I}_{33}} \end{bmatrix} \begin{bmatrix} \tau_1 \\ \tau_2 \\ \tau_3 \end{bmatrix} \tag{4.74}$$

4.8 Attitude disturbance analysis

The disturbance analysis is based on a simulation of the disturbance torques acting on the satellite during one year. In Figure 4.6, the disturbances evolution over a year is represented and the related minimum and maximum bounds, which are reported in table 4.1, have been used to defined the convex disturbance set Ξ.

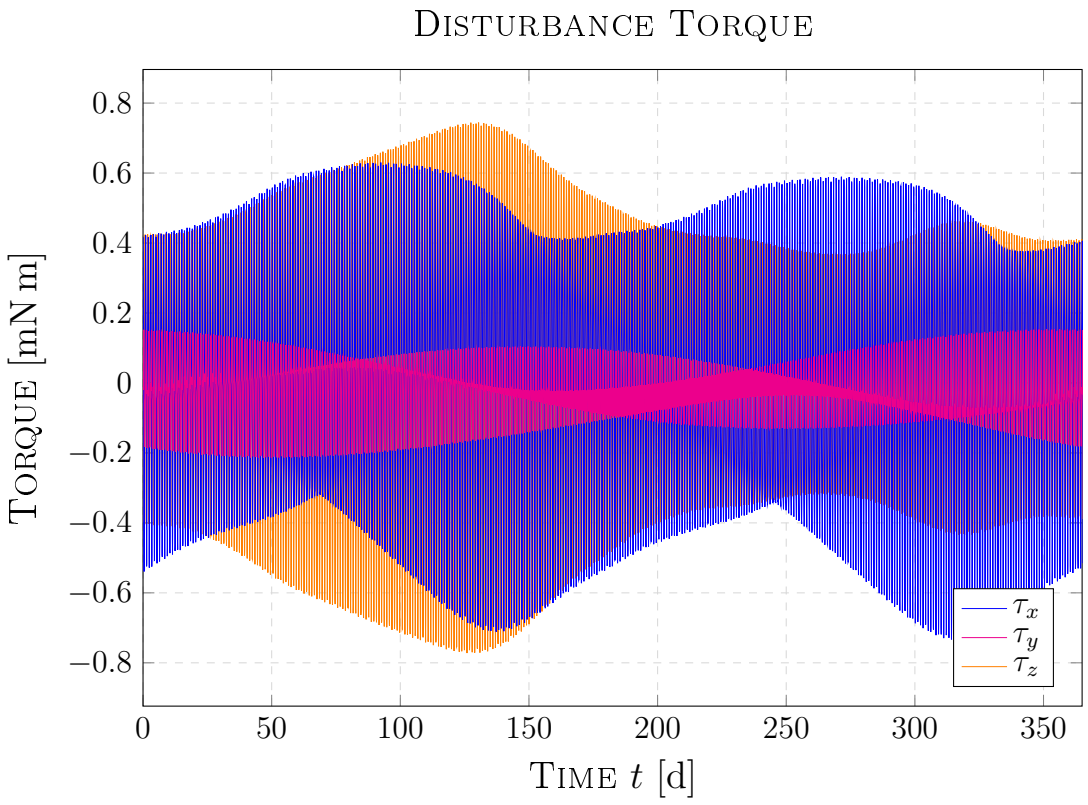

Figure 4.6: Torque disturbance acting on the satellite

The convex disturbance set is a polytope defined as follows

lower bound $[\mathrm{mN\,m}]$	upper bound $[\mathrm{mN\,m}]$
-0.8	0.8
-0.5	0.5
-0.8	0.8

Table 4.1: Torque disturbances bounds

$$\Xi = \left\{ \mathbf{w} \in \mathbb{R}^3 : \mathbf{V}_\Xi \mathbf{w} \leq \mathbf{1} \right\} \tag{4.75}$$

where the matrix $\mathbf{V}_\Xi$ is defined as

$$\mathbf{V} = \begin{bmatrix} -1250 & 0 & 0 \\ 0 & -2000 & 0 \\ 0 & 0 & -1250 \\ 1250 & 0 & 0 \\ 0 & 2000 & 0 \\ 0 & 0 & 1250 \end{bmatrix} \tag{4.76}$$

This convex disturbance set will be used as the additive disturbance set for the design of the TRMPC controller in section 5.5.2. The set is plotted in Figure 4.7

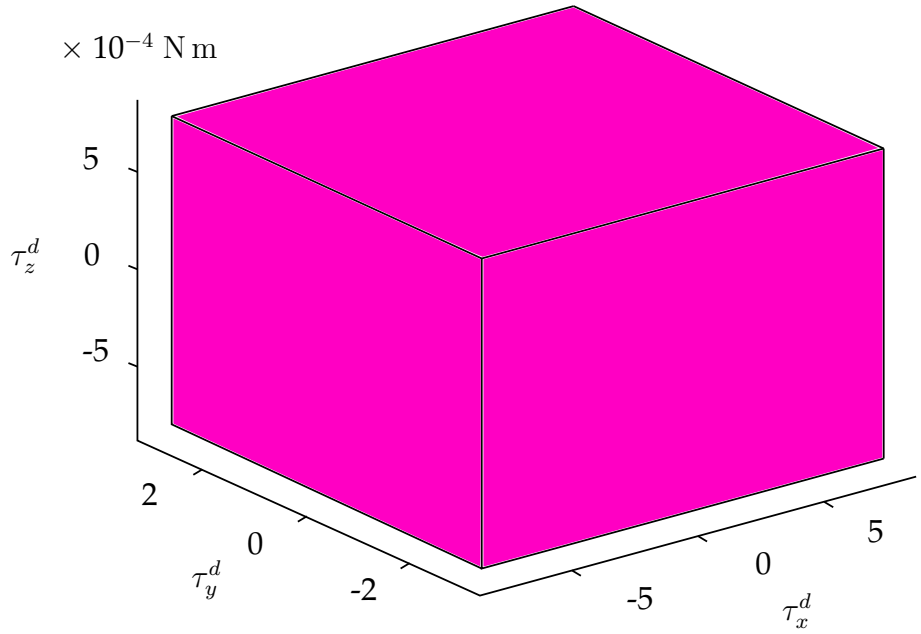

Figure 4.7: Torque disturbance set

4.9 Attitude actuators

The actuator position and orientation design has been assumed following the guidelines of [29]. The actuators are positioned in the most distant points of the main body with respect with the CoM to maximize the produced torque and their orientation has been chosen to avoid ion jet collision with payload components and SA. The thrusters are arranged in clusters. Each of the $n_p = 8$ cluster is represented in Figure 4.8, where the origin of the arrow indicates the position $\mathbf{r}_i$ of the i-th cluster and the direction $\mathbf{u}_i$ of the arrow indicates the cluster thrusters orientation. Each cluster features $n_t = 4$ Enpulsion NANO R^3 thrusters.

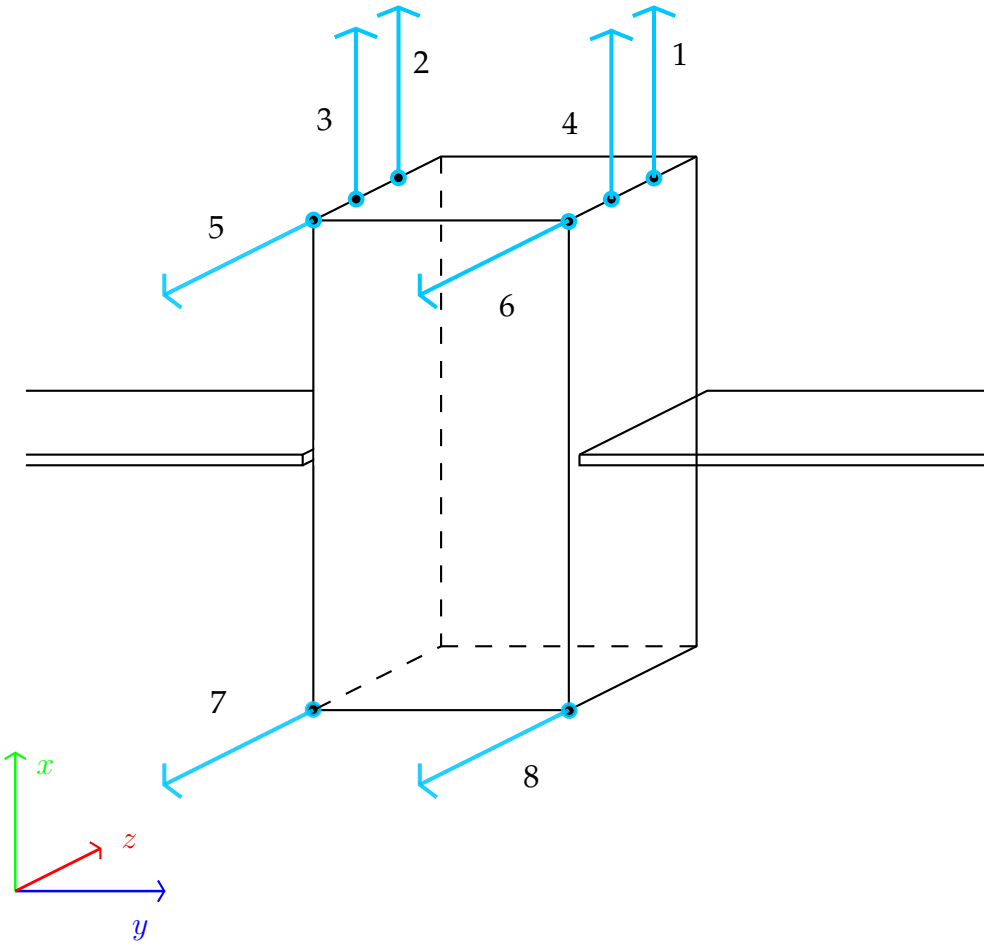

Figure 4.8: Satellite thrusters scheme

The cluster position are located at

$$\mathbf{r}_1 = \begin{bmatrix} 2.85 \\ 1.5 \\ 0.8 \end{bmatrix} \qquad \mathbf{r}_2 = \begin{bmatrix} 2.85 \\ -1.5 \\ 0.8 \end{bmatrix} \qquad \mathbf{r}_3 = \begin{bmatrix} 2.85 \\ -1.5 \\ -0.8 \end{bmatrix} \qquad \mathbf{r}_3 = \begin{bmatrix} 2.85 \\ 1.5 \\ -0.8 \end{bmatrix} \tag{4.77}$$

$$\mathbf{r}_5 = \begin{bmatrix} 2.85 \\ -1.5 \\ -1.85 \end{bmatrix} \qquad \mathbf{r}_6 = \begin{bmatrix} 2.85 \\ 1.5 \\ -1.85 \end{bmatrix} \qquad \mathbf{r}_7 = \begin{bmatrix} -2.85 \\ -1.5 \\ -1.85 \end{bmatrix} \qquad \mathbf{r}_8 = \begin{bmatrix} -2.85 \\ 1.5 \\ -1.85 \end{bmatrix} \tag{4.78}$$

The direction of the gas output with respect to the main body reference frame are

$$\mathbf{u}_1 = \begin{bmatrix} 1 \\ 0 \\ 0 \end{bmatrix} \quad \mathbf{u}_2 = \begin{bmatrix} 1 \\ 0 \\ 0 \end{bmatrix} \quad \mathbf{u}_3 = \begin{bmatrix} 1 \\ 0 \\ 0 \end{bmatrix} \quad \mathbf{u}_4 = \begin{bmatrix} 1 \\ 0 \\ 0 \end{bmatrix} \tag{4.79}$$

$$\mathbf{u}_5 = \begin{bmatrix} 0 \\ 0 \\ -1 \end{bmatrix} \quad \mathbf{u}_6 = \begin{bmatrix} 0 \\ 0 \\ -1 \end{bmatrix} \quad \mathbf{u}_7 = \begin{bmatrix} 0 \\ 0 \\ -1 \end{bmatrix} \quad \mathbf{u}_8 = \begin{bmatrix} 0 \\ 0 \\ -1 \end{bmatrix} \tag{4.80}$$

Each thruster is modeled using the classical rocket equation [27]

$$F_i(\dot{m}_i) = \dot{m}_i I_{sp} g_0 \tag{4.81}$$

where F_i and m_i are respectively the produced thrust and the mass flow of thruster i, I_{sp} is the specific impulse of the thrusters and g_0 is the acceleration by gravity. The total torque produced by the thrusters is given by

$$\begin{aligned} \mathbf{T} =& \sum_i \mathbf{r}_i \times F_i \mathbf{u}_i = \sum_i F_i \mathbf{S}(\mathbf{r}_i)\mathbf{u}_i \\ =& I_{sp} g_0 \underbrace{\begin{bmatrix} \mathbf{S}(\mathbf{r}_1)\mathbf{u}_1 & \dots & \mathbf{S}(\mathbf{r}_n)\mathbf{u}_n \end{bmatrix}}_{\mathbf{C}} \mathbf{m} \\ =& \underbrace{I_{sp} g_0 \mathbf{C}}_{\mathbf{D}} \mathbf{m} = \mathbf{D}\mathbf{m} \end{aligned} \tag{4.82}$$

where $\mathbf{r}_i$ is the distance of thruster i from the CoM, $\mathbf{S}(\cdot)$ is the cross product operator and $\mathbf{m} = [\, m_1 \ \dots \ m_n \,]^T$ is the vector of the thrusters mass-flow. The mass-flow of each thruster must be grater than zero and lower than the maximum value of thrust allowed (i.e. 350 mN) [30]. The input force set $\mathbb{F}$ is the set of allowed thrust produced by each thruster and it is defined as

$$0 \leq m_i \leq \frac{n_t F_i}{I_{sp} g_0}, \quad i = 1, \dots, n_p \tag{4.83}$$

The input torque set $\mathbb{G}$ is computed performing an affine transformation of the set $\mathbb{F}$ by the matrix $\mathbf{D}$, i.e.

$$\mathbb{G} = \left\{ \mathbf{u} \in \mathbb{R}^3 : \mathbf{V}_G \mathbf{u} \leq \mathbf{1} \right\} \tag{4.84}$$

where the matrix $\mathbf{V}_G$ is

$$G = \begin{bmatrix} -185.9100 & 97.8474 & -52.1853 \\ 185.9100 & 97.8474 & -52.1853 \\ 0 & 0 & -238.0952 \\ -238.0952 & 0 & 0 \\ -185.9100 & -97.8474 & -52.1853 \\ -185.9100 & 97.8474 & 52.1853 \\ 185.9100 & 97.8474 & 52.1853 \\ 238.0952 & 0 & 0 \end{bmatrix} \tag{4.85}$$

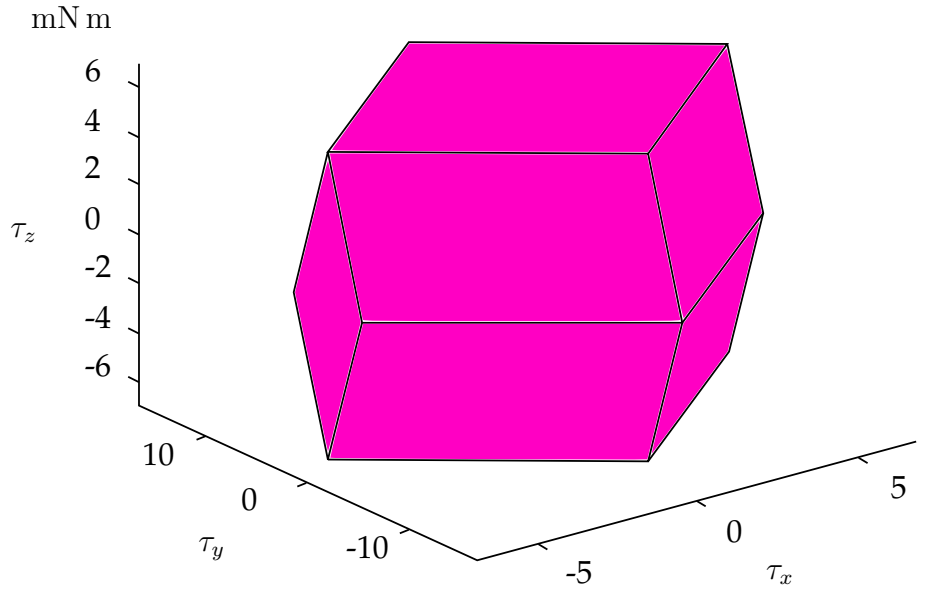

Figure 4.9: Input constraints set

In Figure 4.9 the input torque constraint set is depicted. The controllers that will be presented in Chapter 5 produce a control input torque value. On the other end, our AOCS is thruster based. Hence, we need to derive the real actuator signal to be set to the thrusters according to the control torque defined by the controller. Thus, we have to select which cluster shall be activated to produce the desired torque and a proper problem shall be set up. The problem variables are the n_p values of thrust produced by each cluster of thrusters. The problem constraints are the maximum mass-flow that each cluster can eject, i.e. $\mathbf{m} \in \mathbb{F}$, and the Equation (4.82) which relates the torque and the thrust produced by the thrusters. The number of variables in this problem is higher than the number of constraints, thus there is an infinite number of solution. These kind of problems, where the constraints are linear and the number of solutions are not finite, can be cast into Linear Programming (LP)[2] [41]. Having defined the constraints of the problem, the last element to be designed is the LP cost function. One objective of the satellite mission is to consume the minimum amount of fuel, thus the cost function is designed as the sum of the mass-flows of the clusters. The resulting LP problem is

[2]The solver employed to solve P.1 is OSQP [40].

$$\begin{aligned} \mathbf{m}^* = \quad & \arg\min_{m} && \mathbf{1}^T\mathbf{m} \\ & \text{subject to} && \mathbf{m} \in \mathbb{F} \\ & && \mathbf{Dm} = \mathbf{T} \end{aligned} \tag{P.1}$$

where $\mathbf{m}^*$ is the optimal mass flow of the clusters, the variable $\mathbf{D}$ is the matrix defined in Equation 4.82, $\mathbb{F}$ is the set defined in Equation (4.83) and $\mathbf{T}$ is the control torque input given by the controller. The total fuel consumption M at time t can be computed as in [14].

$$M(t) = M_0 - \int_0^t \|\mathbf{m}\|_1 \, dt \tag{4.86}$$

where M_0 is the initial fuel loaded for the mission.

Chapter 5

Satellite control

This chapter is devoted to the control systems. In the first part the generalities of the SMC and the TRMPC controller are introduced and their application in attitude control is subsequently described. In the last part the SADA optimal trajectory generation and its relative LQR controller are described.

5.1 Sliding Mode Controller

Sliding mode control (SMC) is a well-established control technique for non-linear systems, characterized for his inheritance robustness properties in the presence of plant uncertainties.
The SMC approach can be summarized as described in [36]

- A sliding surface s, which is a subset of the state space, is defined.
- The sliding surface s encloses the trajectory in which the plant is desired to lie.
- A feedback law is designed to bring the plant trajectory towards the sliding surface, and once there, to stay close to s.

The surface s splits the state space in two subspaces: one where $s > 0$ and the other where $s < 0$. When the state trajectory is in one of the two subspaces the control tries to drive the system to the other subspace. When the control law brings the system towards the the subspace, the process restarts. Figure 5.1 shows the SMC working principle.
The SMC action can be divided into two phases: the reaching and the sliding phase. The two phase are sketched in figure 5.2. The first phase that takes place is the reaching one; the initial state is forced towards the desired trajectory on the sliding surface. During the second phase, the sliding one, the trajectory starts in a neighborhood of the sliding surface and it "slides around" the sliding surface. During the sliding phase, the chattering, that is a typical SMC unwanted oscillating phenomenon, can occur.
The reaching phase behavior makes the SMC attractive and the sliding phase behavior makes the SMC invariant.

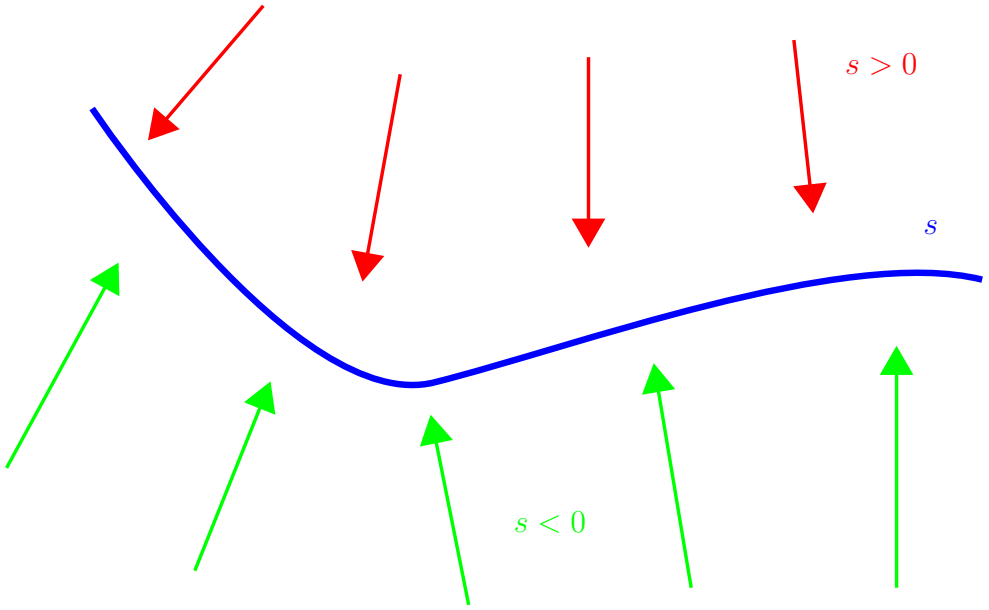

Figure 5.1: SMC principle

5.2 Attitude Sliding Mode Controller

The SMC presented in this section is a classical approach in nonlinear attitude control thanks to its simplicity and performances [36]. The controller shall perform the tracking of the reference attitude, which is described in Section 4.6, in order to accomplish the goal of the mission. The reference attitude trajectory for the SMC controller is expressed by the quaternion reference $\mathfrak{q}_r$ and the angular velocity reference $\boldsymbol{\omega}_r$. While the angular velocity reference is already defined in 4.62, the quaternion reference is computed from the Euler reference trajectory, defined in Equation 4.61, using the conversion equations described in section 4.2.
The system to control is defined by the kinematic equation defined in Equation 4.23 and the Euler dynamics Equation (4.24)

$$\begin{cases} \dot{\mathfrak{q}} = \frac{1}{2}\mathbf{Q}\boldsymbol{\omega} \\ \dot{\boldsymbol{\omega}} = -\mathbf{J}^{-1}\boldsymbol{\omega} \times \mathbf{J}\boldsymbol{\omega} + \mathbf{J}^{-1}\mathbf{u} \end{cases} \tag{5.1}$$

where $\mathbf{J}$ is the inertia tensor of the satellite equal to the inertia matrix $\tilde{\mathbf{I}}$ defined in Equation (4.63) and $\mathbf{Q}$ is the kinematics matrix of quaternion defined in 4.23. The quaternion $\mathbf{q}$, which is defined in 4.16, is the output to be controlled, the system is Multiple Input Multiple Output (MIMO), it is a generalized normal form and it has relative degree $\sigma = 2$. The sliding surface function is defined as

$$\mathbf{s}(\mathbf{q}, \boldsymbol{\omega}, t) = \tilde{\boldsymbol{\omega}} + k_2 \tilde{\mathbf{q}} \tag{5.2}$$

where $\tilde{\boldsymbol{\omega}} = \boldsymbol{\omega} - \boldsymbol{\omega}_r$ and $\tilde{\mathbf{q}}$ are the last three elements of vector $\tilde{\mathfrak{q}}$ defined as

$$\tilde{\mathfrak{q}} = \begin{bmatrix} \tilde{q}_0 \\ \tilde{\mathbf{q}} \end{bmatrix} = \mathfrak{q}^* \otimes \mathfrak{q}_r \tag{5.3}$$

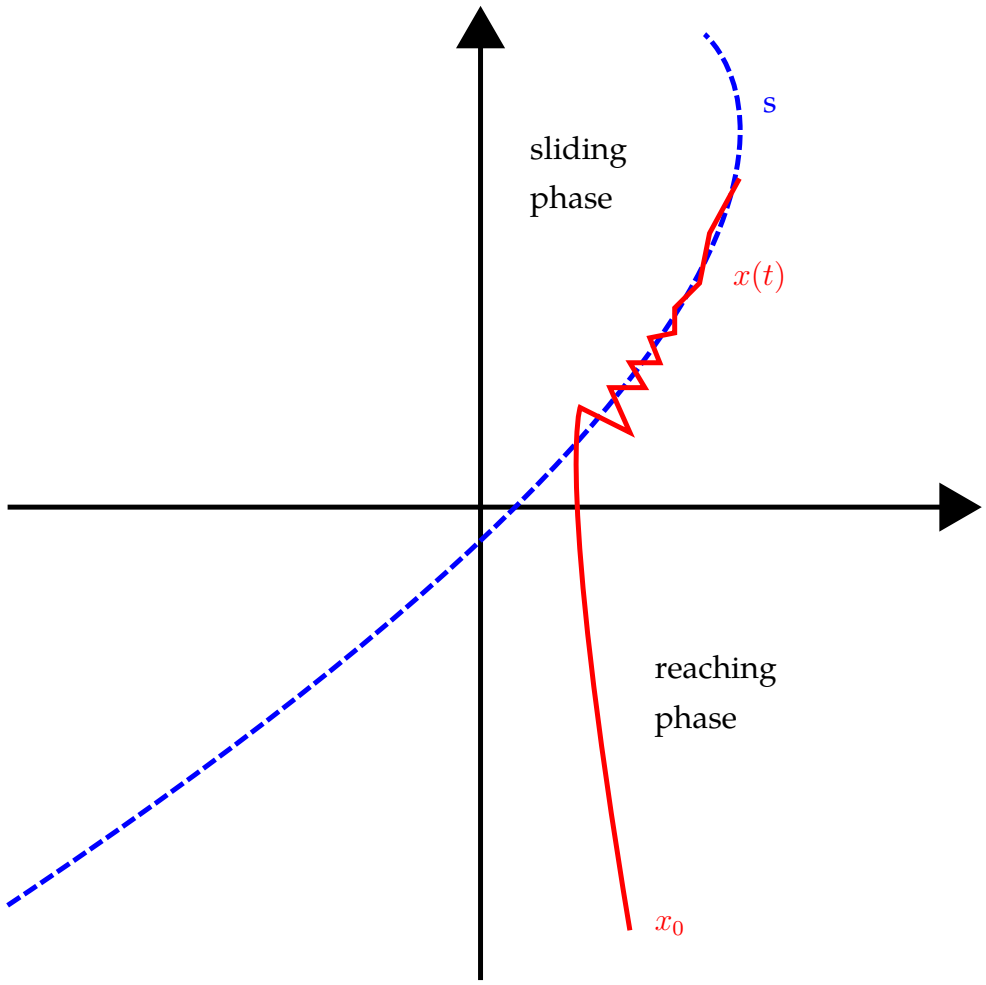

Figure 5.2: SMC typical behavior

where the operator $\otimes$ is the quaternion product operator. The derivative of the sliding surface $\mathbf{s}$ is defined as

$$\begin{aligned}\dot{\mathbf{s}} &= \dot{\boldsymbol{\omega}}_r - \dot{\boldsymbol{\omega}} + k_2\dot{\tilde{\mathbf{q}}} \\ &= \dot{\boldsymbol{\omega}}_r + \mathbf{J}^{-1}\boldsymbol{\omega} \times \mathbf{J}\boldsymbol{\omega} - \mathbf{J}^{-1}\mathbf{u} + \frac{k_2}{2}(\tilde{q}_0\tilde{\boldsymbol{\omega}} + \tilde{\mathbf{q}} \times (\boldsymbol{\omega}_r + \boldsymbol{\omega}))\end{aligned} \tag{5.4}$$

When $\dot{\mathbf{s}} = 0$, the sliding surface is invariant. Imposing $\dot{\mathbf{s}} = 0$ and inverting with respect to $\mathbf{u}$ the above expression, we obtain

$$\mathbf{u}_s = \mathbf{J}\left(\dot{\boldsymbol{\omega}}_r + \frac{k_2}{2}(\tilde{q}_0\tilde{\boldsymbol{\omega}} + \tilde{\mathbf{q}} \times (\boldsymbol{\omega}_r + \boldsymbol{\omega}))\right) + \boldsymbol{\omega} \times \mathbf{J}\boldsymbol{\omega} \tag{5.5}$$

The SMC control input $\mathbf{u}_s$ at this stage guarantee only the invariance property. In order to make the surface attractive, as described in the previous section, the additional term

$$\mathbf{u}_a = k_1\mathbf{J}\tanh(\eta\mathbf{s}) \tag{5.6}$$

is added to the control input. This term steer the trajectory towards the sliding surface thanks to the dependence on the sign of the sliding surface and it is active only when

$\mathbf{s} \neq 0$. In the sliding control theory several attractive terms has been proposed [36]. The choice of this term is a trade off between the convergence speed and the chattering. The proposed function $\tanh$ proved to be more robust to chattering with respect to other functions, i.e. the sign function. Finally, the complete control law is

$$\mathbf{u} = \mathbf{u}_s + \mathbf{u}_a \tag{5.7}$$

5.3 Optimal solar array rotation angle

The Eutelsat 172B SA can rotate around the y-axis of the spacecraft main body. In order to maximize the solar energy converted into electrical energy, the optimal rotation angle shall be found. The Sun direction with respect to the satellite $\hat{\mathbf{r}}_s$ and the normal direction of the SA surface with respect to to the satellite $\hat{\mathbf{n}}_{SA}$ are given. The objective is to find the optimal rotation angle that minimize the angle ϕ_{SA}, which is a 3D angle, between $\hat{\mathbf{r}}_s$ and $\hat{\mathbf{n}}_{SA}$. A graphical representation of these vectors and angles is provided in Figure 5.3.

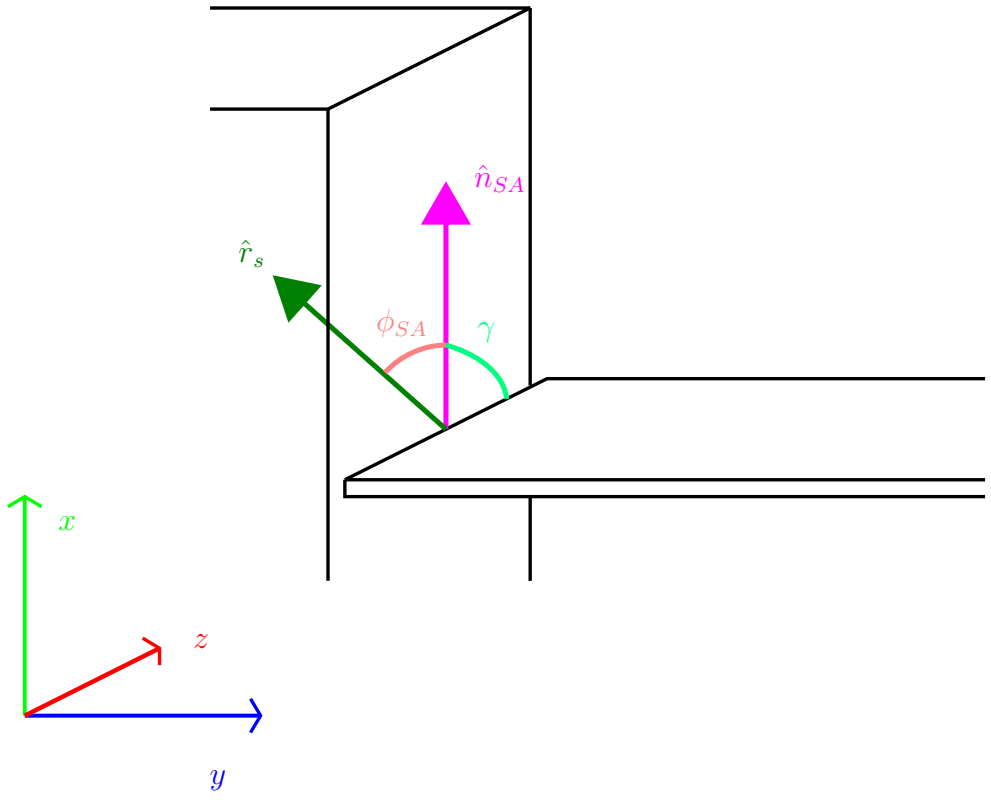

Figure 5.3: Angle ϕ_{SA} and γ representation in body reference frame

The versor $\hat{\mathbf{r}}_s$ can be rotated around the y-axis by the solar array angle γ in the body reference frame, thus the dependency can be written as

$$\hat{\mathbf{n}}_{SA}^{R} = \begin{bmatrix} \cos(\gamma) & 0 & \sin(\gamma) \\ 0 & 1 & 0 \\ -\sin(\gamma) & 0 & \cos(\gamma) \end{bmatrix} \hat{\mathbf{n}}_{SA} \tag{5.8}$$

where $\hat{\mathbf{n}}_{SA}^{R}$ represents the vector $\hat{\mathbf{n}}_{SA}$ rotated around the body y-axis by an angle γ_{SA}. Recalling the scalar product formula that relates the angle between the two vectors, we have

$$\hat{\mathbf{r}}_s \cdot \hat{\mathbf{n}}_{SA} = |\hat{\mathbf{n}}_{SA}||\hat{\mathbf{r}}_s|\cos(\phi_{SA}) \tag{5.9}$$

Since the two vector are versors, the formula simplifies into

$$\hat{\mathbf{r}}_s \cdot \hat{\mathbf{n}}_{SA} = \cos(\phi_{SA}) \tag{5.10}$$

The SA are double faced, this means that there are the same number of solar cells on each face. In mathematical terms this translates into the addition of the absolute value in both sides of equation 5.10 resulting in

$$|\hat{\mathbf{r}}_s \cdot \hat{\mathbf{n}}_{SA}| = \cos(\phi_{SA}) \tag{5.11}$$

The objective is now to find the angle θ_{SA} that maximize the left hand side of equation 5.11. Let us define the vector components of $\hat{\mathbf{r}}_s$ and $\hat{\mathbf{n}}_{SA}$ as

$$\hat{\mathbf{r}}_s = \begin{bmatrix} r_s^x \\ r_s^y \\ r_s^z \end{bmatrix} \quad \hat{\mathbf{n}}_{SA} = \begin{bmatrix} 1 \\ 0 \\ 0 \end{bmatrix} \tag{5.12}$$

The quantity H to be maximized can be expressed as

$$H(\gamma_{SA}) = |r_s^z \cos(\gamma) - r_s^x \sin(\gamma)| \tag{5.13}$$

The optimization problem becomes

$$\theta_{SA} = \underset{\gamma \in [-\pi/2, -\pi/2]}{\operatorname{argmax}} \; H(\gamma) \tag{P.2}$$

The problem in P.2 is a nonlinear optimization problem [1]. Problem P.2 is solved continuously during the simulation generating the optimal trajectory for the SADA rotation angle γ. The possibility to rotate the SA can increase significantly the production of energy, nearly doubling it as can be seen in figure 5.4.

[1] The function used to solve the problem is `fmincon`, which is a nonlinear multivariable constrained problem solver.

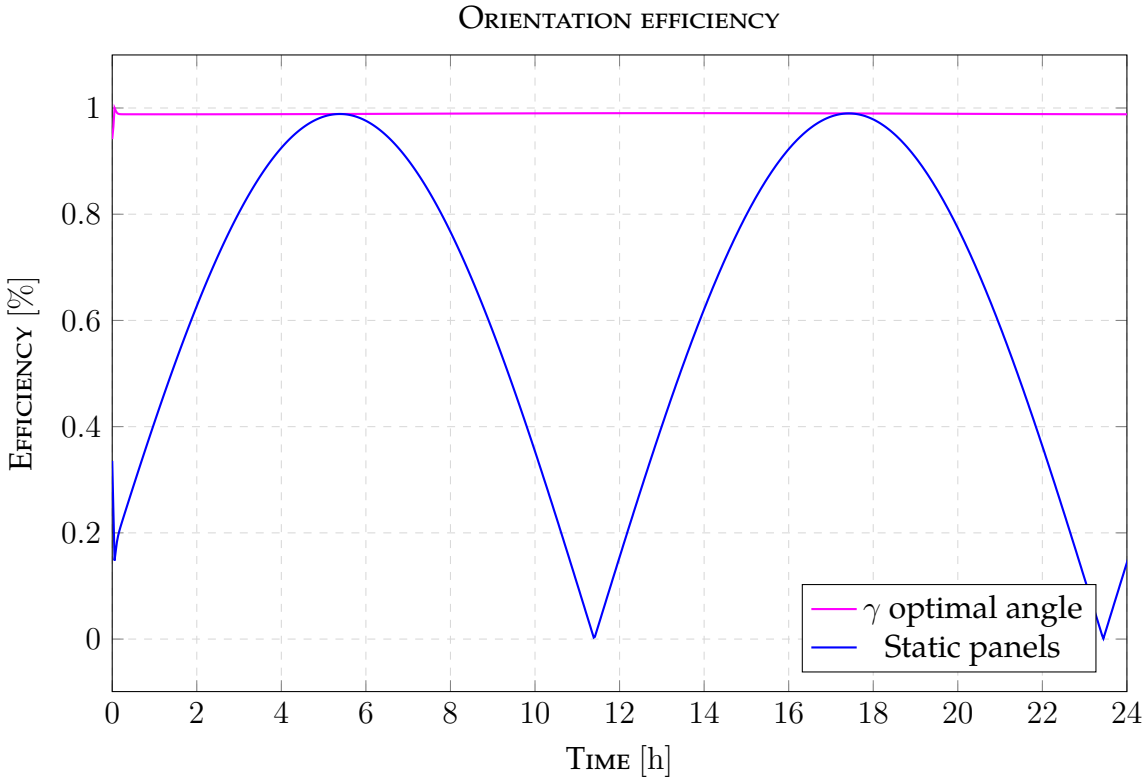

Figure 5.4: Comparison of the efficiency obtained using the rotating solar panel with respect to the static configuration

5.4 Linear Quadratic Regulator (LQR)

Optimal control theory is related to operate a system at a some specified minimum cost [5]. The linear quadratic problem embrace all the system where the plant dynamics is linear and the cost function is quadratic. Linear Quadratic Regulator (LQR) control is a classical feed back control method in the field of optimal control. The Linear Quadratic Regulator (LQR) algorithm is essentially an automated way of finding a state-feedback controller given the cost function weights. There are different types of LQR controllers, the one used in this thesis is the discrete time infinite horizon version. Hereafter the basic theory of the controller is reported.
The plant of the system to be controlled is described by the state space difference equation

$$\mathbf{x}_{k+1} = \mathbf{A}\mathbf{x}_k + \mathbf{B}\mathbf{u}_k \tag{5.14}$$

where $\mathbf{x}_k$ and $\mathbf{u}_k$ are respectively the state and the input at time instant k, matrix $\mathbf{A}$ is the state matrix and $\mathbf{B}$ is the input matrix. The cost function of the LQR control is defined by

$$V = \sum_{k=0}^{\infty} \left(\|\mathbf{x}_k\|^2_{\mathbf{Q}} + \|\mathbf{u}_k\|^2_{\mathbf{R}} \right) \tag{5.15}$$

where $\mathbf{Q}$ is the weight matrix for the state and $\mathbf{R}$ is the weight matrix for the input. The optimal control sequence minimizing the cost function is given by

$$\mathbf{u}_k = -\mathbf{K}\mathbf{x} \tag{5.16}$$

where the gain matrix $\mathbf{K}$ is computed from

$$\mathbf{K} = (\mathbf{R} + \mathbf{B}^T\mathbf{W}\mathbf{B})^{-1}\mathbf{B}^T\mathbf{W}\mathbf{A} \tag{5.17}$$

where the matrix $\mathbf{W}$ is the unique positive definite solution of the discrete time algebraic Riccati equation

$$\mathbf{W} = \mathbf{A}^T\mathbf{W}\mathbf{A} + \mathbf{Q} - \mathbf{A}^T\mathbf{W}\mathbf{B}(\mathbf{R} + \mathbf{B}^T\mathbf{W}\mathbf{B})^{-1}\mathbf{B}^T\mathbf{W}\mathbf{A} \tag{5.18}$$

By introducing the Equation (5.16) in Equation (5.15) the cost function can be equivalently rewritten as

$$V = \|\mathbf{x}_0\|^2_{\mathbf{P}} \tag{5.19}$$

where the matrix $\mathbf{W}$ is the solution of the Equation (5.18).

5.4.1 SADA LQR control

The SADA controller is a saturated LQR. This controller performs the rotation of the solar panels following the trajectory defined in P.2. The dynamic equation of the SADA from the multibody model is 4.40. If we consider the system in a neighborhood of the trajectory, the last two terms of the left hand side of Equation 4.40 can be neglected making the SADA model linear in γ, thus the simplified equation becomes

$$I_2^{22}\ddot{\gamma} + c_\gamma\dot{\gamma} = T_m \tag{5.20}$$

In any case when the the satellite is out of the attitude trajectory the SADA actuator can be locked in position, thus making the system behave like a rigid body for the recovery procedures. The torque input is saturated since it can inject additional torque disturbance and cause a failure of the attitude trajetory tracking which is of primarily importance. The state space model of Equation (5.20) is given by

$$\begin{bmatrix}\dot{\gamma}\\ \ddot{\gamma}\end{bmatrix} = \begin{bmatrix}0 & 1\\ 0 & \dfrac{I_2^{22}}{c_\gamma}\end{bmatrix}\begin{bmatrix}\gamma\\ \dot{\gamma}\end{bmatrix} + \begin{bmatrix}0\\ \dfrac{1}{I_2^{22}}\end{bmatrix}T_m \tag{5.21}$$

5.5 Tube Robust Model Predictive Control (TRMPC)

RMPC is a control technique that ensures robust constraint satisfaction, system stability and optimized performance in the presence of uncertainty. Generally, in the RMPC schemes, robustness properties are guaranteed with the drawback of increased computational complexity. In the last decade a major research output in RMPC has resulted in algorithms that guarantee constraint satisfaction despite the presence of uncertainty, but also to reduce the computational burden. One of the algorithms that

presents a good trade-off between robustness and computational complexity when the disturbance are bounded is the Tube Robust Model Predictive Control (TRMPC). The key feature of the TRMPC is the offline constraint tightening, that ensures the robust satisfaction of the constraints while keeping the computational load comparable to the classical MPC [17]. In the following, the main concepts of the TRMPC are presented, for further information refer to [5, 42]

5.5.1 Model Predictive Control (MPC)

The MPC is a natural evolution of the LQR. The MPC philosophy can be summarized briefly as follows. Predict future behavior using a system model, given measurements or estimates of the current state of the system and a hypothetical future input trajectory or feedback control policy [42]. The fundamentals are similar, they both deal with the control of linear systems to be driven by the solution of an quadratic optimization problem. The innovation of the MPC is that the state and input constraints are included in the problem. The disadvantage in the MPC approach with respect to the LQR methods is the a quadratic optimization problem shall be continuously solved online, but thanks to the advancements in computational processing power of inexpensive microprocessors the problem is becoming less important. The outcome of the MPC is a time varying feedback control law with respect to the LQR which implements a static feedback gain. The MPC is now briefly discussed [42]. Let us define the linear difference system to be controlled defined as

$$\mathbf{x}_{k+1} = \mathbf{A}\mathbf{x}_k + \mathbf{B}\mathbf{u}_k \tag{5.22}$$

where $\mathbf{x} \in \mathbb{R}^n$ is the system state vector, n is the number of states, $\mathbf{u} \in \mathbb{R}^m$ is the system input vector, m is the number of inputs, $\mathbf{A}$ is the state matrix and $\mathbf{B}$ is the input matrix. The state x and the input u are constrained to

$$\mathbf{x} \in \mathbb{X}, \quad \mathbf{u} \in \mathbb{U} \tag{5.23}$$

where $\mathbb{X}$ is the state constraint set and $\mathbb{U}$ is the input constraint set. The regulation problem is concerned with the design of a controller that drives the system state to some desired reference point using an acceptable amount of control effort. In the case where desired reference point is the origin, the controller performance is quantified by a quadratic cost function defined as

$$V = \sum_{k=0}^{\infty} \left(\|\mathbf{x}_k\|_Q^2 + \|\mathbf{u}_k\|_R^2 \right) \tag{5.24}$$

where $\mathbf{Q}$ and $\mathbf{R}$ are weighting matrices that specify the importance of particular states and inputs in the cost function. The prediction horizon employed in Equation (5.24) is infinite. Thus, if every element of the infinite sequence of predicted inputs is treated as free variable, then the constrained minimization of the function in Equation (5.24) would be an infinite-dimensional optimization problem, which is in principle unfeasible. To tackle this problem the dual-mode paradigm is applied. The dual-mode prediction paradigm splits the prediction horizon into two intervals. The first mode considers the predicted control inputs over the first N prediction time steps for some

finite horizon N, whereas the second mode refers to the control law over the subsequent infinite interval. The second mode predicted inputs are specified by a fixed feedback law, which is typically designed considering the LQR solution of the cost function, thus without accounting for the constraints. This technique make reduces the number of optimization variable for the problem from infinite to N. Unfortunately by applying an unconstrained control to the second mode prediction nothing can be said about the constraint satisfaction after the first N steps. The constraints satisfaction condition for the MPC problem are enforced by constraining the state prediction $\mathbf{x}_N$ to lie in a Controlled positive invariant set (CPI) for the system and the constraints. A set $\mathbb{D}$ is said CPI under the dynamics 5.22 and constraints 5.23, if there exist an input $\mathbf{u} \in \mathbb{U}$ such that the predicted state $\mathbf{x}_{k+1}$ is in $\mathbb{D}$. Thus this set is a subset of the original constraints set $\mathbb{X}$. The cost function 5.24 shall be modified to apply the dual-mode paradigm, i.e. set as optimization variables only the first N terms of the control input sequence $\mathbf{U} = [\,\mathbf{u}_0 \;\ldots\; \mathbf{u}_{N-1}]^T$. This can be accomplish by splitting the cost function into two terms. The first term is the summation of the first N entries of the cost function V which include all the optimization variables. This term is defined as

$$V_1 = \sum_{k=0}^{N-1} \left(\|\mathbf{x}_k\|_Q^2 + \|\mathbf{u}_k\|_R^2 \right) \tag{5.25}$$

where $\mathbf{Q}$ is the weight matrix for the state and $\mathbf{R}$ is the weight matrix for the input. The second term account for all the other cost indexes from $N \to \infty$, thus by using the Equation (5.19) the second term is defined as

$$V_2 = \|\mathbf{x}_N\|_W^2 \tag{5.26}$$

where $\mathbf{W}$ is the solution of the discrete time Riccati Equation (5.18). Thus the complete cost function can be written as

$$V = \sum_{k=0}^{N-1} \left(\|\mathbf{x}_k\|_Q^2 + \|\mathbf{u}_k\|_R^2 \right) + \|\mathbf{x}_N\|_W^2 \tag{5.27}$$

Summarizing the MPC problem described before can be cast in the following optimization problem

$$\begin{aligned} \underset{\mathbf{U}}{\text{argmin}} \quad & \sum_{k=0}^{N-1} \left(\|\mathbf{x}_k\|_{\mathbf{Q}}^2 + \|\mathbf{u}_k\|_{\mathbf{R}}^2 \right) + \|\mathbf{x}_N\|_{\mathbf{W}}^2 \\ \text{subject to} \quad & \mathbf{x}_{i+1} = \mathbf{A}\mathbf{x}_i + \mathbf{B}\mathbf{u}_i, \quad \forall i = 0, \ldots, N-1 \\ & \mathbf{x}_i \in \mathbb{X}, \quad \forall i = 0, \ldots, N \\ & \mathbf{u}_i \in \mathbb{U}, \quad \forall i = 0, \ldots, N-1 \\ & \mathbf{x}_N \in \mathbb{D} \end{aligned} \tag{P.3}$$

5.5.2 TRMPC of linear system with additive disturbance

Let us consider the linear system

$$\mathbf{x}_{k+1} = \mathbf{A}\mathbf{x}_k + \mathbf{B}\mathbf{u}_k + \mathbf{w}_k \tag{5.28}$$

where $\mathbf{x} \in \mathbb{R}^n$ is the system state vector, n is the number of states, $\mathbf{u} \in \mathbb{R}^m$ is the system input vector, m is the number of inputs. The vector $\mathbf{w} = \mathbf{D}\boldsymbol{\xi}$ is the additive disturbance where $\boldsymbol{\xi}$ lies in a compact convex polyhedral set Ξ that contains the origin. Hence due to the affine transformation also $\mathbf{w}$ lies in a compact convex polyhedral set $\mathbb{W}$ that contains the origin and the system couple $(\mathbf{A}, \mathbf{D})$ is considered controllable. Both the state and the input are constrained in polyhedral set, $\mathbf{x} \in \mathbb{X}$ and $\mathbf{u} \in \mathbb{U}$ respectively. These two set can be describe in inequality form as mixed constrains defined as

$$\mathbf{F}\mathbf{x}_k + \mathbf{G}\mathbf{u}_k \leq \mathbf{1} \tag{5.29}$$

where $\mathbf{F} \in \mathbb{R}^{s\times m}$ and $\mathbf{G} \in \mathbb{R}^{s\times n}$ are matrices derived from the definitions of $\mathbb{X}$ and $\mathbf{U}$, s is the number of rows of $\mathbf{F}$ and $\mathbf{G}$. The term $\mathbf{1} = [1 \dots 1]^T$ is a column vector with elements equal to unity, the dimension of which is context dependent, i.e. in this specific case the dimension is s

Thanks to the linearity of the Equation (5.28), the component of the predicted state that is generated by the disturbance input evolves independently of the optimization variables. Since the constraints (5.29) are also linear, the worst-case disturbances with respect to these constraints do not depend on the optimization variables and can therefore be determined offline. This leads to a computationally convenient method of handling constraints for open-loop optimization strategies. In fact the resulting constraints on predicted states and inputs are of the same form as those of the classical, i.e without uncertainty, MPC problem, and are simply tightened to account for the uncertainty in predictions [42]. The dynamics of the system (5.28) can thus be splitted into two different dynamics: the nominal dynamics and the error dynamics. The predicted is thus decomposed into nominal and uncertain components, denoted as $\mathbf{z}$ and $\mathbf{e}$, respectively. Let the nominal and the error system be described by

$$\mathbf{z}_{k+1} = \mathbf{A}\mathbf{z}_k + \mathbf{B}\mathbf{u}_k \tag{5.30}$$

$$\mathbf{e}_{k+1} = \mathbf{A}\mathbf{e}_k + \mathbf{w}_k \tag{5.31}$$

where the deviation of the actual state from the nominal state is $\mathbf{e}_k = \mathbf{x}_k - \mathbf{z}_k$. The set $\mathcal{S}(i)$ is defined by

$$\mathcal{S}(i) = \bigoplus_{j=0}^{i-1} \mathbf{A}^j \mathbb{W} \tag{5.32}$$

where $\oplus$ is the Minkowski sum operator. If matrix $\mathbf{A}$ is stable, then, the set $\mathcal{S}(\infty)$ exist and it is positive invariant for $\mathbf{e}_{k+1} = \mathbf{A}\mathbf{e}_k + \mathbf{w}_k$ i.e. $\mathbf{e}_k \in \mathcal{S}(\infty)$ implies $\mathbf{A}\mathbf{e}_k + \mathbf{w}_k \in \mathcal{S}(\infty), \forall \mathbf{w}_k \in \mathbb{W}$, also $\mathcal{S}(i) \to \mathcal{S}(\infty)$ as $i \to \infty$ [43]. The feedback time varying control law implement is

$$\mathbf{u}_k = \mathbf{v}_k + \mathbf{K}(\mathbf{x}_k - \mathbf{z}_k) \tag{5.33}$$

where $\mathbf{x}_k$ is the actual state, $\mathbf{z}_k$ is the nominal state and $\mathbf{v}_k$ is the nominal input and $\mathbf{K}$ is the control gain matrix defined such that the error dynamics eigenvalues are stable. By applying this control strategy the system equation for $\mathbf{x}_k$ is

$$\mathbf{x}_{k+1} = \mathbf{A}\mathbf{x}_k + \mathbf{B}\mathbf{v}_k + \mathbf{B}\mathbf{K}\mathbf{e}_k + \mathbf{w}_k \tag{5.34}$$

the nominal system corresponding to the state system 5.34 is

$$\mathbf{z}_{k+1} = \mathbf{A}\mathbf{z}_k + \mathbf{B}\mathbf{v}_k \tag{5.35}$$

The deviation $\mathbf{e}$ now satisfies the difference equation

$$\mathbf{e}_{k+1} = \mathbf{A}_k\mathbf{e}_k + \mathbf{w}_k, \quad \mathbf{A}_k = \mathbf{A} + \mathbf{B}\mathbf{K} \tag{5.36}$$

As mentioned before, the gain matrix $\mathbf{K}$ is chosen such that $\mathbf{A}_k$ is stable, then the new uncertainty set $\mathcal{S}_k(i)$ is defined by

$$\mathcal{S}_K(i) = \bigoplus_{j=0}^{i-1} \mathbf{A}_k^j \mathbb{W} \tag{5.37}$$

Considering that the error dynamics is uncoupled from the nominal dynamics and that the error set $\mathbb{W}$ is bounded, the tube that contains all the possible realization of the error, given that the error initial condition $\mathbf{e}_0$ lies in it, is $\mathcal{S}_K(i)$. This set is difficult to compute in closed form, thus an outer approximation procedure, described in subsection 5.5.4, is used to compute it. The outer-bounding approximation of $\mathcal{S}_K(\infty)$ is called S. The tube S features a constant cross section and it will be the tube used for the design of the TRMPC. The goal of TRMPC is to ensure that $\mathbf{z}_i \to 0$ as $i \to 0$, so that the state $\mathbf{x}_i$, which lies in the tube $\mathcal{X}_i = \{\mathbf{z}_i\} \oplus \mathcal{S}$, tends to $\mathcal{S}$ as $i \to \infty$. This idea can be visualized in Figure 5.5.

The fact that the state and control trajectories of the uncertain system lie in known neighborhoods of the state and control trajectories, $\mathbf{z}_i$ and $\mathbf{v}_i$ respectively, is the basis for TRMPC described subsequently. It follows from this fact that if $\mathbf{z}_i$ and $\mathbf{v}_i$ are chosen to satisfy $\mathbf{z}_i \oplus \mathcal{S}_k(\infty) \subset \mathbb{X}$ and $\mathbf{z}_i \oplus \mathbf{K}\mathcal{S}_k(\infty)$ for all $i \in \mathbb{I}_{\geq 0}$, then $\mathbf{x}_i \in \mathbb{X}$ and $\mathbf{u}_i \in \mathbb{U}$ for all $i \in \mathbb{I}_{\geq 0}$. The vectors $\mathbf{z}_i$ and $\mathbf{v}_i$ should be chosen to satisfy the tighter constraints [5]

$$\mathbf{z}_i \in \mathbb{Z} = \mathbb{X} \ominus \mathcal{S} \tag{5.38}$$

$$\mathbf{v}_i \in \mathbb{V} = \mathbb{X} \ominus \mathbf{K}\mathcal{S} \tag{5.39}$$

for all $i \in \mathbb{I}_{\geq 0}$, where $\ominus$ is the Pontryagin difference operator. We suppose that $\mathcal{S} \subset \mathbb{X}$ and $\mathbf{K}\mathcal{S} \subset \mathbb{U}$. This assumption is needed because if $\mathbb{W}$ is too large, there is no possibility of satisfying the constraints for all realizations of the disturbance sequence $\mathbf{w}$. Summarizing, the state and control constraints, $\mathbf{x}_k \in \mathbb{X}$ and $\mathbf{u}_k \in \mathbb{U}$, are satisfied at each time i if the control law (5.33) is employed, and the nominal system (5.35) satisfies the tighter constraints (5.38-5.39), in addition

$$\mathbf{x}_0 \in \mathbf{z}_0 \oplus \mathcal{S}, \quad \mathbf{e}_0 \in \mathcal{S} \tag{5.40}$$

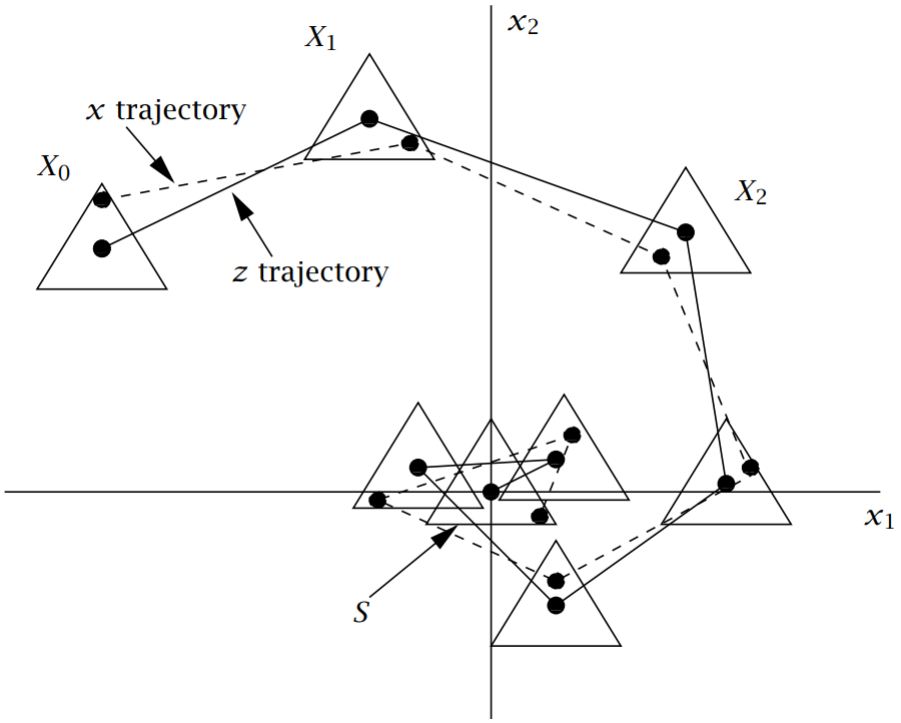

Figure 5.5: TRMPC trajectories evolution [credit [5]]

in which $\mathcal{S}$ is Robust Positive Invariant (RPI) for $\mathbf{e}^+ = \mathbf{A}_k\mathbf{e} + \mathbf{w}$, $\mathbf{w} \in \mathbb{W}$. Satisfaction of constraint after time N, is enforced by constraining the state $\mathbf{z}_N$ to lie in a terminal set $\mathbb{Z}_f$, which is CPI for the dynamics and the constraints, following the same procedure described in subsection 5.5.1

$$\mathbf{z}_N \in \mathbb{Z}_f, \quad \mathbb{Z}_f \subset \mathbb{Z} \tag{5.41}$$

The cost function selection process is equal to the one presented in subsection 5.5.1, where the state $\mathbf{x}$ is substituted by the nominal state $\mathbf{z}$ and the control input $\mathbf{u}$ is substituted by the nominal control input $\mathbf{v}$. Thus, the TRMPC cost function is defined as

$$V = \sum_{k=0}^{N-1} \left(\|\mathbf{z}_k\|_Q^2 + \|\mathbf{v}_k\|_R^2 \right) + \|\mathbf{z}_N\|_W^2 \tag{5.42}$$

where $\mathbf{Q}$ is the weight matrix for the state, $\mathbf{R}$ is the weight matrix for the input and $\mathbf{W}$ is the solution of the Riccati Equation 5.18.

The final TRMPC algorithm is described by Algorithm 1.

Algorithm 1: Tube-based model predictive controller.

Initialization: At time i = 0, set x = z = x(0) in which x(0) is the current state.

Step 1 COMPUTE CONTROL: At time i and current state $(\mathbf{x}_i, \mathbf{z}_i)$, solve the nominal optimal control problem $\mathbb{P}_N(\mathbf{z_i})$ to obtain the nominal control action $\mathbf{v}_i$ and the control action $\mathbf{u}_i = \mathbf{v}_i + \mathbf{K}(\mathbf{x}_i - \mathbf{z}_i)$.

Step 2 CHECK: If $\mathbb{P}_N(\mathbf{z}_i)$ is unfeasible, adopt safety/recovery procedure.

Step 3 APPLY CONTROL: Apply the control $\mathbf{u}_i$ to the system being controlled.

Step 4 UPDATE: Measure the successor state $\mathbf{x}_{i+1}$ of the system being controlled and compute the successor

Step 5: Set $(\mathbf{x}_i, \mathbf{z}_i) = (\mathbf{x}_{i+1}, \mathbf{z}_{i+1})$, set $i = i + 1$, and go to Step 1.

The TRMPC related optimization problem structure is

$$\begin{aligned} \underset{\mathbf{V}}{\text{argmin}} \quad & \sum_{k=0}^{N-1} \left(\|\mathbf{z}_k\|^2_{\mathbf{Q}} + \|\mathbf{v}_k\|^2_{\mathbf{R}} \right) + \|\mathbf{z}_N\|^2_{\mathbf{W}} \\ \text{subject to} \quad & \mathbf{z}_{i+1} = \mathbf{A}\mathbf{z}_i + \mathbf{B}\mathbf{v}_i, \quad \forall i = 0, \ldots, N-1 \\ & \mathbf{z}_i \in \mathbb{Z}, \quad \forall i = 0, \ldots, N \\ & \mathbf{v}_i \in \mathbb{V}, \quad \forall i = 0, \ldots, N-1 \\ & \mathbf{z}_N \in \mathbb{Z}_f \\ & \mathbf{x}_0 - \mathbf{z}_0 \in \mathcal{S} \end{aligned} \tag{P.3}$$

where $\mathbf{V} = [\, \mathbf{v}_0 \; \ldots \; \mathbf{v}_{N-1}]^T$ is the input control sequence.

5.5.3 Terminal set $\mathbb{Z}_f$ computation

Let us introduce some definitions [42]:

- The matrix $\mathbf{\Phi}$ is defined as $\mathbf{A} + \mathbf{BK}$, where $\mathbf{K}$ is the gain matrix chosen for the design of the terminal set.
- A set $\mathbb{B}$ is a Positive Invariant set (PI) under the dynamics and constraints defined in 5.28 with the control law $\mathbf{u} = \mathbf{Kx}$ if and only if $\mathbf{u} \in \mathbb{U}$ and $\mathbf{\Phi x} \in \mathbb{B}$ for all $\mathbf{x} \in \mathbb{B}$.
- The Maximal Positive Invariant set (MPI) is the set under the dynamics of 5.28 which is the union of all PI set under these dynamics and constraints.

The set $\mathbb{Z}_f$ is the terminal constraint set for the TRMPC. The reference set that satisfy all the requirements to design this set is the MPI for the system 5.28. The terminal constraint set $\mathbb{Z}_f$ is defined as

$$\mathbb{Z}_f = \{x : (\mathbf{F} + \mathbf{GK})\mathbf{\Phi}^i \mathbf{x} \leq \mathbf{1}, \quad i = 0, \ldots, \nu\} \tag{5.43}$$

where ν is the smallest positive integer such that $(\mathbf{F}+\mathbf{GK})\mathbf{\Phi}^{\nu+1}$, for all $(\mathbf{F}+\mathbf{GK})\mathbf{\Phi}^i,\ i = 0, \ldots, \nu$. The resulting terminal set can be expressed as

$$\mathbb{Z}_f = \{\mathbf{x} : \mathbf{V}_{\mathbb{Z}_f}\mathbf{x} \leq \mathbf{1}\} \tag{5.44}$$

where the matrix $\mathbf{Z}_f$ is defined as

$$\mathbf{Z}_f = \begin{bmatrix} (\mathbf{F} + \mathbf{GK}) \\ (\mathbf{F} + \mathbf{GK})\mathbf{\Phi} \\ \vdots \\ (\mathbf{F} + \mathbf{GK})\mathbf{\Phi}^{\nu} \end{bmatrix} \tag{5.45}$$

5.5.4 Tube $\mathcal{S}$ computation

The computation of set $\mathcal{S}_k(\infty)$ in closed form is computationally unfeasible, thus an approximation $\mathcal{S}$ of this set is computed. The condition that ensures that the error is always contained into the error tube is given by

$$\mathbf{A}_k\mathcal{S} \oplus \mathbf{D}\mathbb{W} \subseteq \mathcal{S} \tag{5.46}$$

The set $\mathcal{S}$ is RPI for 5.36, it is also assumed that $\mathcal{S}$ is compact, convex, and polytopic and is can be thus be described by linear inequalities

$$\mathcal{S} = \{\mathbf{e} : \mathbf{V}_{\mathcal{S}}\mathbf{e} \leq \mathbf{1}\} \tag{5.47}$$

Under these circumstances and the conditions in Equation 5.40 the predicted error trajectory lies in a tube of fixed cross section $\mathcal{S}$. The set $\mathcal{S}_k(\infty)$ of Equation 5.37 can be approximated by [42]

$$\mathcal{S} = \frac{1}{1-\rho}\bigoplus_{j=0}^{r-1}\mathbf{A}_k^j\mathbb{W} \tag{5.48}$$

where the parameters r and $\rho \in [0, 1)$ satisfy

$$\mathbf{A}_k^r D\Xi \subset \rho\mathbf{D}\Xi \tag{5.49}$$

The matrix $\mathbf{A}_k$ is defined in Equation 5.36 and the other quantities are defined in the first part of subsection 5.5.2. The condition in Equation 5.49 can be verified by solving the LP

$$\max_{\boldsymbol{\xi}\in\Xi} \mathbf{V}_{\Xi}\mathbf{D}^{\dagger}\mathbf{A}_k^r\mathbf{D}\boldsymbol{\xi} \leq \rho\mathbf{1} \tag{5.50}$$

where the $\mathbf{D}^{\dagger}$ is the Moore-Penroose inverse of matrix $\mathbf{D}$ and matrix $\mathbf{V}_{\Xi}$ corresponds to the matrix $\mathbf{V}$ defined in Equation 4.75. The grade of approximation metric is the parameter ρ. The closer to 0 the value of ρ, the better the set $\mathbf{S}$ approximates $\mathbf{S}_k(\infty)$. The closer to 0 the value of ρ the more complex the structure of $\mathcal{S}$ is [42].

Chapter 6

Controllers setup and simulation results

6.1 Controllers setup

In this section the setup of the controllers is presented. The choice of the parameter has been conducted by a trial and error procedure, looking for the parameter combination that returns the best tracking error performances.

6.1.1 TRMPC attitude controller

The weight matrices $\mathbf{Q}$, $\mathbf{R}$ and controller gain matrix $\mathbf{K}$ are

$$\mathbf{Q} = \begin{bmatrix} 1000 & 0 & 0 & 0 & 0 & 0 \\ 0 & 1000 & 0 & 0 & 0 & 0 \\ 0 & 0 & 1000 & 0 & 0 & 0 \\ 0 & 0 & 0 & 1 & 0 & 0 \\ 0 & 0 & 0 & 0 & 1 & 0 \\ 0 & 0 & 0 & 0 & 0 & 1 \end{bmatrix} \qquad \mathbf{R} = \begin{bmatrix} 1 & 0 & 0 \\ 0 & 1 & 0 \\ 0 & 0 & 1 \end{bmatrix} \tag{6.1}$$

$$\mathbf{K} = \begin{bmatrix} -6.5 & 552.5 & 13.6 & -6103.9 & 25.6 & 59.5 \\ 306.3 & -3.6 & -13.6 & 14.1 & -3352.5 & -58.1 \\ 43.4 & -24.8 & -649.2 & 105.6 & -187 & -7314.5 \end{bmatrix} \tag{6.2}$$

and matrix $\mathbf{A}$ and $\mathbf{B}$ are defined in section 4.7. The set $\mathbb{X}$ is the constraints set for the states. It has been defined allowing a maximum Euler angles error of 10^{-3} rad and maximum angular velocity error of 10^{-2} $\mathrm{rad\,s^{-1}}$. The set $\mathbb{X}$ is defined as

$$\mathbb{X} = \{\mathbf{v} : \mathbf{V}_{\mathbb{X}}\mathbf{v} \leq \mathbf{1}\} \tag{6.3}$$

where the resulting matrix $\mathbf{V}_{\mathbb{X}}$ is

$$\mathbf{V}_{\mathbb{X}} = \begin{bmatrix} 1000 & 0 & 0 & 0 & 0 & 0 \\ 0 & 1000 & 0 & 0 & 0 & 0 \\ 0 & 0 & 1000 & 0 & 0 & 0 \\ -1000 & 0 & 0 & 0 & 0 & 0 \\ 0 & -1000 & 0 & 0 & 0 & 0 \\ 0 & 0 & -1000 & 0 & 0 & 0 \\ 0 & 0 & 0 & 100 & 0 & 0 \\ 0 & 0 & 0 & 0 & 100 & 0 \\ 0 & 0 & 0 & 0 & 0 & 100 \\ 0 & 0 & 0 & -100 & 0 & 0 \\ 0 & 0 & 0 & 0 & -100 & 0 \\ 0 & 0 & 0 & 0 & 0 & -100 \end{bmatrix} \tag{6.4}$$

The set $\mathbb{V}$ is a polyhedron set obtained from Equation (5.38). The resulting set is computed by exploiting the MPT toolbox [44] and is defined by a set of linear inequalities as

$$\mathbb{V} = \{\mathbf{v} : \mathbf{V}_{\mathbb{V}}\mathbf{v} \leq \mathbf{b}_{\mathbb{V}}\} \tag{6.5}$$

where $\mathbb{G}$ is the set defined in Equation (4.84), matrix $\mathbf{K}$ is defined in Equation (6.2) and $\mathcal{S}$ is the outer approximation of the error dynamics tube computed following the procedure described in subsection 5.5.4. The set $\mathcal{S}$ is a polyhedron set and it is described by

$$\mathcal{S} = \{\mathbf{e} : \mathbf{V}_{\mathcal{S}}\mathbf{e} \leq \mathbf{b}_{\mathcal{S}}\} \tag{6.6}$$

The set $\mathbb{Z}$ is a polyhedron set obtained from Equation (5.39). The resulting set is computed by exploiting the MPT toolbox [44] and is defined by a set of linear inequalities as

$$\mathbb{Z} = \{\mathbf{z} : \mathbf{V}_{\mathbb{Z}}\mathbf{z} \leq \mathbf{b}_{\mathbb{Z}}\} \tag{6.7}$$

Finally the set $\mathbb{Z}_f$ which is a polyhedron is computed by using the gain matrix defined in Equation (6.2) following the procedure described in subsection 5.5.3. The set $\mathbb{Z}_f$ is defined by Equation (5.44) and is described by

$$\mathbb{Z}_f = \{\mathbf{z} : \mathbf{V}_{\mathbb{Z}_f}\mathbf{z} \leq \mathbf{b}_{\mathbb{Z}_f}\} \tag{6.8}$$

The problem P.3 is recast into the following optimization problem readily solvable by a general Quadratic Programming (QP) solver

$$\begin{aligned} \underset{c}{\text{argmin}} \quad & \mathbf{c}^T\mathbf{P}\mathbf{c} \\ \text{subject to} \quad & \mathbf{A}_i\mathbf{c} \leq \mathbf{b}_i \\ & \mathbf{A}_e\mathbf{c} = \mathbf{b}_e \end{aligned} \tag{P.4}$$

$$\mathbf{c} = \begin{bmatrix} \mathbf{z}_0 \\ \vdots \\ \mathbf{z}_N \\ \mathbf{v}_0 \\ \vdots \\ \mathbf{v}_{N-1} \end{bmatrix} \qquad \mathbf{P} = \begin{bmatrix} \mathbf{Q} & 0 & \dots & \dots & \dots & \dots & 0 \\ 0 & \ddots & \ddots & \dots & \dots & \dots & \vdots \\ \vdots & \ddots & \mathbf{Q} & \ddots & \dots & \dots & \vdots \\ \vdots & \vdots & \ddots & \mathbf{W} & \ddots & \dots & \vdots \\ \vdots & \vdots & \vdots & \ddots & \mathbf{R} & \ddots & \vdots \\ \vdots & \vdots & \vdots & \vdots & \ddots & \ddots & 0 \\ 0 & \dots & \dots & \dots & \dots & 0 & \mathbf{R} \end{bmatrix} \tag{6.9}$$

$$\mathbf{A}_e = \begin{bmatrix} \mathbf{A} & -\mathbf{I} & 0 & 0 & \dots & \mathbf{B} & 0 & 0 & \dots \\ 0 & \mathbf{A} & -\mathbf{I} & 0 & \dots & 0 & \mathbf{B} & 0 & \dots \\ \vdots & \vdots & \ddots & \ddots & \vdots & \vdots & \vdots & \ddots & \vdots \\ 0 & \dots & \dots & \mathbf{A} & -\mathbf{I} & 0 & \dots & \dots & \mathbf{B} \end{bmatrix} \qquad \mathbf{b}_e = \begin{bmatrix} 0 \\ \vdots \\ 0 \end{bmatrix} \tag{6.10}$$

$$\mathbf{A}_i = \begin{bmatrix} -\mathbf{V}_{\mathcal{S}} & 0 & \dots & \dots & \dots & \dots & 0 \\ \mathbf{V}_{\mathbb{Z}} & 0 & \dots & \dots & \dots & \dots & \vdots \\ 0 & \ddots & \ddots & \dots & \dots & \dots & \vdots \\ \vdots & \ddots & \mathbf{V}_{\mathbb{Z}} & \ddots & \dots & \dots & \vdots \\ \vdots & \vdots & \ddots & \mathbf{V}_{\mathbb{Z}_f} & \ddots & \dots & \vdots \\ \vdots & \vdots & \vdots & \ddots & \mathbf{V}_{\mathbb{V}} & \ddots & \vdots \\ \vdots & \vdots & \vdots & \vdots & \ddots & \ddots & 0 \\ 0 & \dots & \dots & \dots & \dots & 0 & \mathbf{V}_{\mathbb{V}} \end{bmatrix} \qquad \mathbf{b}_i = \begin{bmatrix} \mathbf{b}_{\mathcal{S}} - \mathbf{V}_{\mathcal{S}}\mathbf{x}_0 \\ \mathbf{b}_{\mathbb{Z}} \\ \mathbf{b}_{\mathbb{Z}_f} \\ \vdots \\ \mathbf{b}_{\mathbb{Z}} \\ \mathbf{b}_{\mathbb{V}} \\ \vdots \\ \mathbf{b}_{\mathbb{V}} \end{bmatrix} \tag{6.11}$$

6.1.2 SMC attitude controller

The SMC parameter to be tuned are k_1, k_2 and η. The best combination found is represented by the values collected in table 6.2. All the other parameters of the controller are related with model properties described in the previous sections.

parameter	value
k_1	2
k_2	0.05
η	0.01

Table 6.1: SMC control parameters

The controller output is saturated due to limits of the actuators presented in section 4.9. The set of admissible control inputs is defined by set defined in Equation (4.84).

6.1.3 SADA LQR controller

The weight matrices chosen are

$$Q = \begin{bmatrix} 100 & 0 \\ 0 & 100 \end{bmatrix} \quad R = 10000 \tag{6.12}$$

The resulting gain matrix for the LQR control is

$$K = \begin{bmatrix} 0.0982 & 5.4456 \end{bmatrix} \tag{6.13}$$

This controller is saturated, the maximum and minimum value are defined in table

parameter	value $[\mathrm{N\,m}]$
max torque	10^{-4}
min torque	-10^{-4}

Table 6.2: SADA control parameters

6.2 Simulation results

The software used to implement and perform the simulations is MATLAB Simulink. The simulations have been run using fixed step solver with $1\,\mathrm{s}$ integration time, whereas the attitude controller is run every $5\,\mathrm{s}$. The simulation time is considerably long, thus the simulation parameters has been chosen considering a trade-off between simulation data quality and simulation time.
The main outcomes of the simulation are the attitude orientation error, the produced power and the fuel consumption. For each simulation scenario these quantities will be presented. The simulation time for each scenario is 1 year. The only components that will be changed in the different simulation scenarios are the controller and the satellite attitude dynamics model, all the other components are common in each scenario. The simulation scenarios are

1. Multibody configuration satellite with rotation solar arrays controlled using the TRMPC

2. Multibody configuration satellite with rotation solar arrays controlled using the SMC

3. Rigid configuration satellite with fixed solar arrays controlled using the TRMPC

4. Rigid configuration satellite with fixed solar arrays controlled using the SMC

6.3 Scenario 1. TRMPC multibody satellite with rotation SA

In the first scenario we obtained the best results, the Euler angles tracking error is the smallest, while the amount of consumed fuel is comparable with the consumption of the second scenario. The production of electric power is almost double with respect to scenarios three and four, wheres is comparable with the electric power generated in the second scenario. One drawback of the TRMPC with respect with the SMC implemented in the second scenario are the small oscillation generated by the controller as can be seen in Figure 6.6. The reference plots of scenario one are: Euler angles tracking error in Figures 6.1 and 6.2, disturbance torques in Figures 6.3 and 6.4, input torque in Figures 6.5 and 6.6, thrust produced by the thrusters in Figures 6.7 and 6.8, the electrical power produced in Figure 6.9 and finally the Xenon fuel consumption in Figure 6.10.

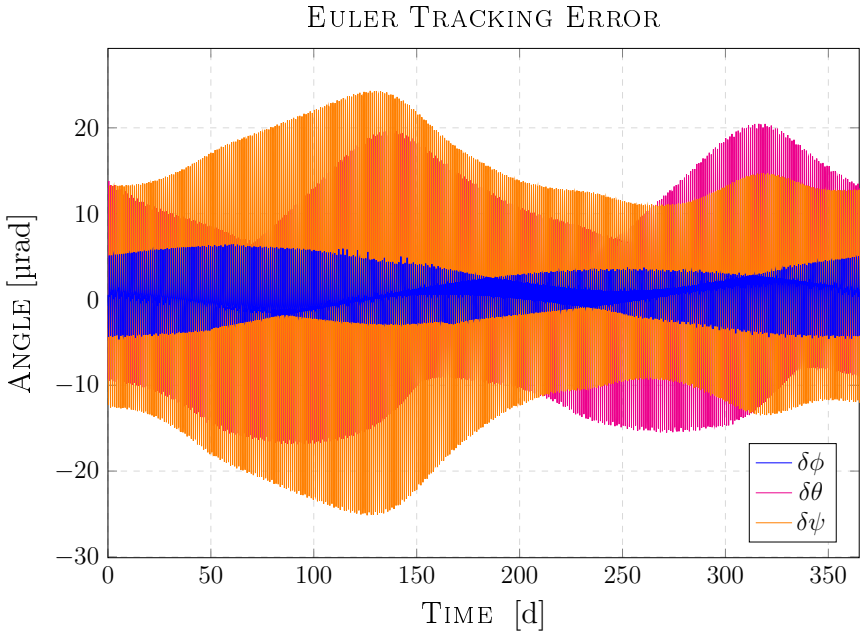

Figure 6.1: Euler tracking error in one year period [TRMPC-multibody]

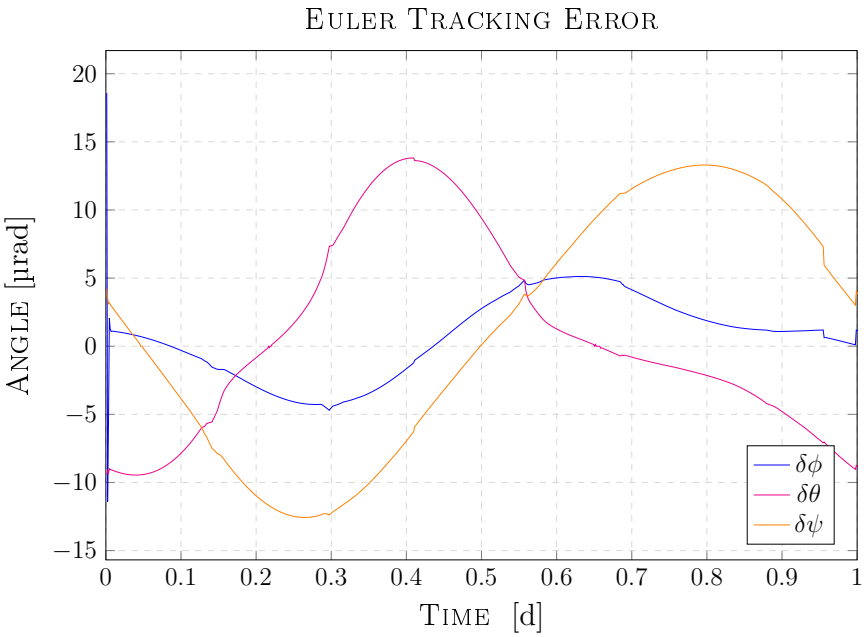

Figure 6.2: Euler tracking error, first day focus [TRMPC-multibody]

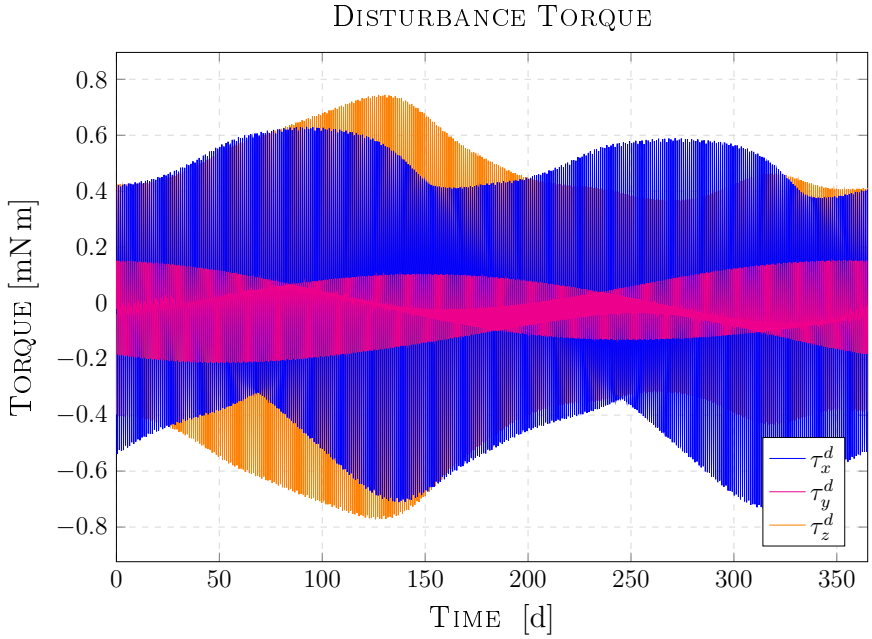

Figure 6.3: Disturbance torque in one year period [TRMPC-multibody]

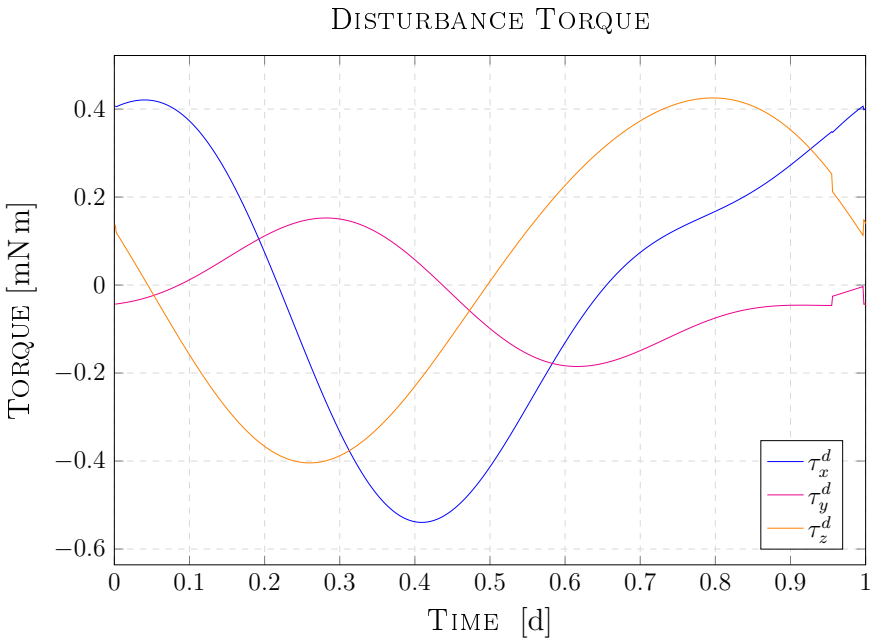

Figure 6.4: Disturbance torque, first day focus [TRMPC-multibody]

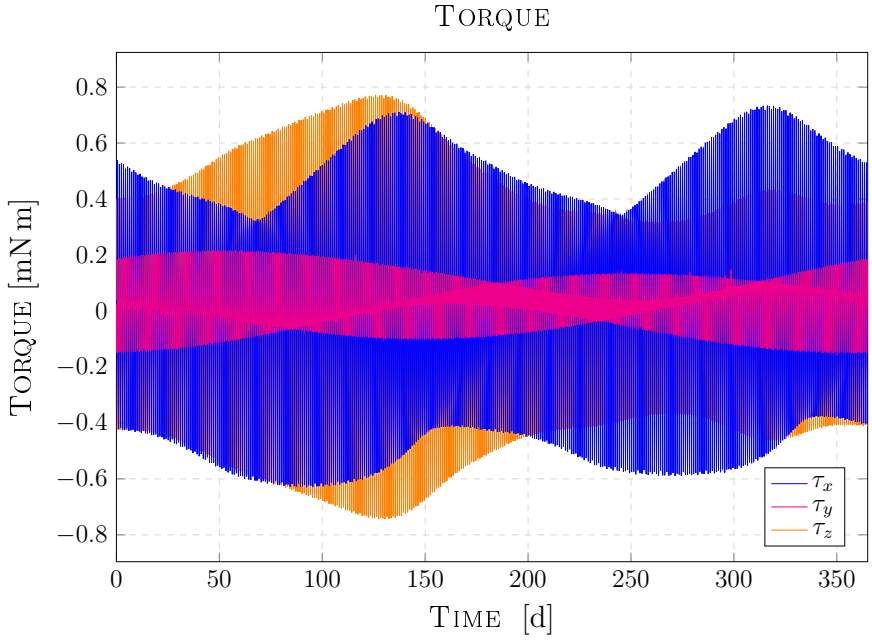

Figure 6.5: Torque in one year period [TRMPC-multibody]

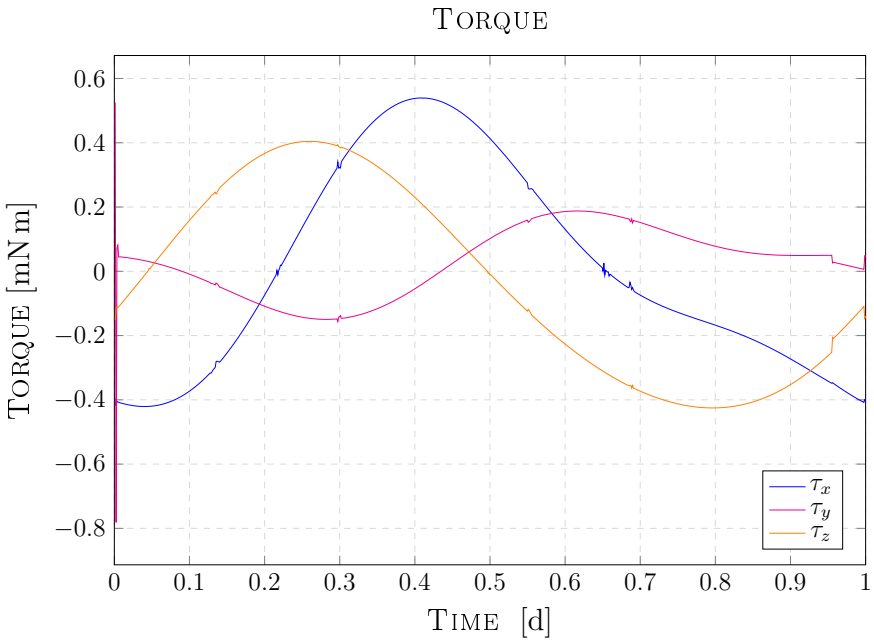

Figure 6.6: Torque, first day focus [TRMPC-multibody]

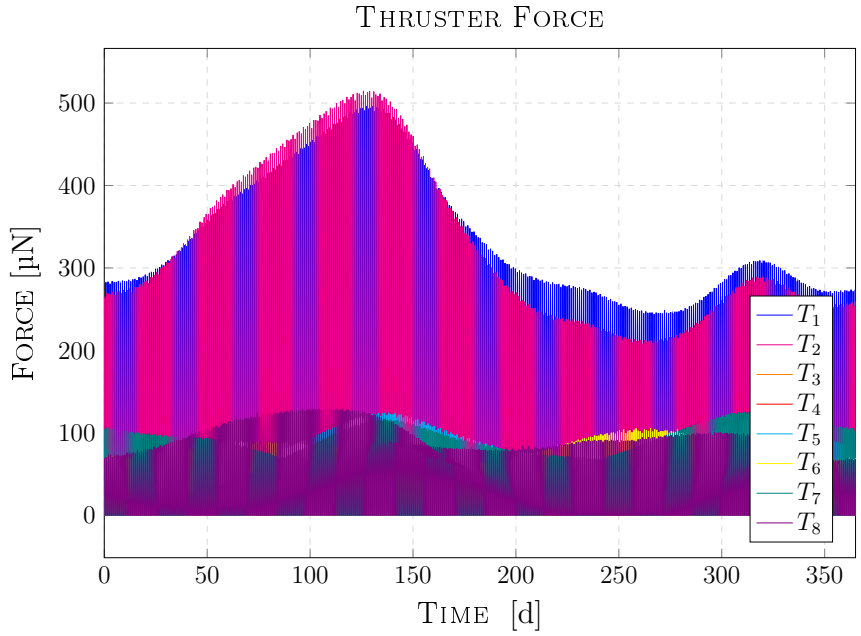

Figure 6.7: Thruster Force in one year period [TRMPC-multibody]

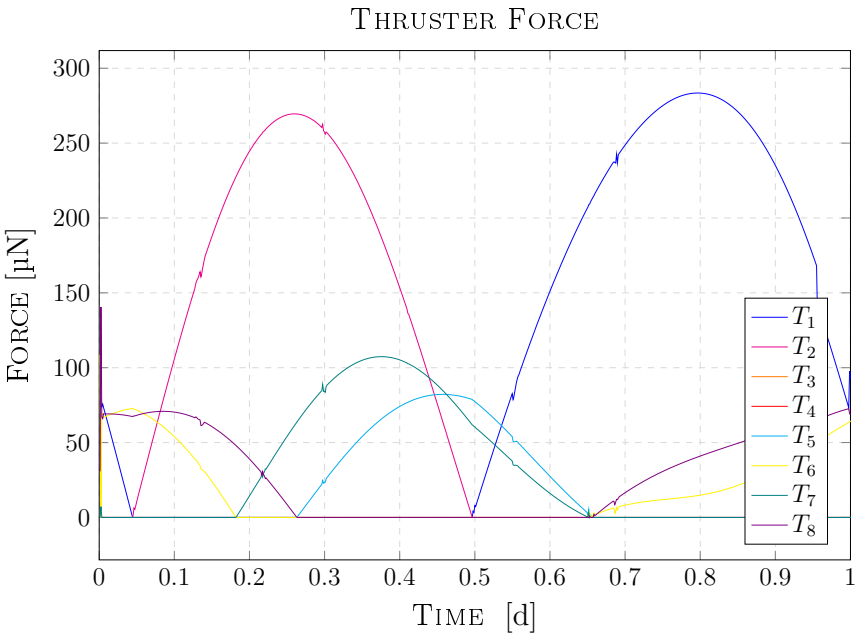

Figure 6.8: Thruster Force, first day focus [TRMPC-multibody]

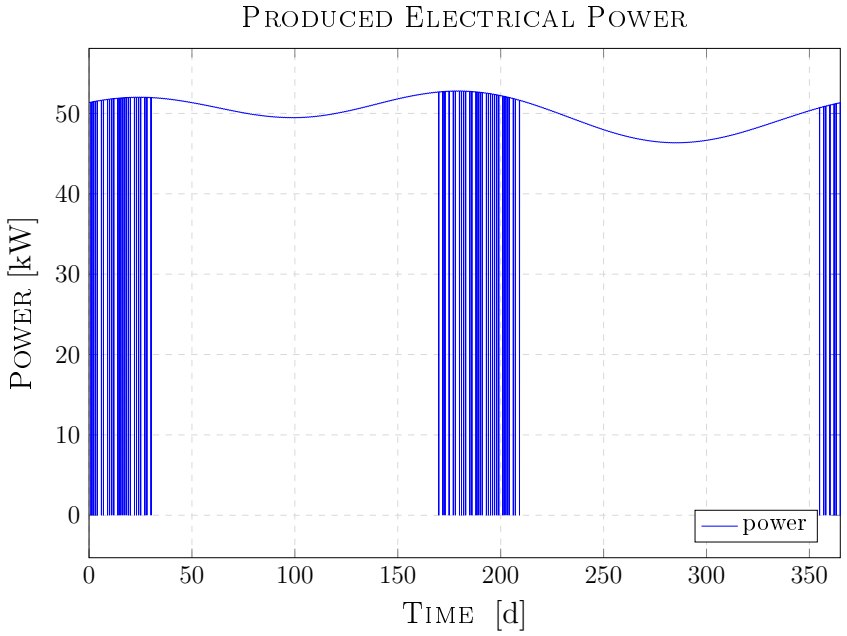

Figure 6.9: Electrical energy power production in one year [TRMPC-multibody]

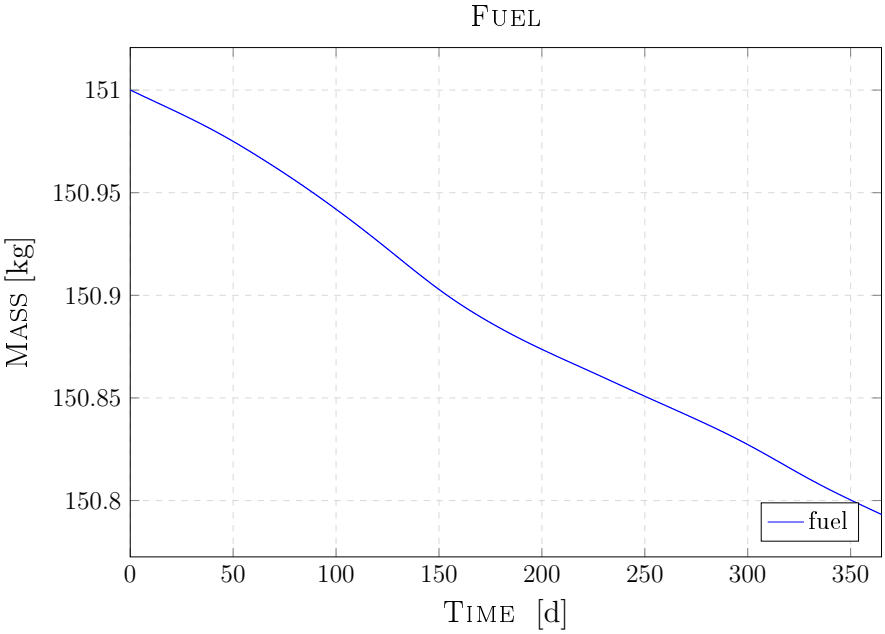

Figure 6.10: Xenon fuel consumption in one year [TRMPC-multibody]

6.4 Scenario 2. SMC multibody satellite with rotation SA

In the second scenario the Euler angles tracking error is the almost double compared to the first scenario. The amount of consumed fuel is comparable with the consumption of the first scenario. The production of electric power is almost double with respect to scenarios three and four, wheres is comparable with the electric power generated in the first scenario. The benefit of the SMC with respect to the TRMPC is the smoothness of the control input generated as can be seen by comparing the plots 6.15 and 6.5. The reference plots of scenario two are: Euler angles tracking error in Figures 6.11 and 6.12, disturbance torques in Figures 6.13 and 6.14, input torque in Figures 6.15 and 6.16, thrust produced by the thrusters in Figures 6.17 and 6.18, the electrical power produced in Figure 6.19 and finally the Xenon fuel consumption in Figure 6.20.

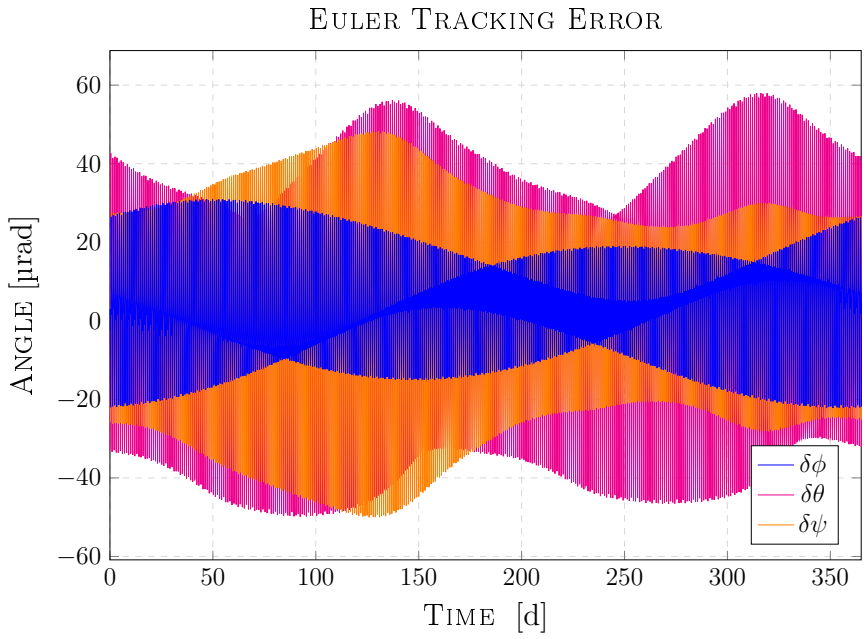

Figure 6.11: Euler tracking error in one year period [SMC-multibody]

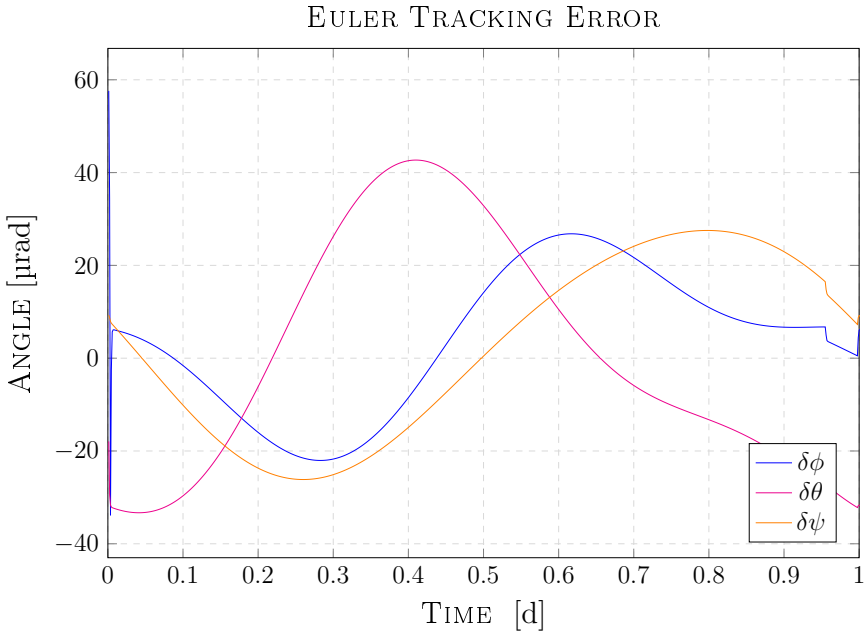

Figure 6.12: Euler tracking error, first day focus [SMC-multibody]

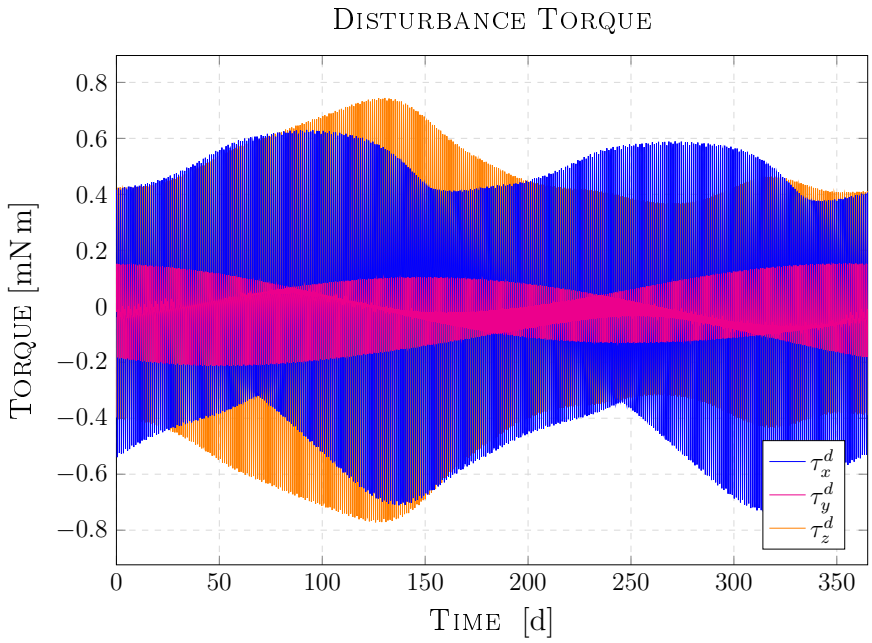

Figure 6.13: Disturbance torque in one year period [SMC-multibody]

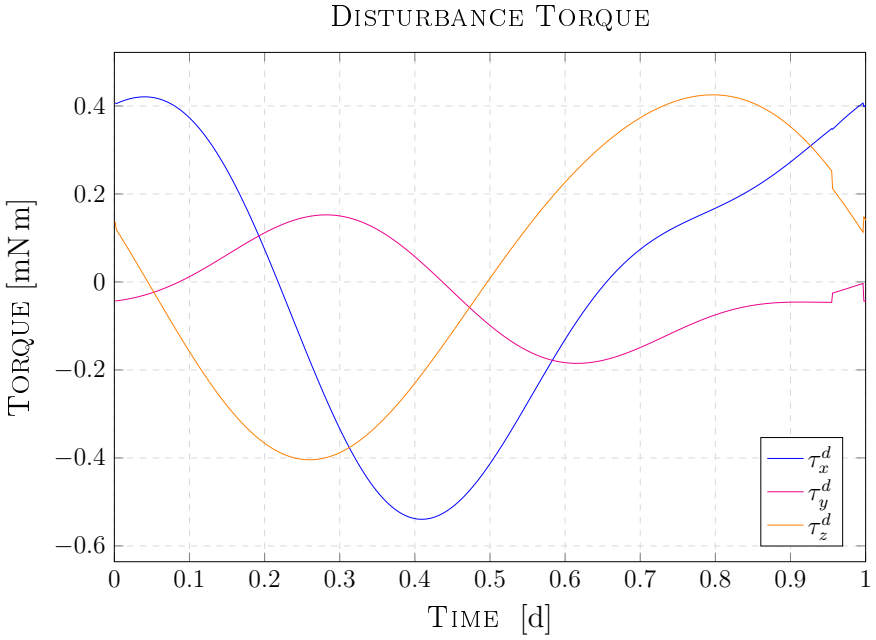

Figure 6.14: Disturbance torque, first day focus [SMC-multibody]

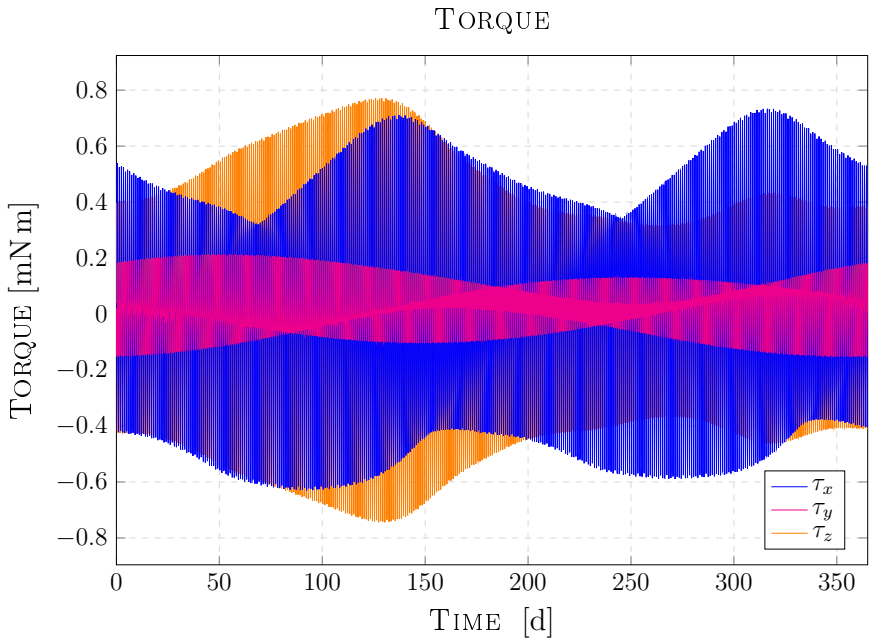

Figure 6.15: Torque in one year period [SMC-multibody]

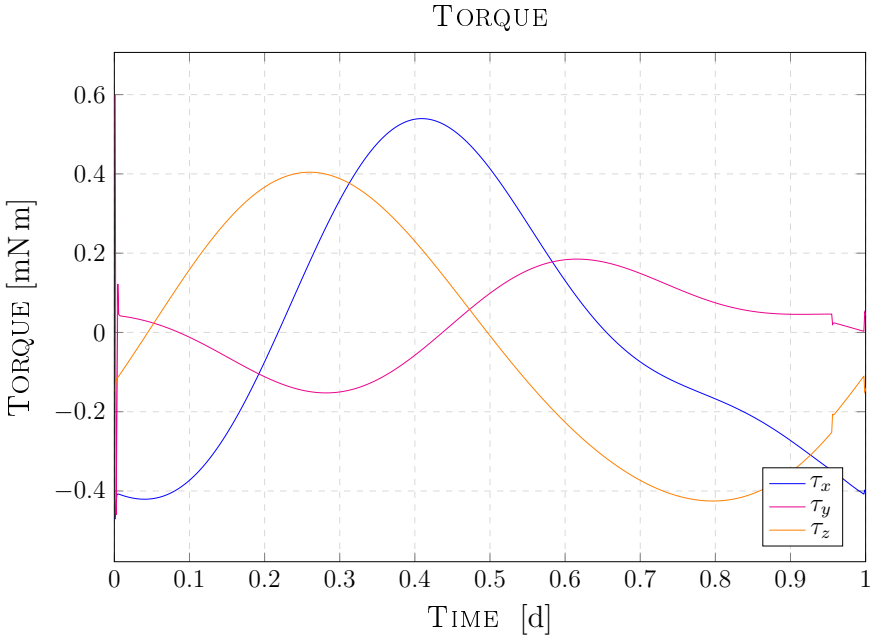

Figure 6.16: Torque, first day focus [SMC-multibody]

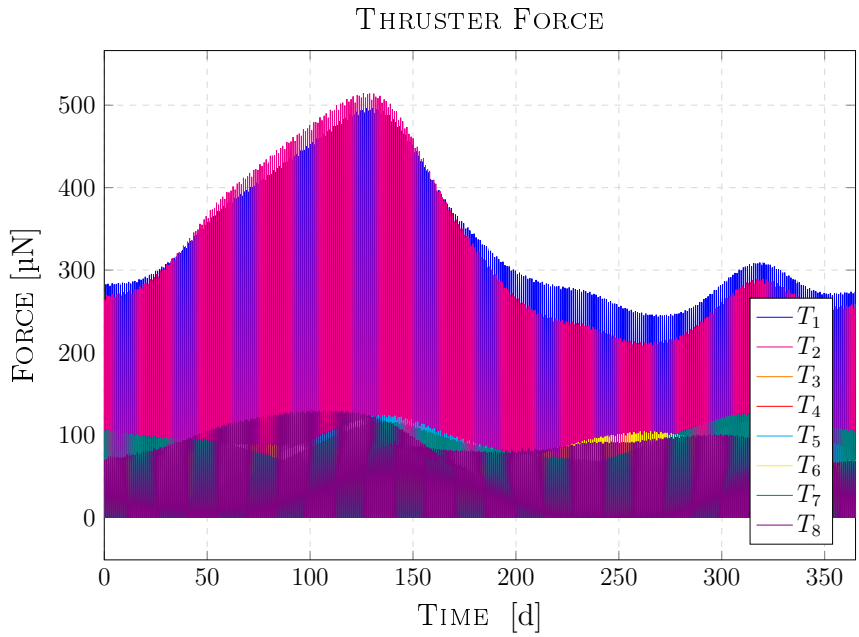

Figure 6.17: Thruster Force in one year period [SMC-multibody]

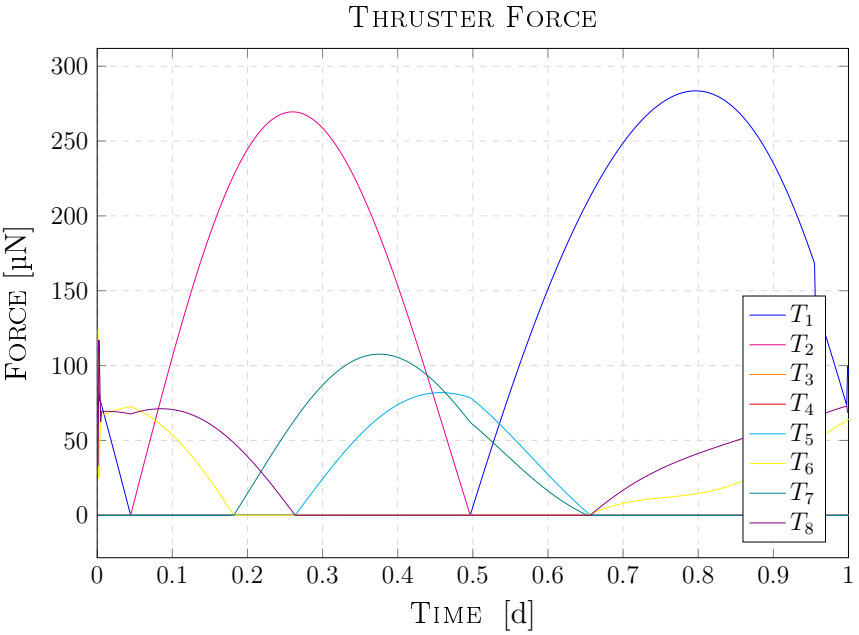

Figure 6.18: Thruster Force, first day focus [SMC-multibody]

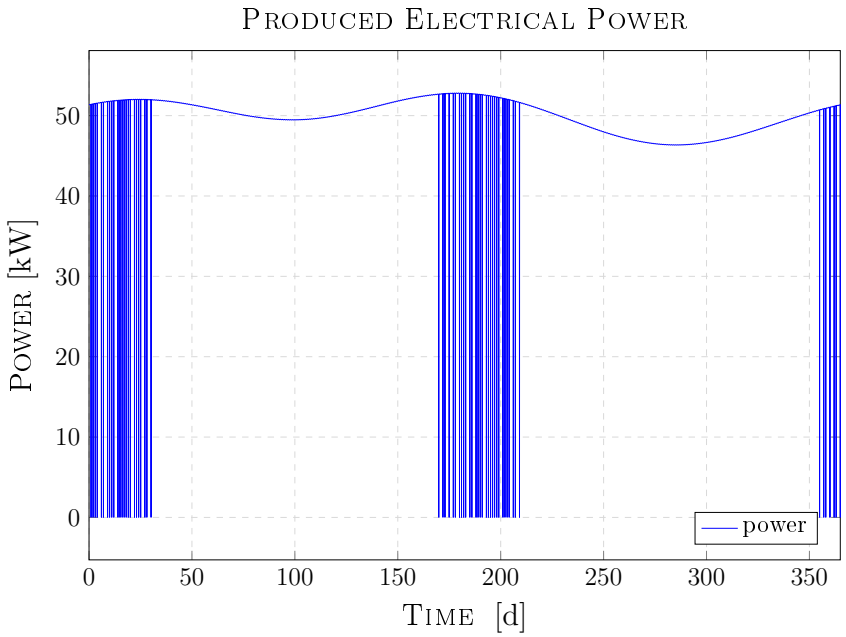

Figure 6.19: Electrical energy power production in one year [SMC-multibody]

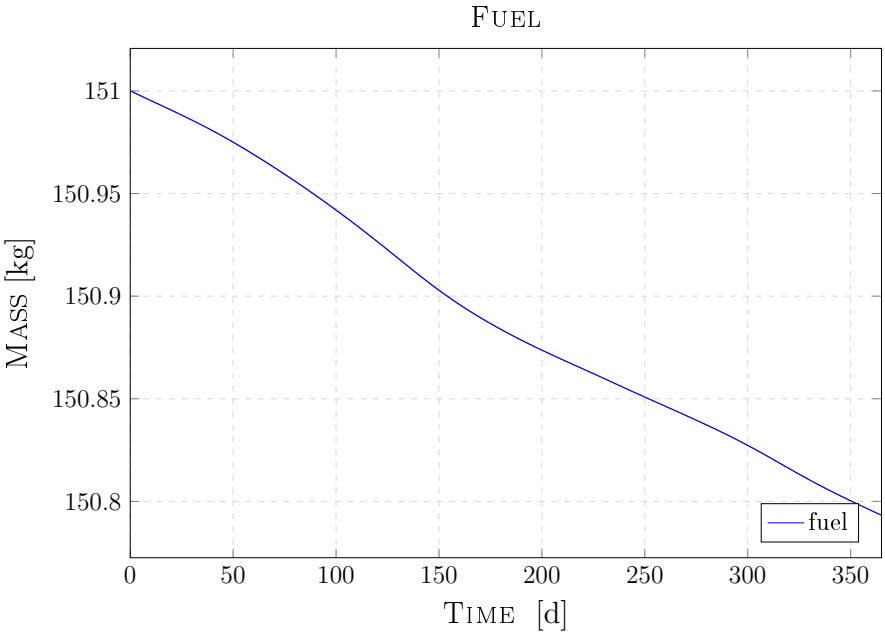

Figure 6.20: Xenon fuel consumption in one year [SMC-multibody]

6.5 Scenario 3. TRMPC fixed SA

In the third scenario we analyze the first fixed SA configuration. The Euler tracking performances are comparable with the results obtained in the first scenario. The disturbance torque magnitude is comparable with all the other scenarios. The electric power production is half with respect to the configuration with the rotating SA. The amount of consumed fuel is lower with respect to the configurations with the rotating SA. The same oscillatory behavior reported in scenario one, where also the TRMPC is implemented, is still present. The reference plots of scenario three are: Euler angles tracking error in Figures 6.21 and 6.22, disturbance torques in Figures 6.23 and 6.24, input torque in Figures 6.25 and 6.26, thrust produced by the thrusters in Figures 6.27 and 6.28, the electrical power produced in Figure 6.29 and finally the Xenon fuel consumption in Figure 6.30.

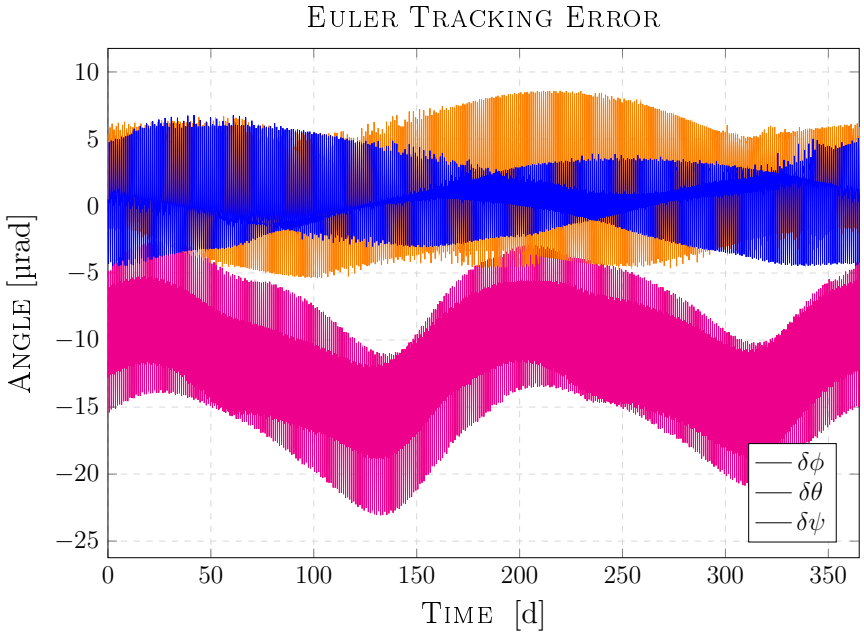

Figure 6.21: Euler tracking error in one year period [TRMPC-fixed]

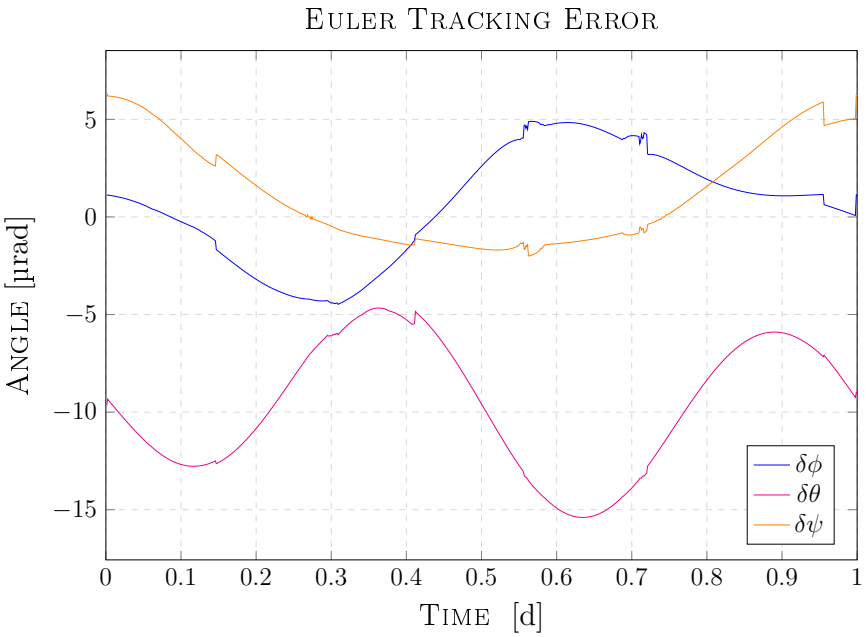

Figure 6.22: Euler tracking error, first day focus [TRMPC-fixed]

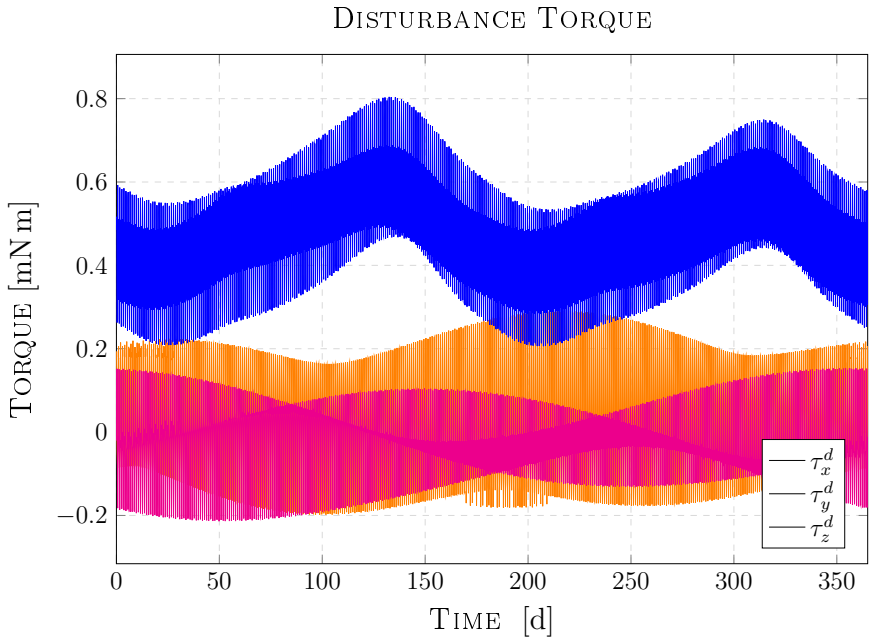

Figure 6.23: Disturbance torque in one year period [TRMPC-fixed]

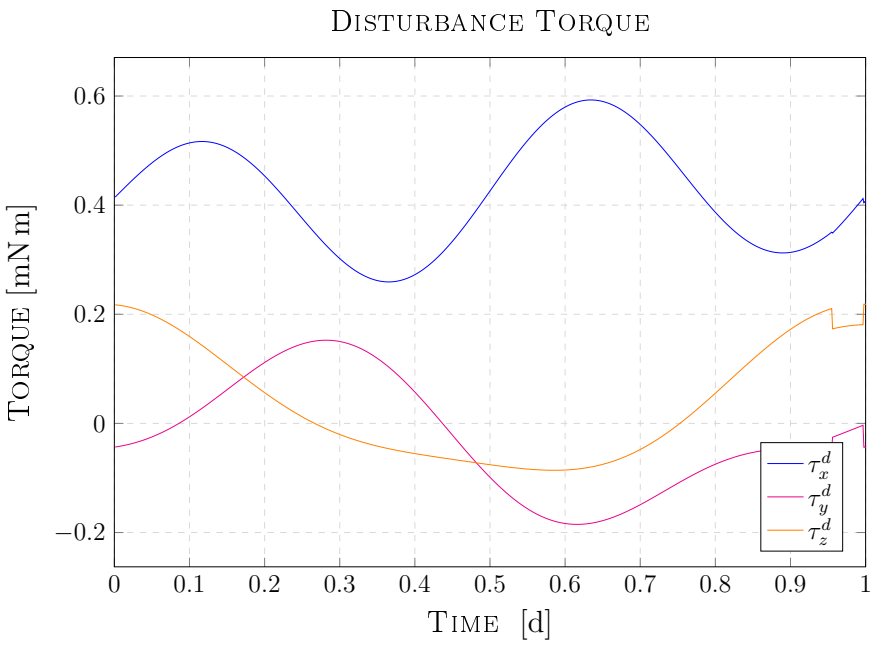

Figure 6.24: Disturbance torque, first day focus [TRMPC-fixed]

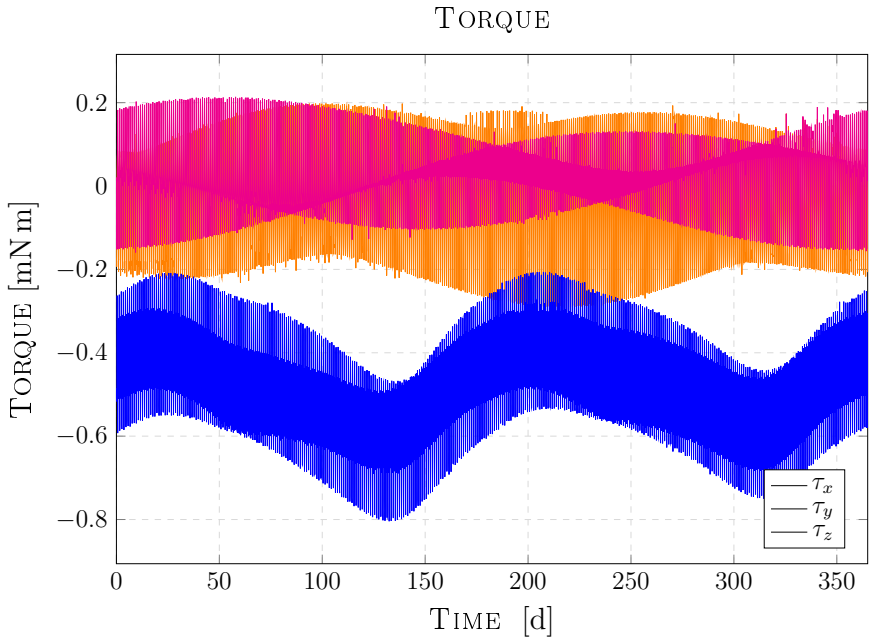

Figure 6.25: Torque in one year period [TRMPC-fixed]

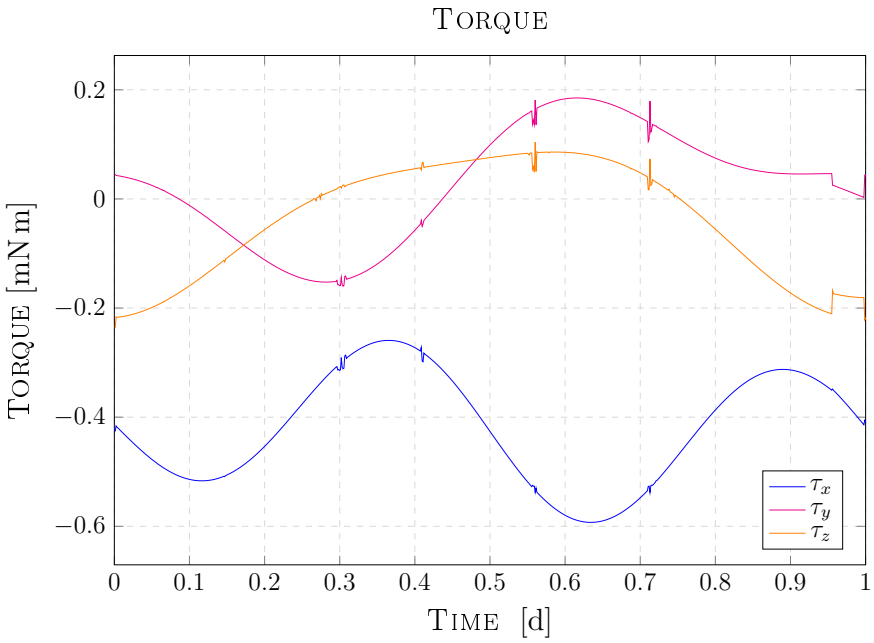

Figure 6.26: Torque, first day focus [TRMPC-fixed]

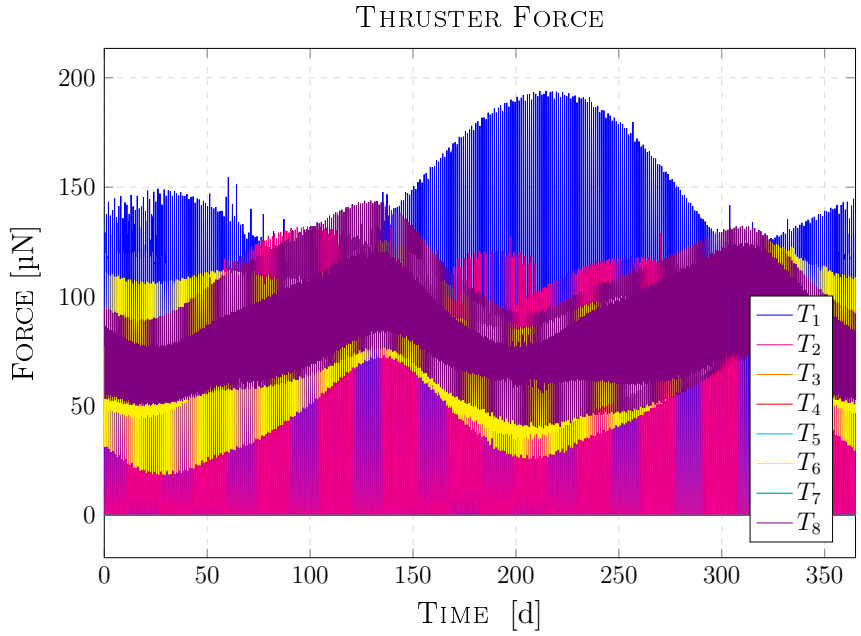

Figure 6.27: Thruster Force in one year period [TRMPC-fixed]

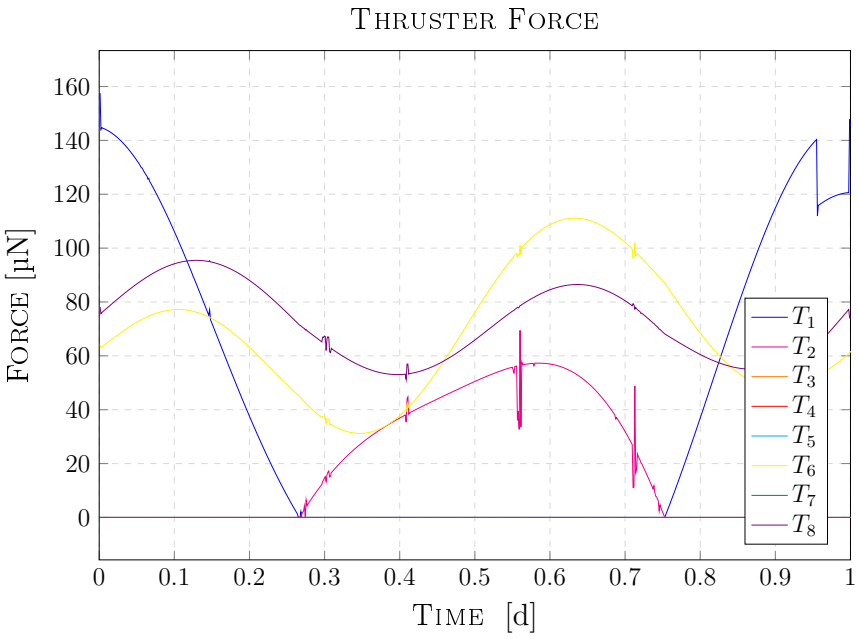

Figure 6.28: Thruster Force, first day focus [TRMPC-fixed]

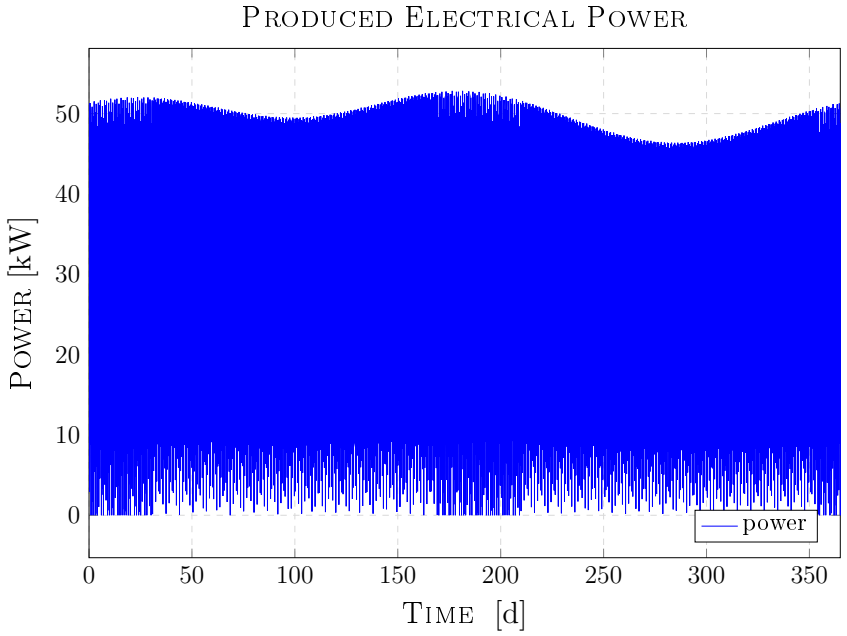

Figure 6.29: Electrical energy power production in one year [TRMPC-fixed]

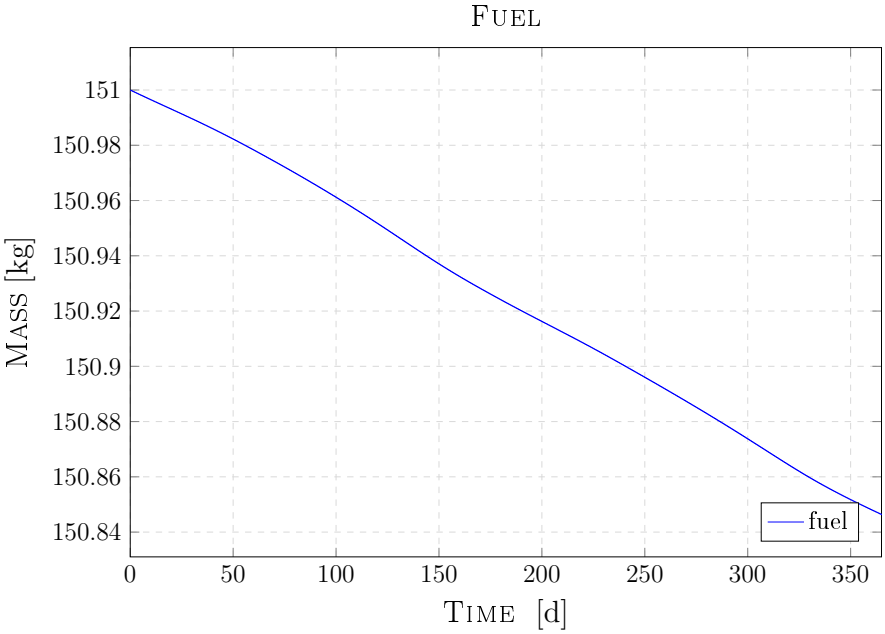

Figure 6.30: Xenon fuel consumption in one year [TRMPC-fixed]

6.6 Scenario 4. SMC fixed SA

In the fourth scenario the Euler angles tracking error is the worst obtained. The amount of consumed fuel and production of electric power is comparable with scenario three. The SMC control input smoothness with respect to the TRMPC is still present. The reference plots of scenario four are: Euler angles tracking error in Figures 6.31 and 6.32, disturbance torques in Figures 6.33 and 6.34, input torque in Figures 6.35 and 6.36, thrust produced by the thrusters in Figures 6.37 and 6.38, the electrical power produced in Figure 6.39 and finally the Xenon fuel consumption in Figure 6.40.

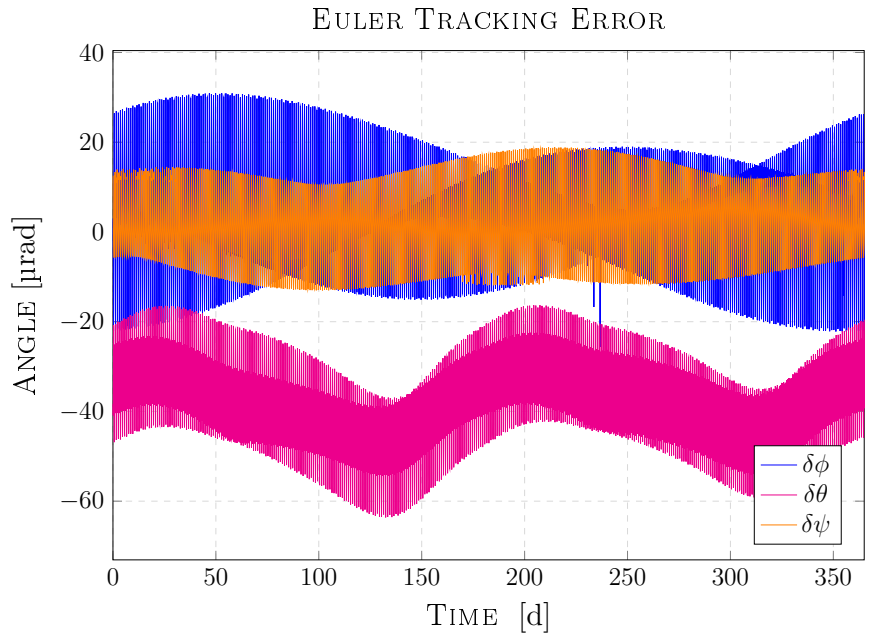

Figure 6.31: Euler tracking error in one year period [SMC-fixed]

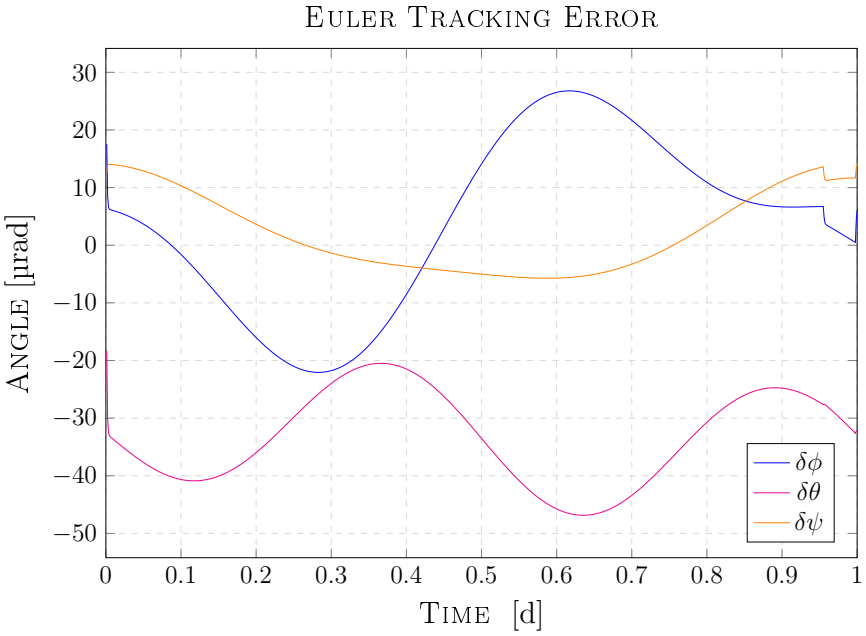

Figure 6.32: Euler tracking error, first day focus [SMC-fixed]

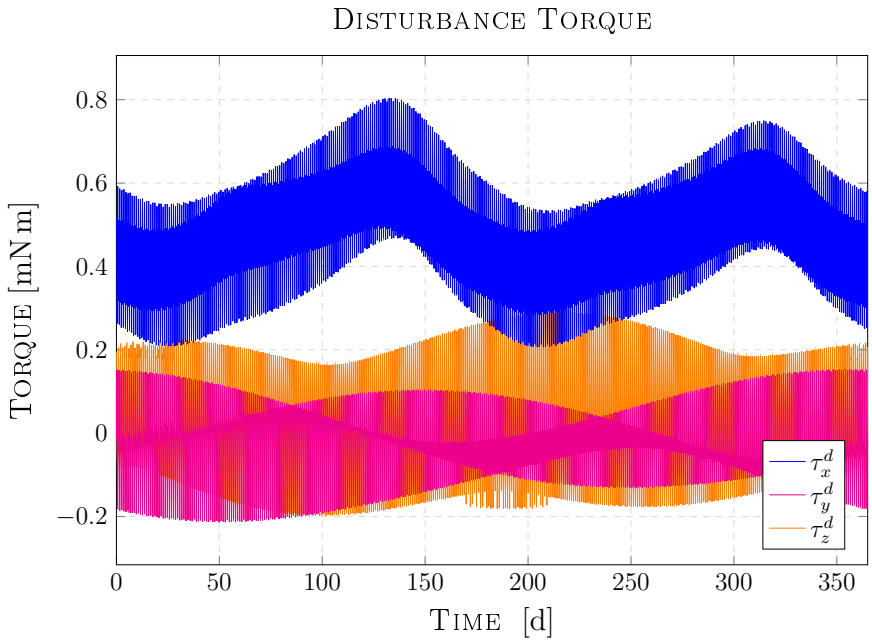

Figure 6.33: Disturbance torque in one year period [SMC-fixed]

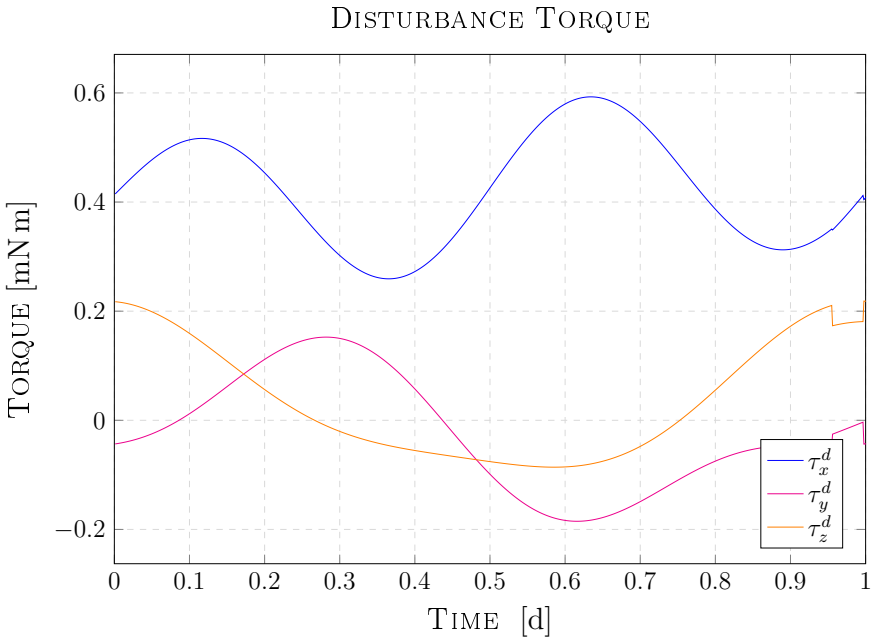

Figure 6.34: Disturbance torque, first day focus [SMC-fixed]

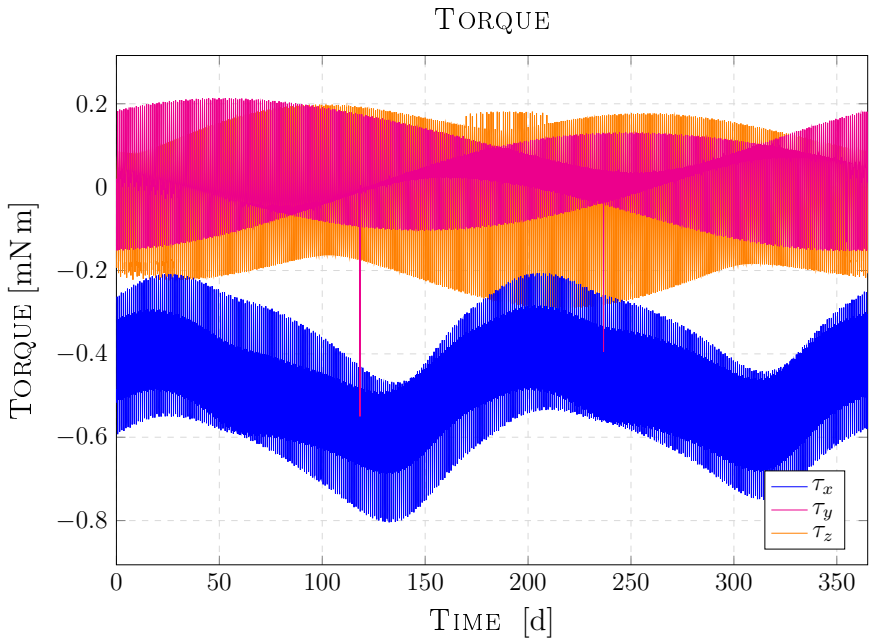

Figure 6.35: Torque in one year period [SMC-fixed]

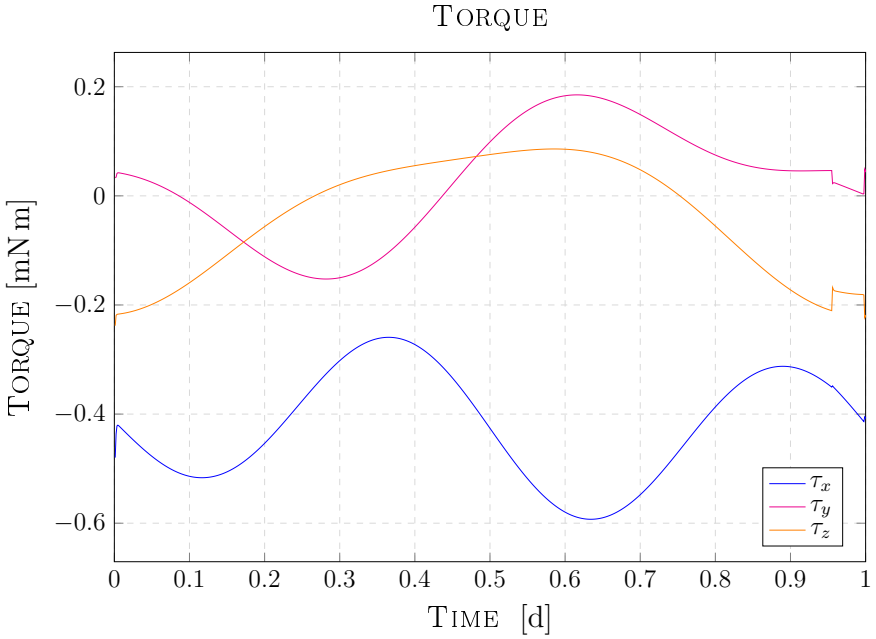

Figure 6.36: Torque, first day focus [SMC-fixed]

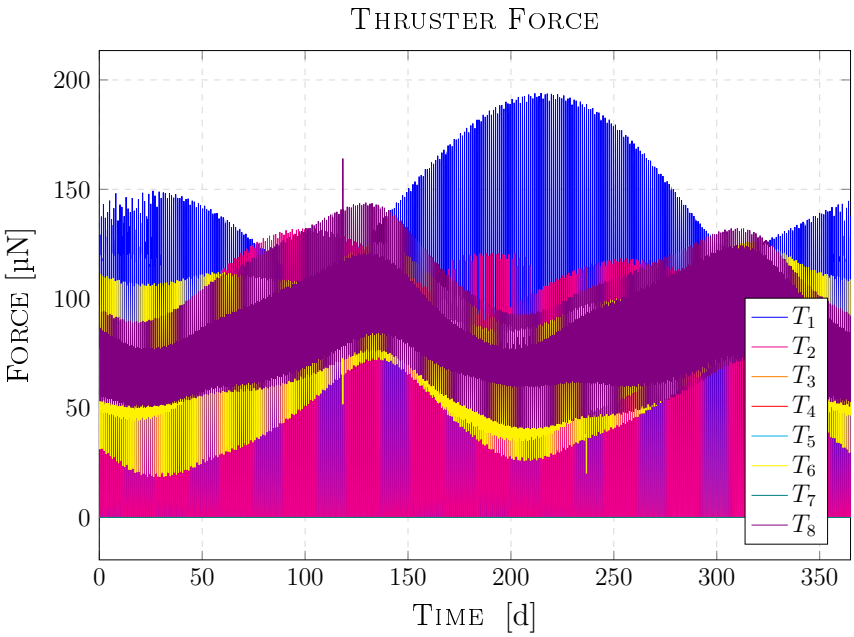

Figure 6.37: Thruster Force in one year period [SMC-fixed]

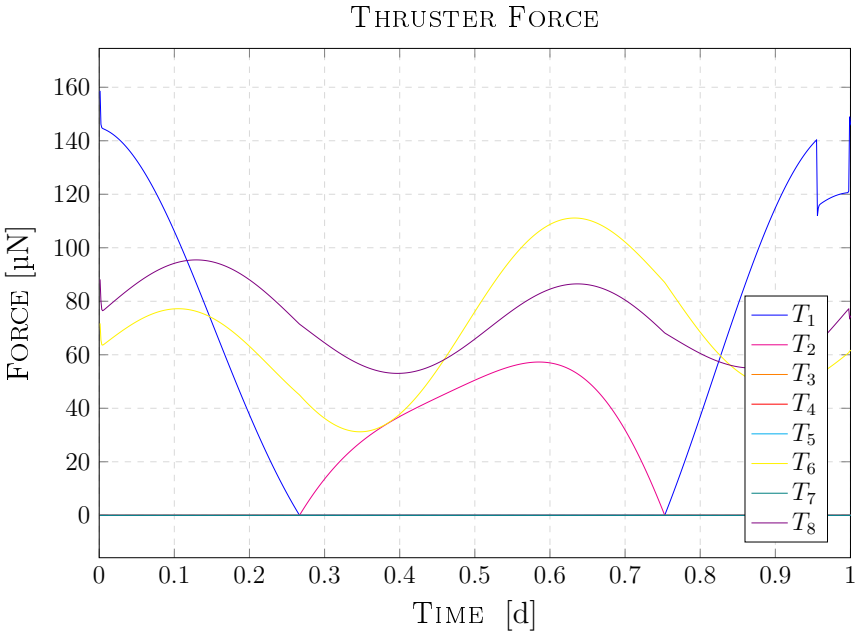

Figure 6.38: Thruster Force, first day focus [SMC-fixed]

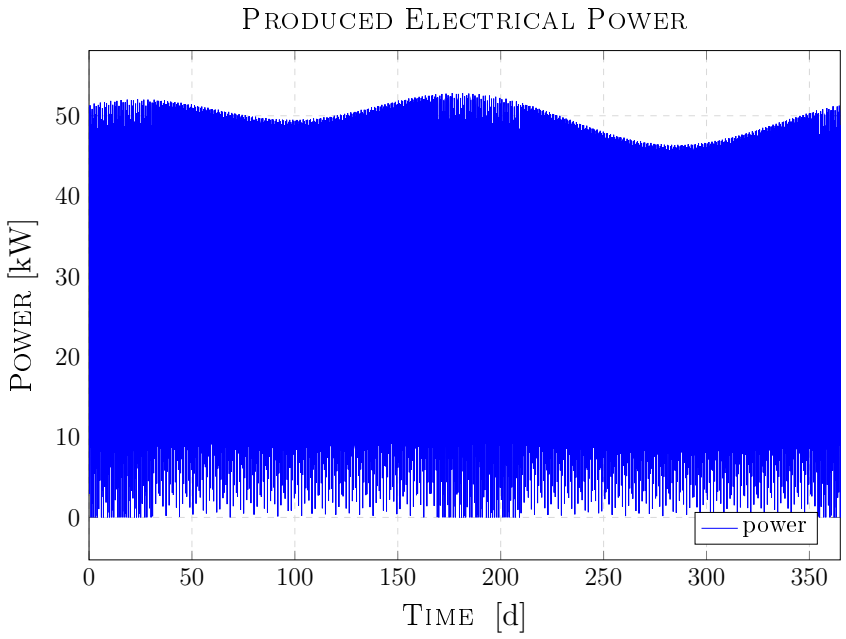

Figure 6.39: Electrical energy power production in one year [SMC-fixed]

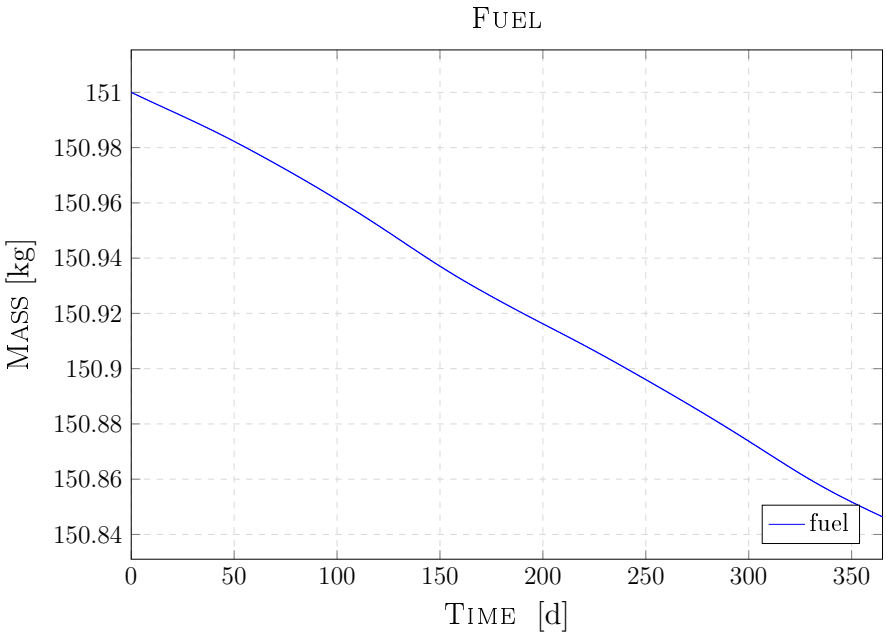

Figure 6.40: Xenon fuel consumption in one year [SMC-fixed]

Chapter 7

Conclusions and Future Works

In this thesis project a system analysis of the propulsion system and the electrical power subsystem of the GEO satellite Eutelsat 172B has been carried out. After the modeling phase, several simulations in different scenarios have been performed. The goal of the thesis is to verify the effectiveness of the introduction of the SADA and its interaction with the propulsion subsystem and the electrical power subsystem. The analysis is focused on the production of energy, the attitude tracking performances and the fuel consumption.

The key results obtained are:

- the feature of rotating solar arrays effectively increase and stabilize the production of electrical energy not influencing significantly the attitude tracking error performances
- the proposed TRMPC controller allows to achieve better tracking performances against the classical SMC approach, whereas the SMC provides smoother control input signals
- the fuel consumption for the configuration with the rotating SA is almost 50 percent higher with respect to the fixed SA configuration. Anyway this is a minor drawback since in absolute values the benefit obtained in the power production is higher.

This study was an effort to pave the path for future works in GEO satellite design. There is plenty of room for improvements, due to the hypothesis that we have made in the modeling phase. Some of the most important feature to can be added are

- The coupling of the orbital control and the introduction of the orbital dynamics disturbance can give more realistic results on the consumption of fuel and the tracking performances.
- The SA dynamic model and thus this add the disturbance created by the SA
- A more sophisticated modeling for the thrusters shall be implemented to create a more realistic simulator

By introducing these feature simulation outcomes will be more realistic and the conclusion based on the simulator results will be definitely more accurate and significant.

Bibliography

[1] E. C. SA, "Satellite eutelsat 172b." https://www.eutelsat.com/files/PDF/brochures/EUTELSAT_SATELLITE_E172B.pdf. Accessed: 2021-02-10.

[2] ESA, "Geostationary orbit esa." https://www.esa.int/ESA_Multimedia/Images/2020/03/Geostationary_orbit. Accessed: 2021-02-10.

[3] F. Markley and J. Crassidis, *Fundamentals of Spacecraft Attitude Determination and Control*. Springer-Verlag New York, 2014.

[4] H. D. Curtis, *Orbital Mechanics for Engineering Students*. Butterworth-Heinemann, 2019.

[5] J. Rawlings and D. Mayne, *Model predictive control: theory and design*. Nob Hill, 2009.

[6] "List of satellites in geosynchronous orbit." https://en.wikipedia.org/wiki/List_of_satellites_in_geosynchronous_orbit. Accessed: 2021-02-10.

[7] J. T. Satre, "Geosynchronous satellite." https://web.archive.org/web/20030417162310/http://web.mit.edu/invent/iow/rosen.html. Accessed: 2021-02-10.

[8] M. Finch, "Limited space: Allocating the geostationary orbit," *7 Nw. J. Int L. and Bus*, 1986.

[9] NASA, "Nasa technology roadmap," 2015.

[10] ESA, "Esa electric propulsion." https://www.esa.int/Enabling_Support/Space_Engineering_Technology/What_is_Electric_propulsion. Accessed: 2020-06-30.

[11] Spaceflight101, "Eutelsat 172b." https://spaceflight101.com/ariane-5-va237/eutelsat-172b/. Accessed: 2021-02-10.

[12] J. Gonzalez and S. G., "Esa electric propulsion activities," *32nd International Electric Propulsion Conference*, 2011.

[13] D. Nicolini and R. D., "Xenon resistojets as a secondary propulsion on ep spacecrafts and performance results of resistojets using xenon," *28th International Electric Propulsion Conference*, 2003.

[14] M. Leomanni and A. Garulli, "An mpc-based attitude control system for all-electric spacecraft with on/off actuators," *52nd IEEE Conference on Decision and Control*, 2013.

[15] D. Zlotnik and S. Di Cairano, "Mpc for coupled station keeping, attitude control, and momentum management of geo satellites using on-off electric propulsion," *IEEE Conference on Control Technology and Applications*, 2017.

[16] A. Bemporad and M. Morari, "Robust model predictive control: A survey," *Robustness in Identification and Control*, 1999.

[17] M. Mammarella, "Attitude control of a small spacecraft via tube-based model predictive control," *AIAA SPACE and Astronautics Forumand Exposition*, 2018.

[18] E. Gietl and E. W. Gholdston, "The electric power system of the international space station: A platform for power technology development," *Aerospace Conference*, 2000.

[19] J. Martin and C. d'Allest, "Eurostar 3000 aocs design," *4th ESA International conference on Spacecraft Guidance, Navigation and Control Systems*, 1999.

[20] Z. e. a. Tong, "Adaptive robust control with input shaping technology for solar array drive system," *Acta Astronautica*, 2017.

[21] C. e. a. Guo, "Active control technology for flexible solar array disturbance suppression," *Aerosapce Science and Techonology*, 2020.

[22] J. e. a. Martin, "Eurostar 3000 aocs design," *Proceedings 4 ESA International Conference on Spacecraft guiadance, navigation and control systems*, 2000.

[23] G. S. Page, "Eutelsat 172b." `https://space.skyrocket.de/doc_sdat/eutelsat-172b.htm`. Accessed: 2020-06-30.

[24] W. Larson and J. Wertz, *Space Mission Analysis and Design*. Space Technology Library, 1992.

[25] SpectroLab, "Spectrolab ultra triple junction (utj) solar cells," 2020.

[26] R. Space, "Septa® 24 solar array drive assembly," 2020.

[27] D. Goebel and I. Katz, *Fundamentals of electric propulsion: ion and Hall thrusters*. John Wiley & Sons, 2008.

[28] D. Manzella, "Performance evaluation of the spt-140," *Proceedings of Electric Propulsion Conference*, 1997.

[29] M. Sidi, *Spacecraft dynamics and control*. Cambridge University Press, 1997.

[30] Enpulsion, "Enpulsion nano r3 datasheet." `https://www.enpulsion.com/order/`. Accessed: 2021-02-10.

[31] E. M. Standish and J. G. Williams, *Orbital Ephemerides of the Sun, Moon, and Planets*. NASA, 1992.

[32] J. T. Satre, "Satellite eclipse calculator." `https://www.satellite-calculations.com/Satellite/satellite_eclipse.htm`. Accessed: 2021-02-10.

[33] J. e. a. Wertz, *Space Mission Engineering: The New SMAD*. Microcosm Press, 2011.

[34] M. Tolstoj, "Analysis of disturbance torques on satellites in low-earth orbit based upon grace," Master's thesis, RWTH Aachen, 2017.

[35] B. Bona, *Dynamics Modelling of Mechtronic System*. Celid, 2013.

[36] C. Novara, "Slides of nonlinear control and aerospace applications," 2020.

[37] T. Lu and S. Shiou, "Inverses of 2x2 block matrices," *Computers and Mathematics with Applications*, 2002.

[38] D. Luenberger and et al, *Linear and nonlinear programming*. Springer, 1984.

[39] D. Simon, *Optimal state estimation*. Wiley, 2006.

[40] B. Stellato, G. Banjac, P. Goulart, A. Bemporad, and S. Boyd, "OSQP: an operator splitting solver for quadratic programs," *Mathematical Programming Computation*, 2020.

[41] G. Calafiore and L. El Ghaoui, *Optimization Models*. Cambridge University Press, 2014.

[42] B. Kouvaritakis and M. Cannon, *Model Predictive Control: Classical, Robust and Stochastic*. Springer, 2016.

[43] E. Kolmanovsky, I. ans Gilbert, "Theory and computation of disturbance invariant sets for discrete-time linear systems," *Mathematical problems in engineering*, 1998.

[44] M. Herceg, M. Kvasnica, C. Jones, and M. Morari, "Multi-Parametric Toolbox 3.0," in *Proc. of the European Control Conference*, (Zürich, Switzerland), pp. 502–510, July 17–19 2013. `http://control.ee.ethz.ch/~mpt`.